In-vitro Corrosion Studies of Biopolymers-coated Magnesium and Magnesium Alloys

A Thesis submitted to

Fulfilment of the Requirements

for the Award of the Degree of

DOCTOR OF PHILOSOPHY

in

METALLURGICAL AND MATERIALS ENGINEERING

by

HANUMA REDDY TIYYAGURA

(Roll No. 701360)

Under the guidance of

Prof. M. K. Mohan

Professor

National Institute of Technology, Warangal

Telangana State

DEPARTMENT OF METALLURGICAL AND MATERIALS ENGINEERING

NATIONAL INSTITUTE OF TECHNOLOGY

WARANGAL - 506 004, TELANGANA STATE, INDIA

MARCH - 2018

DEPARTMENT OF METALLURGICAL AND MATERIALS ENGINEERING NATIONAL INSTITUTE OF TECHNOLOGY WARANGAL - 506 004 (T.S.) INDIA

CERTIFICATE

This is to certify that the work presented in the thesis entitled **"*In-vitro* Corrosion Studies of Biopolymers-coated Magnesium and Magnesium Alloys"** which is being submitted by **Mr. Hanuma Reddy Tiyyagura (Roll No: 701360),** is a bonafide work submitted to National Institute of Technology, Warangal in partial fulfilment of the requirements for the award of the degree of **Doctor of Philosophy** in **Metallurgical and Materials Engineering Department.**

To the best of our knowledge, the work incorporated in the thesis has not been submitted to any other university or institute for the award of any other degree or diploma.

Prof. M K Mohan

Head of the Department&Thesis Supervisor
Department of Metallurgical and Materials Engineering
National Institute of Technology
Warangal.

<u>Thesis Approval for Ph.D.</u>

This Thesis entitled: ***In-vitro* Corrosion Studies of Biopolymers-coated Magnesium and Magnesium Alloys**,by **Hanuma Reddy Tiyyagura** Roll No: 701360, is approved for the degree of Doctor of Philosophy.

Examiners

____

____

____

Supervisor

____

____

____

Chairman

____

Date :____________

Declaration

This is to certify that the research work presented in the thesis entitled***In-vitro* Corrosion Studies of Biopolymers-coated Magnesium and Magnesium Alloys** is a bonafide work done by me under the supervision of **Dr. M K Mohan**, was not submitted elsewhere for the award of any degree. I declare that this written submission represents my ideas in my own words and where others' ideas or words have been included, I have adequately cited and referenced the original sources. I also declare that I have adhered to all principles of academic honesty and integrity and have not misrepresented or fabricated or falsified any idea / data / fact / source in my submission. I understand that any violation of the above will be a cause for disciplinary action by the Institute and can also evoke penal action from the sources which have thus not been properly cited or from whom proper permission has not been taken when needed.

____

(Signature)

Hanuma Reddy Tiyyagura
Roll No. 701360.

Date: ___________

Acknow ledgements

During the course of my Doctoral Research work, I have received the assistance and support from the following people:

First and foremost, I am truly indebted and I express my earnest gratitude for my Research Supervisor ***Dr. M. K. Mohan****,* Professor, Department of MMED, National Institute of Technology Warangal for his inestimable expertise and astute guidance. His unabated enthusiasm, which stems from his absolute command over the subject, has been a constant source of inspiration for me to work hard and the outcome is expressed in the form of this thesis.

I express my gratitude to my co-research supervisor Prof***.VanjaKokol***, University of Maribor, Slovenia, for continuous support and valuable suggestions during my doctoral research.,

I am grateful to ***The Director***, National Institute of Technology, Warangal for giving me the opportunity to carry out the work and allowing me to submit in the form of a thesis. I greatly acknowledge ***Erasmus Mundus Euphrates,*** and ***Ministry of Human Resource Development, Govt. of India*** for the financial support in the form of fellowship.

I express my gratitude to the Doctoral Scrutiny Committee members: ***Prof. M.K. Mohan***, Chairman and Head, Department of Metallurgical and Materials Engineering, ***Dr.Asit Kumar Khanra***, Department of Metallurgical and Materials Engineering, ***Dr. B. Srinivasa Rao,*** Department of Metallurgical and Materials Engineering and ***Dr. K. V. Gobi***Department of Chemistry, NIT Warangal for their detailed review, constructive suggestions and excellent advice during the progress of this research work.

I take this opportunity to thank all my colleagues in the Department of MME, along with the kind help from non-teaching staff.My friends, Dr.Rangadhara Chary Varayogi ,Dr.

SaikumarGadakary, Rajesh, Sony, Suman, Sai Mahesh, Raju, who was always with me, encouraged me, and gave support all through the way in my life at NITW.I thank all my co-scholars and students for their constant motivation and encouragement.

My heart goes to my beloved Parents, and Family Members who with all their patience, prayers and faith in the Almighty, waited all these long years to see me reaching this stage. Their blessings and care always gave me new fervour and gusto to do something more with perfection.

Hanuma Reddy Tiyyagura

ABSTRACT

Metallic materials continue to play an important role in orthopaedic surgery, both as bone regeneration implants and as fixation devices. Among which stainless steel, cobalt-chromium, and titanium based alloys have been used for almost a century. New developments and innovative methods were proposed to make these materials even more suitable. In this regard, magnesium (Mg) with a redox potential of -2.37 V which is an active anode, has been found to be suitable. This could be the main contributing factor towards its biodegradable nature. The biodegradability eliminates the need of second surgery, which results in decreased costs and relief from pain to the patient. Other problem encountered in orthopaedic materials is the mismatching of Young's modulus, when compared to that of metal and bone, resulting in stress-shielding effect and loosening of implant. The Young's modulus of Mg is closer to that of bone which removes stress shielding effect. In this context, Mg and its alloys have gained considerable attention, recently, due to their attractive features, including biocompatibility, biodegradability and bioresorbability, all being related to their light weight with an appropriate density (1.74 - 2.0 g/cm^3) as well as excellent mechanical properties and elastic modulus (41-45 GPa).

The limitation of magnesium-based implants is too rapid degradation upon contact with body fluids, which causes reduction in the mechanical integrity before the tissue regeneration. This also leads to generation of H_2 and OH^- ions in the surrounding medium followed by increase of pH or alkalinity, and thus leads to delay in the healing process at implantation sites as well as tissue necrosis. In this thesis, alloying with Gd, Ag elements and different surface modifications by natural biopolymers like chitosan, gelatin and cellulose acetate were performed to overcome this problem.

Chapter I, II and **III**, explains the introduction, literature review and materials and methods respectively.

In **chapter 4.1** *in-vitro* corrosion properties of binary Magnesium alloys (Mg-4Ag and Mg-5Gd) have been discussed.The degradation behavior of these alloys was investigated in simulated body fluids (SBF) for 28 days and the morphology was investigated by SEM, EDS, FTIR, ICP-OES techniques. The corrosion performance was evaluated through the analysis of corrosion

resistance with time by using Electrochemical Impedance Spectroscopy (EIS) and cyclic polarisation measurements.

Chapter 4.2 discusses the magnesium surface coated with eletrospun natural polymer cellulose acetate (CA) membranes and its corrosion behaviour. Electrospinning is relatively simple technique to produce nano and micro-scale fibers, which possess unique properties (high (active) surface area to volume ratio and a tuneable porous structure), which are useful in the field of implants and tissue engineering. Electrospun CA nanofibers have shown great potential in different biomedical applications.In this study, the electrochemical behaviour of electrospunCA coated Mg was investigated in SBF solution at 37°C for 24 h.

Chapter 4.3 reveals the corrosion behaviour of AZ91 Mg alloy coated with gelatine (GEL) layer being mechanically stabilized by *in situ* cross-linking using non-cytotoxic carbodimide chemistry. Simulated body fluid (SBF) incubation was performed in order to evaluate the coating process-related improvement of the Mg alloy deterioration rate and its kinetic profile by following the pH studies. Furthermore, the corrosion behaviour was also evaluated using potentiodynamic polarization and impedance techniques and the surface morphology of corroded surface was analysed using scanning electron microscopy and energy-dispersive X-ray spectroscopy.

Chapter 4.4 evaluates the effect of physiological stability and corrosion resistance of chitosan-coated porous Mg monoliths. Although chitosan was already applied in the modification of Mg-containing implants for improving both anti-corrosion properties as well as biocompatibility, this effect onto pure and porous Mg-based materials has not been evaluated yet. In that respect, the Mg monoliths were prepared by Powder Metallurgy (P/M) technology using ammonium bicarbonate (NH_4HCO_3) as space holding particles to control the porosity profile, and being examined related to the microstructure by SEM and porosity analysis. The chitosan coating efficacy and stability were evaluated by FTIR and XRD spectroscopies, while the corrosion behaviour was followed by using an immersion test with gravimetrical and pH change evaluation. Finally, the mechanical (compression) performance and the mineralization potential onto the monolith surface were examined.

In **chapter 4.5**, the formation of Polydopamine (PDA)/ Gelatine (GEL) on magnesium monolith by dip coating technique and immersion in the SBF solution has been explained. FTIR,XRD and EDS techniques were used for finding out the chemical composition of the formed layer. The surface structure was examined byScanning Electron Microscope (SEM) and the corrosion behaviour of Mg coated by PDA/GEL in SBF solution evaluated by Potentiodynamic Polarization measurements(PDP)and Electrochemical Impedance Spectroscopic measurements(EIS). The influence of solution pH, and coating time on the achieved coating properties was investigated.

List of Figures

Fig.No	Title	Page Number
1.1	Research status of Biodegradable Metals.	4
1.2	Generalized materials, systems design chart for biodegradable Mg alloys designed for biomedical applications.	4
1.3	Comparison of the coating effectiveness on corrosion resistance of Mg alloys substrates.	8
1.4	Publications on Magnesium as biomaterial country wise (source – Scopus search).	9
1.5	Publications on Magnesium as biomaterial discipline wise (source – Scopus search).	9
2.1	(a) Schematic of the coating fabrication process, involving (I) MAO treatment, and (II) spin-based assembling. (b) The structure of the resulting M-CSCe hybrid coating.	15
2.2	Polarization of the samples to −1.5 V vs Ag/AgCl in 0.1 M NaCl.	16
2.3	Scanning electron microscopy (SEM) images of AZ31, aminated hydroxyethyl cellulose (AHEC)/AZ31, and hydroxyapatite/aminated hydroxyethyl cellulose (HA/AHEC)/AZ31 specimens: before (a–c); and after (d–f) immersion in simulated body fluid (SBF) for 7 days.	17
2.4	SEM micrographs of the uncoated and CA-coated Mg-1Ca-0.2Mn-0.6Zr alloy. Top view images of the uncoated (**a,b**) and CA-coated (**c,d**) alloy.	18
2.5	Corrosion performance of CMC composite coating measured by potentiodynamic polarization.	19
3.1	Scheme of needle-less electrospinning	25
4.1	Figure. 4.1: Optical micrographs of a) pure Mg b) Mg-4Ag, and c) Mg-5Gd.	29
4.2	pH values of the SBF solution followed by immersing of alloys up to 28 days at 37 0.5˚C.	30

4.3	Corrosion rates of alloys and Mg-ions release after immersion in SBF solution at 37 0.5˚C for 28 days.	31
4.4	ATR-FTIR analysis of 1) pure Mg 2)Mg-4Ag 3)Mg-5Gdalloys after 28 days of incubation in SBF solution at 37 0.5˚C.	31
4.5	XRD analysis of alloys after 28 days of incubation in SBF solution at 37 0.5˚C.	32
4.6	SEM images of pure Mg alloy surface showing on the formation of (a,d) corrosion products and cracks, (b) pits and (c) clusters.	33
4.7	SEM images of (a, b) Mg-4Ag and (c, d) Mg-5Gd alloys surface, after 28 days of incubation in SBF at 37 0.5˚C.	34
4.8	Nyquist plots showing measured (dotted symbols) and fitted (solid line) EIS data for a) pure Mg, b) Mg-4Ag, and c) Mg-5Gd measured after 1 h, 3 h, 5 h, 36 h, 48 h, 60 h, and 72 h of immersion in SBF solution at 37 0.5°C.	36
4.9	Fitted EIS parameters for alloys immersed for 1 h, 3 h, 5 h, 36 h, 48 h, 60 h, and 72 h in SBF at 37 0.5°C, obtained using the $R_s(R_1Q_1)(R_2Q_2L)$ EEC model in Figure f.	37
4.10	Cyclic polarisation measurements for alloys in SBF solution after 72 h at 37 0.5°C.	39
4.11	a) FTIR absorbance spectra of GEL-coated AZ91 Mg alloy before and after incubation in SBF (pH of 7.4 ±0.2) at 37±0.5 ºC for 7 and 30 days, and b) deconvoluted Amide I (1600-1700cm^{-1}) region of the respective samples with inserted histogram containing deconvolution data.	40
4.12	(i)FE-SEM images of uncoated AZ91Mg alloy (a) surface and (b) cross-section before incubation; the surfaces of (c,d) uncoated and (e,f) GEL-coated AZ91 alloy after incubation in SBF (pH of 7.4 ±0.2) at 37±0.5 ºC after 7 days.	43
	(ii) : FE-SEM images of uncoated AZ91Mg alloy surface (a) and cross-section (b,c), and GEL-coated AZ91 alloy surface (d) and cross-section (e,f) after incubation in SBF (pH of 7.4 ±0.2) at 37±0.5 ºC after 30 days.	44
4.13	XRD patterns of (a) uncoated and (b) GEL-coated AZ91 Mg alloys before incubation, and (c) uncoated and (d) GEL-coated AZ91 Mg alloy after incubation in SBF solution (pH of 7.4 ± 0.2) at 37 ± 0.5 ºC for 30 days.	45

4.14	a)Change in pH values of SBF solution with immersed uncoated and GEL-coated AZ91 Mg alloys at 37±0.5 ºC b) Potentiodynamic polarization curves of uncoated and GEL-coated AZ91 Mg alloy tested in SBF (pH of 7.4±0.2) at 37±0.5 ºC.	46
4.15	Nyquist and Bode plots of (a, b) uncoated and (c, d) GEL-coated Mg alloys as a function of time in SBF (pH of 7.4±0.2) at 37±0.5 ºC.	47
4.16	Equivalent circuit used for curve fitting of obtained EIS results.	49
4.17	EC parameters of (a, b) uncoated and (c, d) GEL-coated Mg alloy in SBF (pH of 7.4±0.2) at 37±0.5 ºC and different time intervals.	49
4.18	Equivalent Circuit (EC) fitted EIS curves as a function of immersion time (1, 3, 6, 12 and 24h) for uncoated and GEL-coated Mg alloys in SBF (pH of 7.4±0.2) at 37±0.5 ºC.	51000
4.19	FE-SEM images of Mg alloy surface coated with CA nanofibers a)before and b) after the electrochemical testing in SBF at 37°C for 24 h.	53
4.20	EIS Nyquist and Bode plots of (a & b) uncoated and (c & d) CA coated pure Mg as a function of immersion time Mg in SBF solution at 37 ± 5 ºC.	54
4.21	Equivalent circuit models (a) Uncoated and CA coated after 72 h and (b) CA coated.	55
4.22	(a) Equivalent circuit curve fitting plots of uncoated pure Mg as a function of time. (b) Equivalent circuit curve fitting plots of CA coated pure Mg as a function of time c)i) potentiodynamicpolarizationstudiesofPure Mg and CA coated Mg afterincubation of SBFsolutions at 37±0.5 ºC. ii) EDS analysis of CA coated samples after the corrosion test. d) Mechanism of CA-coated Mg in SBF solution.	57 58 60 60
4.23	SEM images of Mg monolith surfaces after first (at 130°C; a, b and c) and second (at 550°C; d, e and f) heat treatment, corresponding to different Mg/NH_4HCO_3 ratio (100/0, 90/10 and 80/20).	62

4.24	ATR-FTIR spectra of chitosan and chitosan-coated Mg monoliths prepared with the lowest (14%) porosity, before and after 48h incubation in SBF solution at 37°C.	63
4.25	(a). Anticipated surface and bulk phenomena of uncoated (above) and chitosan-coated (below) Mg-monolith, taking place before (a) and after (b) incubation in SBF media.	64
4.26	XRD spectra of i) uncoated and ii) chitosan-coated (14% porous) Mg monolith after 48 h of incubation in SBF solution.	65
4.27	The weight-loss of uncoated and chitosan-coated Mg monoliths of different porosity, and pH changes of SBF solution during 120 h of incubation at 37°C.	67
4.28	SEM images of chitosan-coated Mg monoliths of different porosity (14%, 30% and 40%) with different magnifications (A, B and C) after 48 h immersion in the SBF solution at 37°C.	68
4.29	SEM-EDX analysis of chitosan-coated Mg monoliths with different porosity (A 14%, B 30%, and C 40%) after 48 h immersion in the SBF solution at 37°C.	68
4.30	Stress-strain diagram of uncoated and chitosan-coated (14% and 40% porous) Mg monoliths (left) with extracted data for compression strength (MPa), maximum strain (%) and elastic modulus (MPa) for the same data set (right).	70
4.31	a) SEM micrograph of Mg Monolith b) PDA/GEL coated Mg monolith.	71
4.32	Typical results of the pH and weight loss measurements during immersion tests in SBF solution at 37˚C.	71
4.33	FTIR spectra of PDA/GEL coated Mg monolith before and after incubation in SBF solution after 168h.	72
4.34	SEM and EDS of PDA/GEL coated Mg monolith after incubation in SBF solution after 168hours.	74
4.35	XRD analysis of PDA/GEL coated Mg monolith after incubation in SBF solution after 168 hours.	75
4.36	PDP plots of Mg Monolith and DOPA/GEL Mg monolith	75
4.37	Nyquist and Bode Plots Mg Monolith and DOPA/GEL Mg monolith with equivalent circuits.	77

List of Tables

Table No	Title	Page Number
1.1	Comparison of the corrosion rates of the Mg, Fe and Zn-based BMs.	5
1.2	Density and mechanical properties of biomaterials.	7
3.1	Composition of Simulated Body Solution (SBF).	22
3.2	Chemical composition and density of Mg, Mg-4Ag and Mg-5Gd used through the study as specified by the supplier.	22
4.1	EDS analysis of alloys after 28 days of incubation in SBF at 37 0.5˚C.	34
4.2	a)Electrochemical parameters of uncoated and GEL-coated AZ91 Mg alloy. b) Comparison of corrosion currents of AZ91 alloy from literature data	46 47
4.3	Equivalent circuit parameters of uncoated and Gel coated AZ91 alloys.	52
4.4	Equivalent circuit curve fitting parameters of EIS results as a function of time.	56
4.5	EDX elements weight and atomic percentages.	69
4.6	Electrochemical data from the polarization curves coated monolith.	76
4.7	Equivalent circuit curve fitting parameters of EIS results	77
4.8	Compressive strength of the Mg monolith, and PDA/GEL Mg monolith before immersion test and after the immersion of the samples for 24, 144 and 336h in SBF solution.	79
4.9	Mechanical properties of porous Mg biomaterials	80

TABLE OF CONTENTS

CHAPTER 1

1.1 INTRODUCTION 3
1.1.1 Biodegradable metals: 3
1.1.2 History of Magnesium as biomaterial: 5
1.2. OBJECTIVES OF THE PRESENT STUDY 10

CHAPTER 2

2.1 LITERATURE REVIEW 11
2.2 ALLOYING ELEMENTS 12
2.3 BIODEGRADABLE POLYMERS 13
2.4 SURFACE MODIFICATION WITH GELATINE 13
2.5 SURFACE MODIFICATION WITH CHITOSAN 14
2.6 SURFACE MODIFICATION WITH CELLULOSE AND ITS DERIVATIVES 16
2.7 POROUS MAGNESIUM 19

CHAPTER 3

3.1 EXPERIMENTAL PROCEDURE 21
3.2 MATERIALS 21
3.3 IMMERSION TESTS 22
3.4 ATTENUATED TOTAL REFLECTANCE FOURIER TRANSFORM INFRARED (ATR-FTIR) SPECTROSCOPY ANALYSIS 23
3.5 X-RAY DIFFRACTION (XRD) ANALYSIS 23
3.6 SCANNING ELECTRON MICROSCOPY (SEM) IMAGING AND EDXS ANALYSIS 23
3.7 ELECTROCHEMICAL MEASUREMENTS 24
3.8 ELECTROSPINNING........ 25
3.9 PROCESSING OF POROUS MG MONOLITHS 25
3.10 CHITOSAN COATING 26
3.11 DOPA/GEL TREATMENT 26
3.12 IN *VITRO* DEGRADATION STUDY 26
3.13 COMPRESSION TESTING 27

CHAPTER 4

4.1 DEGRADATION AND ELECTROCHEMICAL CORROSION BEHAVIOR OF MG4AG AND MG5GD ALLOYS UNDER *IN-VITRO* CONDITIONS

4.1.1. *IN VITRO* DEGRADATION BEHAVIOR 29
4.2 ELECTROCHEMICAL BEHAVIOR 35
4.2.1 Electrochemical Impedance Spectroscopy (EIS) measurements 35
4.2.2 Cyclic polarisation measurements 38
4.2.3 Summary 39
4.3 *IN-SITU* CROSS-LINKED GELATINE COATING ON AZ91 MG ALLOY FOR LESS-CORROSIVE AND SURFACE BIOACTIVE ORTHOPAEDIC APPLICATION. 39
4.3.1 Coating characterization 39
4.3.2 Electrochemical corrosion behavior 45
4.3.4 Summary 52
4.4 ELECTROCHEMICAL STUDIES OF ELECTROSPUN COATED CELLULOSE ACETATE (CA) ON MAGNESIUM SURFACE 53

4.4.1 Electrochemical Impedance studies: **53**
4.4.2 Cellulose Acetate –Mg Mechanism: **59**
4.4.3 Summary **61**
4.5 THE CHITOSAN COATING AND PROCESSING EFFECT ON PHYSIOLOGICAL CORROSION BEHAVIOUR OF POROUS MAGNESIUM MONOLITHS **62**
4.5.1 Monoliths processing and microstructure characterization **62**
4.5.2 Coating identification and evaluation of monoliths stability **62**
4.5.3 Mechanical properties of monoliths **69**
4.5.4 Summary **70**
4.6 *IN-VITRO* STUDIES OF POLYDOPAMINE/GELATIN SURFACE MODIFIED POROUS MAGNESIUM MONOLITHS TO CONTROL DEGRADATION RATE. **71**
4.6.1 *In vitro* degradation testing **71**
4.6.2. Chemical Composition of PDA/GEL Layer Fabricated on Magnesium monolith **72**
4.6.3. Coating characterization **73**
4.6.5. Mechanical Properties **79**
4.6.5. Summary **81**

CHAPTER 5

5.1 CONCLUSIONS: **82**
5.2 SCOPE FOR FUTURE WORK: **83**

CHAPTER 6

6.1 REFERENCES: **84**
PUBLICATIONS BASED ON THE PRESENT WORK **100**
CONFERENCES / PROCEEDINGS **100**
BOOK CHAPTER: **101**

Chapter 1

1.1 Introduction

1.1.1 Biodegradable metals:

Recent advances in the usage of corrodible metals for the medical device application have gathered considerable interest among many researchers. The researchers have named these recent corrodible metals for medical applications using the word Biodegradable Metals(BM).Mg based BMs and other BMs (pure W, pure Zn etc) are classified based on their *in vitro* and *in vivo* performance and micro structures etc.[1]

The classification of BM as follows.

1. Mg-based alloys

2. Iron-based biodegradable metals

3. Zn-based alloys.

The three main body BM systems viz, Mg-based, Fe-based and Zn-based are shown in Figure 1.1. Among all the three, the Mg-based BMs have pioneered the research with hundreds of publications on vitro cytotoxicity, animal testing and clinical trials. The Fe-based BMs have few of publications on alloy design and several animal testing as potential vascular stent. The last one among the three is Zn-based BMs with megre publications.[2]

Due to the inherent degradable characteristics of Mg and its alloys, most of the degradable medical implant metals use these metals. Thus many of researchers have developed Mg materials in order to meet their requirements. BIOTRONIK developed three generations of absorbable metal stents (AMSs) using WE43 and modified Mg-based alloys as shown in Figure 1.2 [3].Comparison of corrosion rates of BMs as shown in Table 1.1.[2]

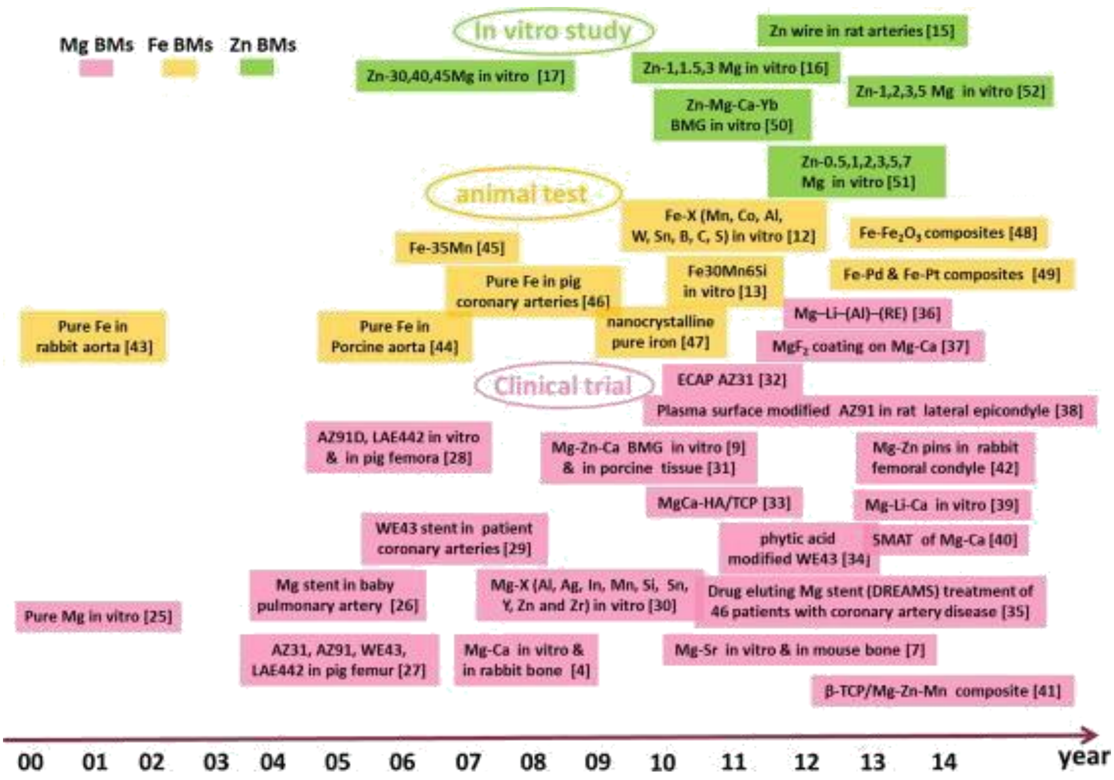

Figure 1.1. Research status of BiodegradableMetals

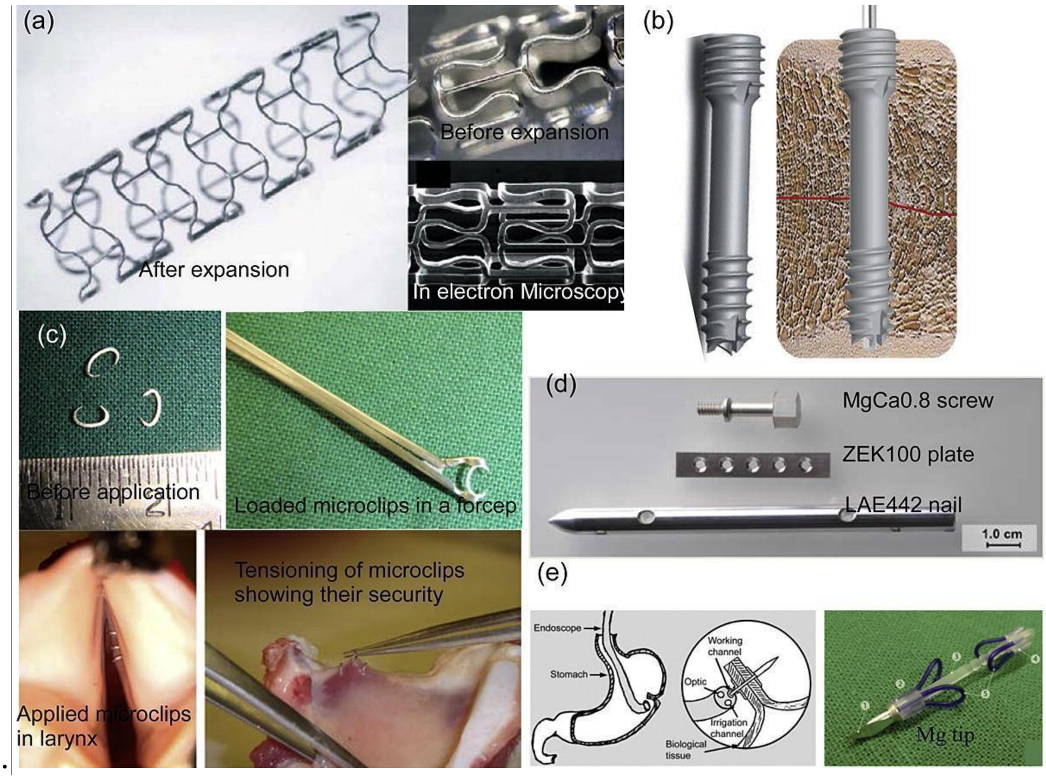

Figure 1.2. Generalized materials, systems design chart for biodegradable Mg alloys designed for biomedical applications

.

Table 1.1. Comparison of the corrosion rates of the Mg, Fe and Zn-based BMs.

Alloy system		*In vitro*(mm/yr)		*In vivo* (mm/yr)
		Electrochemical test	Immersion test	
Mg BMs	Mg	0.20	0.10 ±0.07	
	Mg–6Zn	0.16	0.07 ± 0.02	2.32 ± 0.11
	Mg–1Ca		12.56	1.27
	LAE442	6.9	5.535	0.46 ±0.11
	Mg–10Gd Mg–8Y Mg–0.8Ca	2.17±0.23	1.25 ± 0.2	0.39 ± 0.1
	Mg–2Sr	0.87 ± 0.08	0.37 ± 0.05	1.01±0.07
Fe BMs	Fe	0.105	0.012	
	Fe–2W	0.075	0.026	
	Fe–0.5CNT	0.099	0.048	
	Fe–Mn	0.105	0.0018	
	Fe–W	0.151	0.016	
Zn BMs	Zn		0.08	0.02
	Zn–1Mg		0.09	

1.1.2 History of Magnesium as biomaterial:

The first isolated aluminum and magnesium are reported in early 18th century by the British chemist Sir Humphrey Davy. In addition to these, Davy have also discovered various other metals along with their production process. Succeeding Davy, his assistant Faraday produced Mg metal in 1833 from the anhydrous $MgCl_2$. Though Mg is discovered in 1833, its commercialization is done in 1853 by a German scientist Robert Bunsen in his laboratory. The first industrial Mg samples are exhibited at London in the year 1852. These industrial samples were mainly used in pyrotechnical applications. During the same years, the countries like France, England and USA were using the Mg for photographical applications. In 1886, the Germany started production of commercial Mg with the modification of Bunsen's cell. In Germany, the Aluminum and Magnesium Farbik in Hemelingen (Germany) is developed for the dehydration and electrolysis of molten carnallite. Later in 1896, Chemische Fabrik

Griesheim-Elektron have extended this process to Bitterfeld works and became the pioneer in Mg production till the early 19th century. Later Griesheim-Elektron have merged with I.G. Farbenindustrie AG, as a result most of the magnesium alloys having the brand name Elektron were developed for both technical and medical applications. In the year 1925, American Magnesium Corporate and the Dow Chemical Company were only the major companies produced Mg in USA. During the early 19th century, the smaller quantities of Mg were produced in countries like Italy, France etc. [4]

Modern orthopedics implantology relies mainly on the metals that assure mechanical resistance to dynamic loads and exhibits excellent corrosion resistance and reasonable level of biocompatibility [5]. However, the complexity of bone tissue regeneration and metallic implant osseointegration without the risk of infections and cell phenotype/genotype changes, is still a great challenge, causing major health risks such as discomfort, tissue destruction, loss of the implant, amputation, systemic illness and in many cases, even in the death of the patient. Often, a second surgery is carried out that leads to extra scarring, prolonged healing time, pain and consequently a considerable economic impact [6,7]. Both prevention of infection and integration of the implant with the bone tissue are thus highly challenging tasks to replace an injured and diseased bones and joints by metal-based implants [8,9].

Biodegradable implants [10] have already proved their clinical efficiency in cardiovascular and orthopaedic devices [11–13]. Among them, magnesium (Mg)-based ones are the most promising, especially in hard tissue regeneration [14–16]. They offer several advantages over the conventionally used metals (e.g. stainless steel, cobalt-based and titanium-based alloys [12]) including greater fracture toughness, good match of the elastic modulus and compressive yield strengths (to cortical human bone) [17], reduced stress shielding [18], light weight [19,20], excellent biocompatibility [21], biodegradability [22] and bio-resorbability [23–25], and compatible mechanical properties, closer to that of natural bone [1,26] presented in Table 1.2. Acting as temporary implants, they can be dissolved within the human body, without the need of a second surgical intervention for its removal. However, too rapid degradation of magnesium-based implants upon contact with body fluids [27,28] is the main limitation, which causes reduction in the mechanical integrity before the tissue regeneration [29]. This also leads to generation of H_2 and OH^- ions in the surrounding medium followed by increase of pH or alkalinity, and thus leads to delay in the healing process at implantation sites as well as tissue necrosis [30]. Therefore, there is an increasing demand for the design and development of suitable Mg-based implants with an appropriate degrading rate and bio-safe corrosion products.

Table 1.2: Density and mechanical properties of biomaterials.

Material	Density (g/ cm^3)	Tensile strength (MPa)	Young's modulus (GPa)	Cost Estimation Rank
Cortical bone	1.7-2.0	8-150	3-30	N/A
Magnesium	1.74-2.0	170	41-45	2
Ti-6Al-4V	4.45	930-1140	100-110	3
Stainless steel	7.9	480-620	165-200	1
Co - Cr alloys	7.8	-	230	4

The choice of appropriate material processing is one approach for controlling the degradation of Mg-based implants, which explains the higher performance (by means of lower H_2 evolution, as well as pH control) of porous-, comparing to compact (non-porous) Mg-based materials [31]. In this respect, different techniques for the production of porous Mg materials have been applied as e.g. Gasar process, infiltration process, laser perforating technique and powder metallurgy (P/M) [32]. The latter one have been recently found its place in the biomedical area, advancing the production of near net shapes with narrow tolerances and controlled porosity, the use of different powders (ceramic, metallic, non-metallic etc.), achievement of high surface quality and lower cost than other conventional methods, like casting and extrusion. This process also allow the formation of finer and uniform dispersion of second phases and grain refinement, grain size control, and consequent mechanical properties improvement, respectively [33].

The other approach for degradation delay or improved corrosion resistance, which simultaneously affect the quality of the bone–implant integration while preventing the occurrence of intervening fibrous tissue layer, is surface modification of Mg-based implants. This includes alloying, micro arc oxidation [34,35], plasma electrolytic deposition [36], magnetron sputtering [37], electrophoretic deposition[38], sol-gel, electro deposition, physical vapour deposition, chemical vapour deposition [39]ion implantation [40], hydroxyapatite [41] and polymer [42] coating respectively. The effectiveness of these coatings on corrosion resistance have been shown in Figure.1.3 [1] In comparison with synthetic polymers (e.g. polylactic acid, poly lactic-co-glycolic acid, polycaprolactone), the biopolymer coatings using hyaluronic acid, chitosan, cellulose, alginate, poly-l-lysine, collagen, fibronectin etc. [43] were found more biocompatible, mainly due to the lack of highly acidic degradation products related to the synthetic ones. Their bioactivity and osteointegration support are additional advantages, being especially valuable in orthopaedic applications.

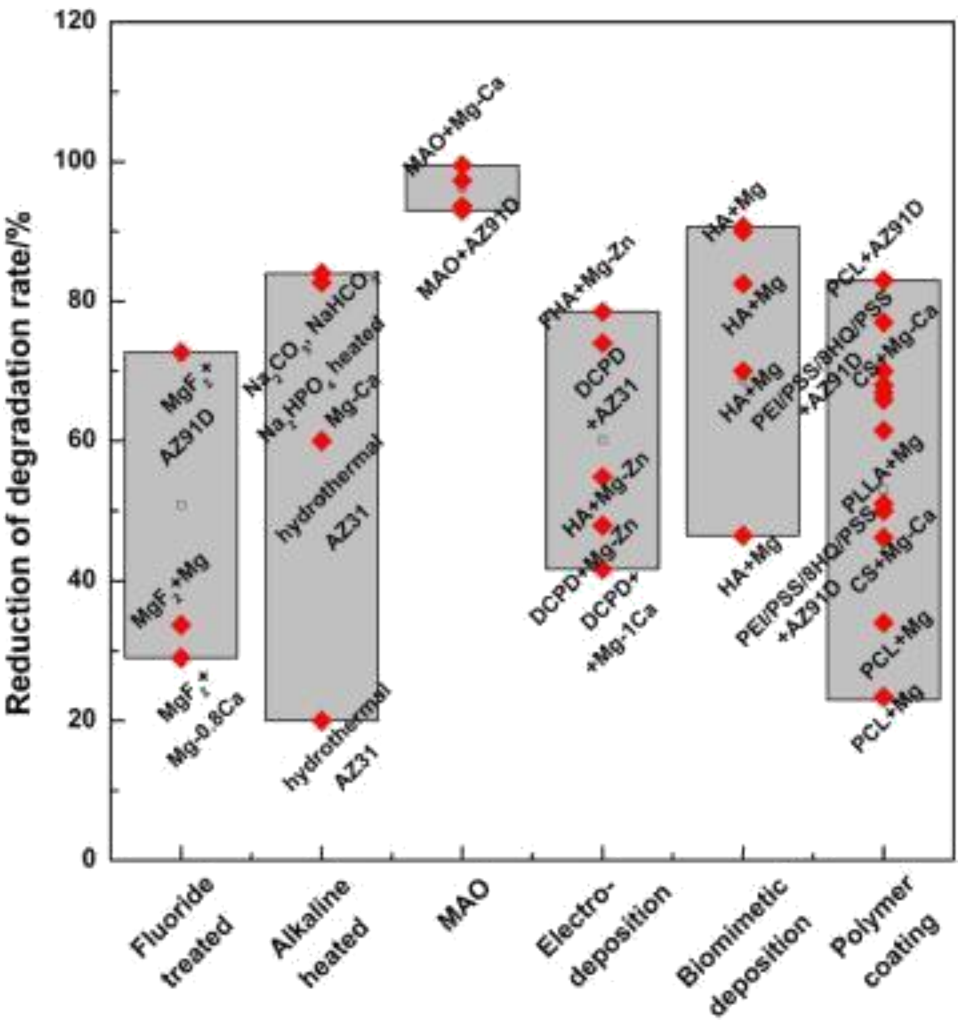

Figure 1.3: Comparison of the coating effectiveness on corrosion resistance of Mg alloys substrates.

A strategy to encompass both would be the use of biodegradable implant as Mg-based alloys [44– 47] that would re-sorbs in the body along with the bone healing. However, highly uncontrolled and rapid degradation rate in physiological conditions (pH 7.4) is still a major drawback of Mg-based material [48], leading to a high hydrogen gas production because of high aggressive ion concentration in the tissue surrounding, especially directly after implantation and before the formation of a protective degradation layer, influencing on a delay in the healing process [30,49]. Too rapid degradation can also result in a reduction of mechanical integrity and premature failure of the implant.

The research on the magnesium alloys for biomedical applications is interdisciplinary and all the field of researchers are focusing on the improvement of the biodegradable magnesium implants as shown in Figure 1.4.

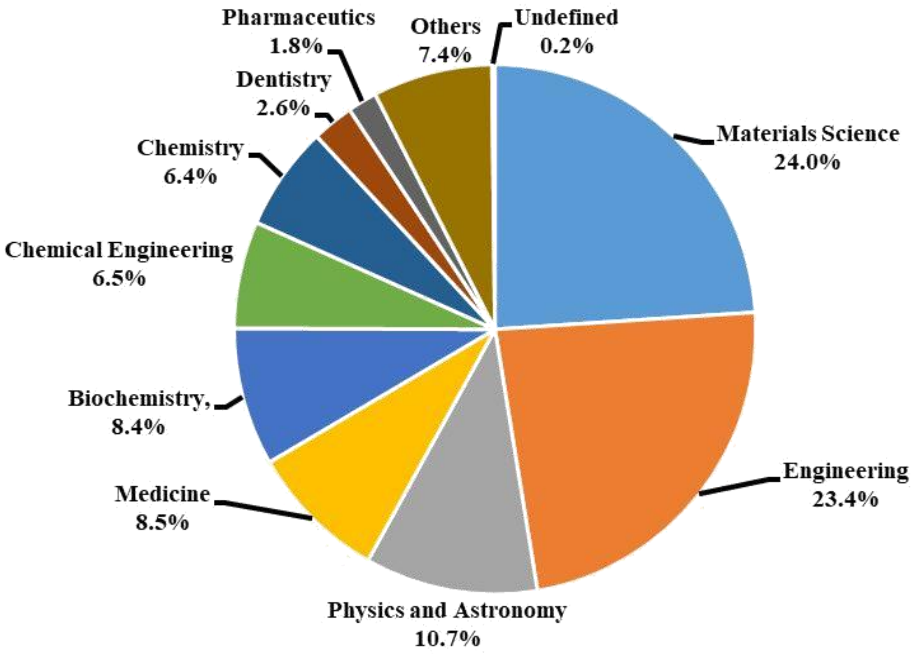

Figure 1.4: Publications on Magnesium as biomaterial country wise (source – Scopus search).

From the last few years, the following countries are focused on the research on the development of magnesium and magnesium for biomedical applications as shown in Figure 1.5.

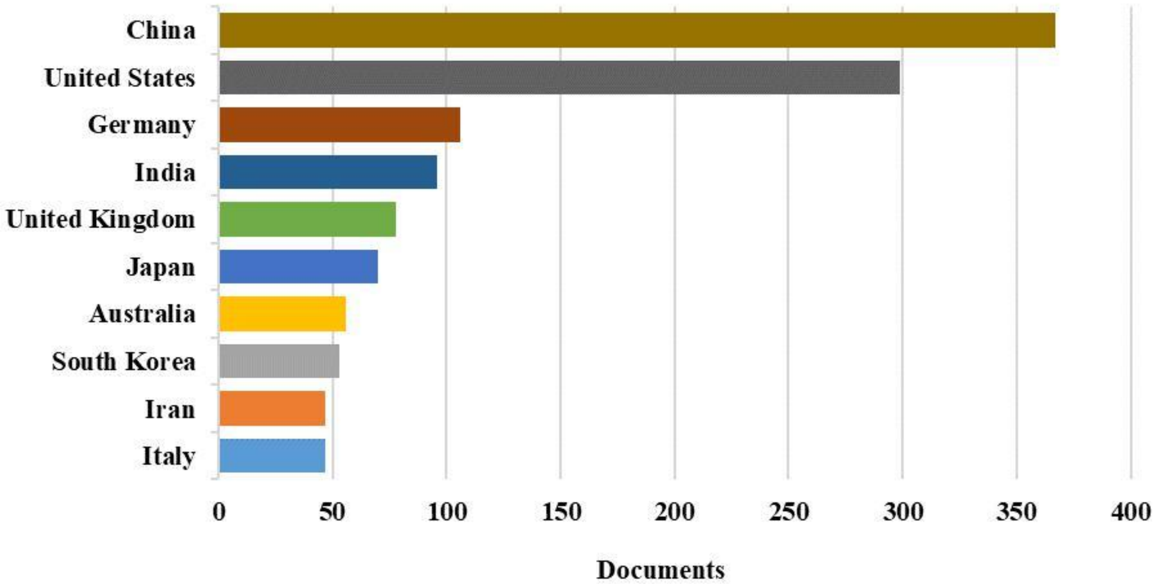

Figure 1.5: Publications on Magnesium as biomaterial discipline wise (source – Scopus search).

1.2. Objectives of the present study

The objectives of the present study are as follows :

- Evaluation of corrosion properties of Mg-4Ag and Mg-5Gd binary Magnesium alloys.
- Cross-linked Gelatin coatings on AZ91 Magnesium alloys for less corrosion and bioactive biomedical implant surface.
- Evaluation of corrosion properties for Electrospun Cellulose Acetate coated pure Magnesium Surface.
- Preparation of Porous Magnesium Monoliths by P/M processing followed by Chitosan coating and its effect on the physiological corrosion behavior.
- *In-vitro* Studies of Polydopamine/Gelatin surface modified Porous Magnesium monoliths to control degradation rate.

Chapter 2

2.1 Literature Review

Metallic materials continue to play an essential role in orthopaedic surgery, both as bone regeneration implants and as fixation devices. Among which stainless steel, cobalt-chromium, and titanium based alloys have been used for almost a century [50]. New developments and innovative methods were proposed to make these materials even more suitable. Mg is an element with a redox potential of -2.37 V, thus making it an active anode. This could be the main contributing factor towards its biodegradable nature. The biodegradability eliminates the need of second revision surgery which results in decreased costs and relief from pain to the patient. Other problem which is widely encountered for orthopaedic materials is mismatching of Young's modulus, when compared to of that of metal and bone, resulting in stress-shielding effect and loosening of implant. Young's modulus of Mg is closer to that of bone which removes stress shielding effect. In this context, Mg and its alloys have gained considerable attention recently due to their attractive features, including biocompatibility, biodegradability and bioresorbability [45,51], all being related to their light weight with an appropriate density (1.74 - 2.0 g/cm^3) as well as excellent mechanical properties and elastic modulus (41-45 GPa) [12,45,49,52–57].

Acting as temporary implants, Mg alloys can be dissolved within the body without the need for a second surgical intervention for their removal. However, too rapid degradation of Mg from Mg alloy in the presence of human body fluids, and subsequent loss of mechanical integrity before the tissue regeneration limits its application [56,58]. In addition to that, the simultaneous generation of H_2 and OH^- ions in the surrounding medium causes an increase of alkalinity, leading to a delay of the healing process at the implantation place, as well as tissue necrosis [59]. Many methods have been developed over the decades to combat these issues. The surface modification such as heat treatment, micro-arc oxidation (MAO) using plasma or electrolytes, phosphate treatment, alloying and ion implantation [59–63] were employed to control the degradation rate of the Mg alloy.

Various methods including surface dip- and electrophoretic- deposition coatings with biocompatible and biodegradable polymers as an attractive strategy [42,43,64–68] were also investigated without altering the alloy bulk properties. Although clinically acceptable synthetic poly (glycolic acid), poly (lactic acid) and their copolymers with tailored *in vivo* degradation rates and metabolically digestible degradation products [61,67–70] have been shown as highly potential material to act as a corrosion barrier, and additionally to deliver drugs, genes and growth factors at the body-implant interface [71,72]. However, the usage of natural biopolymers such as chitosan, albumin, hyaluronic acid, alginate, cellulose, gelatine, collagen, fibronectin, etc., were found to be more appropriate candidates due to the lack of highly acidic degradation products as well as their bioactivity and osseo-integration support, resulting in faster/improved biological interactions with the surrounding tissues [73,74], but haven't been fully explored yet.

2.2 Alloying elements

Another approach to improve the degradation rate, mechanical properties and *in-vitro* characteristics of the Mg based alloys is by alloying, i.e., addition of another elements in small quantities to the base metal (Mg). Currently, Aluminum, Zinc, Manganese, Silicon, Calcium, Strontium, Lithium, Silver, Bismuth, Zirconium and rare earth element (Gadolinium, Neodymium, Cerium and Dysprosium) have been investigated as alloying elements [1,75,76]. Among these, some common alloying elements are Aluminum, Calcium, Zinc, Strontium, Silicon, Manganese, Silver and Gadolinium. Aluminum is a common alloying element due to appearance of β $Mg_{17}Al_{12}$ phase, but it has detrimental effect on the human health as it can Alzheimer's disease. Calcium is the main component of hydroxyapatite and induces bone healing, thus a better choice as an alloying element, but the presence of secondary phase (Mg_2Ca) can potentially decrease the corrosion resistance of the alloy. Zinc is a crucial trace element for the human body and is necessary for many biological functions. Strontium is a component of human bone and has been known for promoting osteoblast. Sr has the ability to improve the mechanical properties and improve the corrosion resistance. Silicon can be tolerated in human body in small quantities and essential for the development of bone and connective tissue, however, Mg-Si alloys show low ductility and strength due to large Mg_2Si particle size and brittle eutectie phase. Manganese play an important role in metabolic activity of amino and carbohydrates. Rare earth elements are potential alloying elements as they can improve mechanical properties and decrease the degradation rate substantially [76]. Gadolinium has a large solubility limit in Magnesium (23.49 wt %) which facilitates the adjustment in mechanical properties by precipitation and solid solution strengthening [77]. Literature regarding corrosion behavior of Mg-Gd is scarce. The corrosion behavior of Mg-Gd binary alloy improves with an increasing amount of Gd upto 10 wt%. The presence of $Gd(OH)_3$ in the degradation layer contributes to the corrosion protection of the base alloy. Detailed researchs need to be carried out to understand the exact corrosion mechanism and *in-vitro* corrosion behavior of Mg-Gd alloy in order to be used for clinical purposes. The alloying of Mg with Gd was shown to improve the corrosion rate from about 0.75 mm/year for pure Mg to about 0.56 mm/year as well as to increase the mechanical strength of the implant (to tensile strength of 310 MPa, yield strength of 280 MPa, and ultimate elongation at peak hardness of 2.8%, at room temperature) [59,77–79]. Silver (Ag) contributes towards the faster degradation rates. Ag contributes towards the antibacterial properties of implant, metallic Ag pose the minimal risk to health and did not show any cytotoxicity. The addition of 2 wt% of Ag in Mg-Ag binary alloy increases the degradation rate. The Ag alloying addition of 4-6 wt % also exhibited similar results [80]. The use of antibacterial Ag as alloying element was also successfully implemented into Mg-alloys to improve its mechanical properties (i.e., compressive strength of 53 MPa and tensile strength of 55 MPa) as well as significantly reduces the corrosion rate up to about 0.36 mm/year [80–82] and to impart antibacterial activity while not reducing eukaryotic cells viability.

The present work has been carried out to evaluate the corrosion behaviour of Mg-5Gd and Mg-4Ag in SBF solution.

2.3 Biodegradable polymers

Besides several other coating techniques and components, the coating of biopolymers, such as chitosan and cellulose-based derivatives have been used to overcome the corrosion resistance, to provide new functionalities and mechanical support. The biopolymer coating has also been used as platform for the controlled release of molecules like drugs, proteins, and other active components. The potential uses of biopolymers in the surface modification of magnesium-based (pure metals and its alloy) and their impact on controlling the corrosion resistance are described in the following sections.

2.4 Surface modification with Gelatine

In particular, gelatine obtained by a controlled denaturation and proteolysis of fibrous insoluble protein, type I collagen, the major constituent of skin, bones, and tissues, shows high potential. This is mainly due to its good-accessible cell-recognition (i.e. arginine–glycine–aspartates, RGD) sequences of amino acids with osteo-inductive and osteo-conductive properties, which intensify the osteo-integration as well as three-dimensional tissue regeneration [73,83–85], while may simultaneously improve the anticorrosion properties and reduced adhesion of bacterial colonies [85]. Gelatine is currently used in pharmaceuticals, wound dressings and adhesives in clinics due to its good resorption *in vivo*, excellent cytocompatibility, non-antigenicity, plasticity and adhesiveness [86–88]. It has shown the potential to act also as a barrier surface layer for Mg alloys to decrease the corrosion of latter in many cases. For instance when applied with an electro-spinning and dehydrothermal post cross-linking method [89], by an impregnation with the co-embedded hydroxyapatite, and using a zirconia sol-gel [63], or by an emulsion solvent evaporation/extraction using the gelatine-PLGA hybrid and glutaraldehyde cross-linked nanoparticles [90]. All the coatings showed relatively high stability and strong binding capacity due to the good physical interlocking of GEL with the MAO layer which, however, may cause a deleterious influence on the corrosion protective ability; related to its high pore density which increased the effective surface area and the tendency of the corrosive medium to adsorb and concentrate in these pores [91,92]. Hence, it is not only essential, but also mandatory to increase the corrosion resistance of such coatings. On the other hand, the stability of the gelatine coating is decreased with subsequent incubation time, leading to swelling, deformation, and eventually delimitation from the alloy surface. Thus, further studies are needed to enhance the mechanical properties and the long-term corrosion protection ability of gelatine coatings.

2.5 Surface modification with chitosan

Chitosan is a linear and natural amino polysaccharide composed of β(1→4)-linked D-glucosamine residues and N-acetyl-glucosamine groups. It is derived by the partial deacetylation of chitin; the latter in turn is derived from shrimp and crustacean shell. The cationic chitosan is biocompatible, biodegradable and exhibits favorable biological properties [93]. These properties together with their natural availability makes chitosan an important candidate in several biomedical applications, for example, as corrosion inhibiting coating material for biomedical implants. In this section, only the recent works of corrosion resistance behaviour of chitosan coating on magnesium and its alloy are reviewed [94–102].

Zhang *et al*. deposited chitosan admixed with either calcium phosphate (CaP) or carbon nantubes (CNTs) on the surfaces of AZ91D magnesium alloy via an electrophoretic deposition (EPD) technique. They found out that the coating has improved the bioactivity and imparted increased cell viability [101]. The same author studied the *in vitro* corrosion of properties of CaP/Graphene/chitosan coated AZ 91D Mg alloy in the modified SBF solution. The immersion studies revealed that the coating improved the corrosion resistance of the alloy when compared to uncoated one. The electrochemical studies revealed that the corrosion current decreased from -1.554 V to -1.330 V vs. SCE. This result confirmed that the coating is stable for eight weeks, and the addition of graphene improved the bonding strength between the coating and the substrate. The presence of graphene in the coating has also enriched the cell viability than CaP/Chitosan alone [102]. Song *et al*. [103] developed self-healing coating based on gelatin-chitosan microcapsules containing $La(NO_3)_3$ for coating of AZ91D alloy. The coating has significantly improved corrosion resistance than that of uncoated alloy. Jia.*et.al*[64] proposed a non-toxic multilayer coating based on chitosan admixed with rare-earth element cerium (Ce) as inhibitor for Mg-1Ca alloy as shown in the Figure 2.1. The authors have demonstrated that the micro oxidation coating, as pre-treatment, not only improved the adhesion between coated layer and the alloy but also reduced the

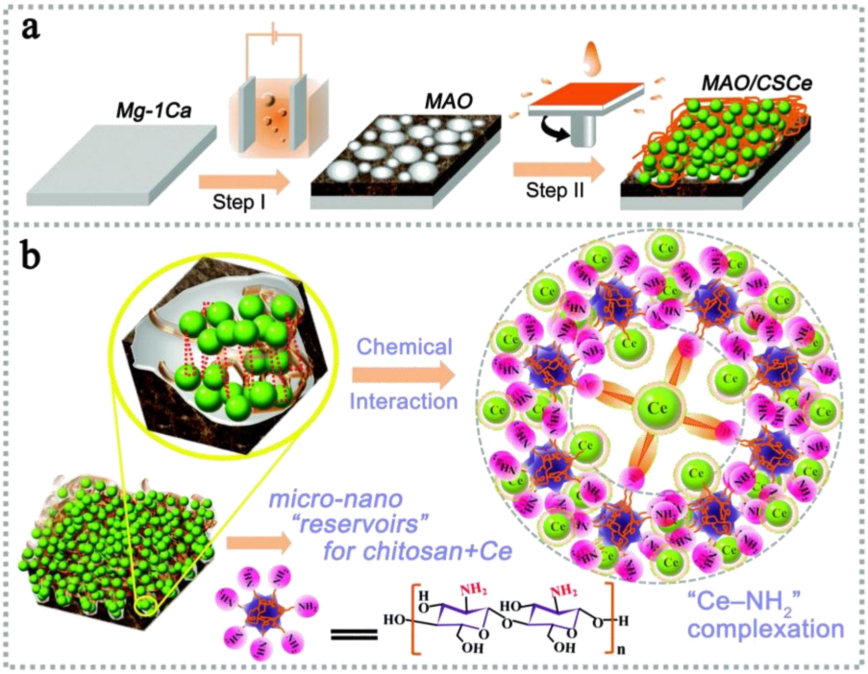

Figure 2.1: (a) Schematic of the coating fabrication process, involving (I) MAO treatment, and (II) spin-based assembling. (b) The structure of the resulting M-CSCe hybrid coating. Reprinted with permission from ref. [64] Copyright 2016 RSC.

rate of corrosion [57]. The electrochemical studies showed that the coating has one order magnitude higher impedance than the uncoated alloy. The immersion studies demonstrated that the pH values are reduced from 11.2 to 8.5 after the application of coating. Further, it has been found out that the biobased coating minimized the degradation rate and showed excellent cytocompatibility. A novel coating from chitosan-bioactive glass was developed and applied by electrophoretic process onto WE43 magnesium alloy by Heise *et al*. [97] The electrochemical studies performed in Dulbecco's Modified Eagle Medium (DMEM) showed that the coating improved the corrosion resistance. The bioactivity test illustrated the formation of inorganic compound hydroxycarbonateapatite on the surfaces of implant, which is beneficial for the bone healing.In a recent work of Pozzo *et al*. the corrosion protection properties of coatings of chitosan (2%, w/v) crosslinked with genipin (1, 3 or 6 mmol per mol of chitosan repeat units), which were applied on sheets of AZ31 magnesium alloy [104]. The authors have noticed a positive influence of the coating on the corrosion properties. For instance, the crosslinking process not only decreased the corrosion current considerably but also shifted the corrosion potential of the alloy to less negative value. This is an indication that the crosslinking process decreased the thermodynamic tendency toward corrosion as well as the rate of metal degradation. In another recent work, Córdoba *et al*. developed a functional bi-layer coating (inner layer: silane-TiO_2, top-layer: chitosan) to modify the surface of biodegradable implants such as AZ31 and ZE41 Mg alloys, for bone repair applications [105].

The results showed that the top layer chitosan biopolymers strongly influenced the composition of the corrosion products of both alloys, besides the entrapment of evolved H_2 gas forming gas pockets and delay in the release of hydrogen gas. In addition, in the presence of chitosan layer, the formed corrosion products such as $MgCO_3$ and $CaCO_3$ provided additional corrosion protection to the Mg alloys at longer immersion times (>3 weeks).

2.6 Surface modification with cellulose and its derivatives

Cellulose and their derivatives, the most abundant natural biopolymers on earth, have been used extensively for various biomedical applications. It is highly biocompatible and non-immunogenic, and shows good processability [106]. Therefore, recently, it has been used as protective coating for magnesium-based implants [107]. For instance, organo-soluble cellulose acetate was spin coated on magnesium implant and investigated to control the pH of the surrounding environment and to minimize the corrosion resistance of the substrate. In addition, the permeability of the coated membrane cellulose acetate was controlled by varying the concentration of underlying anchoring layer such as poly (N,Ndimethylaminoethyl methacrylate) (PDMAEMA), the positively charged polyelectrolyte, which limit the limiting the ion/H_2 flow [107].

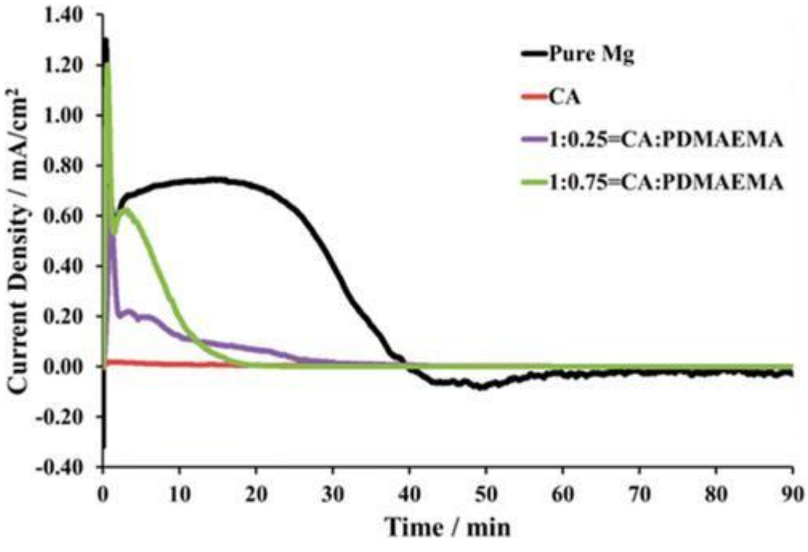

Figure 2.2: Polarization of the samples to −1.5 V vs Ag/AgCl in 0.1 M NaCl. Reprinted with permission from ref[107]. Copyright 2014 American Chemical Society.

They also found out that the corrosion rate can be altered by measuring the current density when the samples were polarized to a constant value near the open-circuit potential (OCP), i.e., −1.5 V vs Ag/AgCl. The current density profiles of the pure Mg and cellulose acetate coated samples are shown in Figure 2.2. While a high corrosion rate with a relatively high current density during the first 40 min is observed for pure Mg, the presence of the CA coating showed an almost passive behavior throughout the entire measurement time. In the case of coating that contained increasing amount of PDMAEMA content, higher current density was observed for the first 20 min after which the corrosion is minimized. The reduced corrosion after a short period of time, in this case, is assumed due to the accumulation of corrosion products between the membrane and the substrate surface [107]. Zhu *et al.*, investigated the use of composite made from aminated hydroxyethyl cellulose (AHEC) and hydroxyapatite (HA), as biocompatible coating material [108]. A clear difference in the surface morphology can be seen for composite coated substrate compared to that of pure one as shown in the Figure 2.3. The surfaces of AHEC coated AZ31 alloy showed a uniform and dense structure formation, and no scratches, while a homogeneous and consistent flake-like crystals and porous structure, essential for the simulation of osteoblast proliferation, were observed for the composite i.e., HA/AHEC-coated alloy. These surface features were altered upon incubation of the samples in SBF for one week where wide and deep cracks and

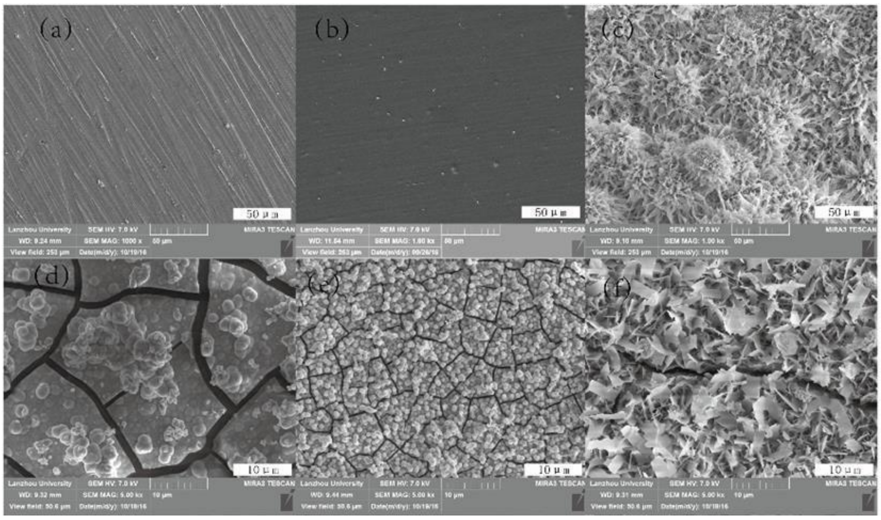

Figure 2.3: Scanning electron microscopy (SEM) images of AZ31, aminated hydroxyethyl cellulose (AHEC)/AZ31, and hydroxyapatite/aminated hydroxyethyl cellulose (HA/AHEC)/AZ31 specimens: before (a–c); and after (d–f) immersion in simulated body fluid (SBF) for 7 days. Reprinted with permission from ref [108]. Copyright 2017 MDPI.

pits were observed for HA coated alloy as with the pure alloy, and smaller cracks and pits with a more narrow and shallow structures were seen for composite coated surfaces.

The potentiodynamic polarization measurements demonstrated that compared to uncoated AZ31 alloy, the corrosion potential is increased to about 185 mV and the corrosion density is reduced up to 10 times than that of uncoated alloy. It is clear that the coated composite material reduced the corrosion rate, which decreased the corrosion ion concentration that are in direct contact with the surface of the AZ31 substrate. In addition, the composite coating also reduced the degradation speed in simulated body fluid (SBF) [108]. In another study, again cellulose acetate was dip coated onto a novel Magnesium-based alloy (Mg-1Ca-0.2Mn-0.6Zr (wt %)) by Neacsu *et al*.[109] The Scanning Electron Microscopy (SEM) measurements showed that the micro-scratches, on the alloy surface, arose from the motographic sample preparation, disappeared completely and a thin smooth layer of membrane with small-diameter pores and channels are created due to the application of cellulose acetate polymer coating as shown in the Figure 2.4.

The results revealed that the cellulose acetate coating improved the corrosion resistance of the alloy significantly in a physiological environment. Compared to uncoated implant, it also exhibited good cytocompatibility, by cell adhesion, viability and proliferation, and promotion of osteogenic differentiation [109]. Still, an important unresolved issue is the reduction of brittleness of implants. In this regard, Asl and their co-workers, developed a novel coating materials from the

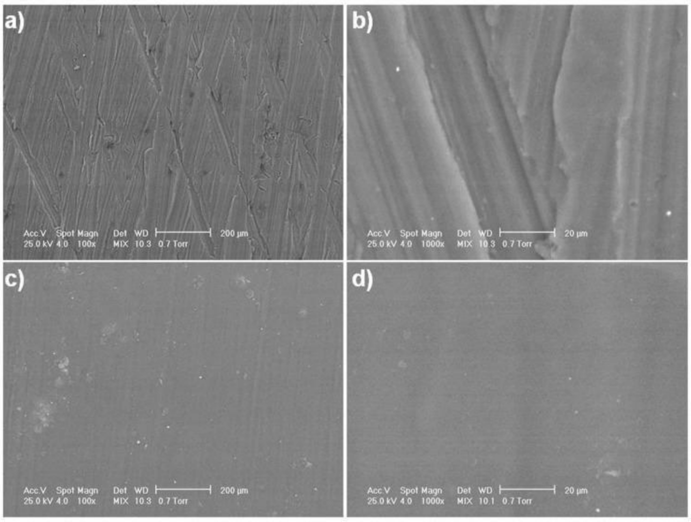

Figure 2.4: SEM micrographs of the uncoated and CA-coated Mg-1Ca-0.2Mn-0.6Zr alloy. Top view images of the uncoated (**a,b**) and CA-coated (**c,d**) alloy. Reprinted with permission from ref [109]. Copyright 2017 MDPI.

combination of carboxymethyl cellulose (CMC), polyacrylic acid (PAA) and calcium phosphate (Ca-P) [110]. Results from the nanoindentation measurements showed that the incorporation of polymers significantly improved the mechanical performance of the coating. For instance, the use of 0.2 wt % polymer in the deposition bath increased the Young’s modulus of coating close to the

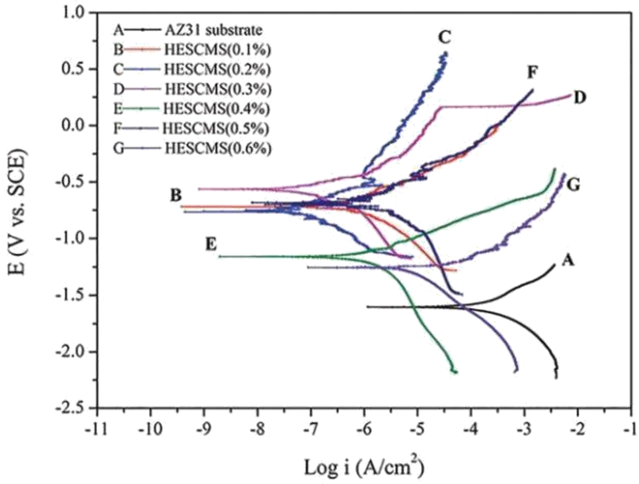

Figure 2.5: Corrosion performance of CMC composite coating measured by potentiodynamic polarization. Reprinted with permission from ref [110]. Copyright 2015 Wiley.

Mg substrate (PAA: 50 GPa, CMC: 47 GPa) when compared to inorganic Ca-P coating (98 GPa) and Mg substrate (41-47 GPa).[110]

The electrochemical measurements revealed that the corrosion resistance of polymer composite coated Mg-substrate was increased to approximately 1000-fold, as measured by corrosion current density. While variation in polymer concentration had no significant effect on the corrosion performance in the case of PAA composite coating, the composite coating prepared from CMC resulted in slightly decreased corrosion performance with increased CMC concentration as shown in the Figure 2.5 This was ascribed to coating morphology since the coating turned into slightly porous at higher polymer concentration.

2.7 Porous magnesium

In the recent years, there has been tremendous interest in bone tissue engineering studies in reconstructing the damaged bone tissue. Scaffolds with porous structure are extensively used in the bone tissue regeneration [37, 109]. Furthermore, their mechanical properties can be controlled by modification of their structure which reduces the stress shielding effect. Scaffolds are mainly made up of ceramics and polymers, but their mechanical properties are not suitable for load bearing applications [112]. To overcome this, metallic materials are recently introduced to the scaffolds. Iron, zinc and magnesium are the most commonly used porous biodegradable metals and they are suitable for orthopaedic applications. Recent studies on these metallic materials revealed that they can serve as load-bearing orthopaedic implants [40,113–116]. Magnesium dissolves in the human body which helps in healing of the tissues, thus eliminating the need for a second surgery, which saves cost and time. As mentioned before, the major limitation is the rapid degradation of magnesium, which increases pH of the body fluid [35]. Surface modification is one of the efficient procedure to control the degradation of magnesium [117].

Recently, Mg porous scaffolds coated with different polymers and composite coatings [15,16,118–121] for the improvement of bioactivity and corrosion resistance, were extensively investigated . Here, a gelatine coating was applied to the Mg scaffold surface to improve its corrosion resistance, and a thin PDA layer prepared between the Mg scaffold and GEL layer to obtain better corrosion properties. The formed PDA/GEL layer not only acts as an intermediate layer but also serves as a barrier layer to control the dissolution of magnesium, and promotes the apatite formation, which is more helpful for the tissue engineering applications. Gelatine (GEL) is a natural biopolymer derived from collagen, which is biodegradable and biocompatible [122,123], has good cytocompatibility, and good corrosion protection [42], and is readily available with low cost. The formed hydroxyapatite (Hap) on the GEL coated surface enhances the mechanical properties of the scaffold and improves its biological interactions [120,124,125]. Polydopamine(PDA) is a biocompatible and biodegradable material useful for the biomedical applications [126,127]. PDA is a polymer containing amine and belonging to catechol groups useful for the bioconjugation [126,128,129]. It is used for surface modification of biomaterials [130] since it creates an adherent layer on the surface [131], having good stability, and acts as corrosion resistant coating [121,129]. This coating is helpful for the biomineralization process, which is suitable for the bone tissue applications and promotes protein adsorption [132,133]. The PDA layer also acts as a good intermediate layer between the surface and the coated polymer, and improves the stability of the coating [62,131,134]. It has been proven that the PDA coating improves the corrosion resistance on the magnesium surface [121,135–137].

In the present work, the corrosion properties were evaluated for Binary Magnesium alloys (Mg-4Ag and Mg-5Gd). Pure Mg was coated with electrospun Cellulose Acetate and was further characterized for corrosion properties. AZ91 Mg alloy was modified with Gelatin coating for a less corrosive and bioactive surface. The porous Mg monolith were produced via P/M method and further coated with organic biopolymer Chitosan and Polydopamine/Getain via depositing coated procedure.

Chapter 3

3.1 Experimental Procedure

In order to fulfil the objectives of the present investigation, the required fabrication methods and characterization techniques have been discussed in this chapter. Further to have a better understanding of the research results, various materials characterization techniques were used, and the conditions and parameters considered during these techniques are explained along with the equipment on which these properties are evaluated are mentioned briefly.

3.2 Materials

Pure Mg, Mg-4Ag and Mg-5Gd alloys were heat treated and extruded as rods having 10 mm in diameter and with 1.5 mm thickness by Helmholtz-Zentrum (HZG), Geesthacht, Germany. For the preparation of the Simulated Body Fluid (SBF) solution of pH 7.4 as shown in Table 3.1. The chemical composition of the alloys has been shown in Table 3.2. Analytical grade Mg powder (99.9 % purity; size <100 µm), ammonium bicarbonate (NH_4HCO_3), and low molecular weight chitosan (deacetylation degree of 75-85 %) were purchased from Sigma Aldrich. Gelatine (GEL) type B (About 5 PI, confirmed through potentiometric titration, 47 32 kDa Mw as ascertained through Gel Permeation Chromatography), l,1-ethyl-3(3 dimethyl aminopropyl)-1-carbodiimide hydrochloride (EDC), and N-hydroxysuccinimide (NHS).. The following reagents were dissolved in to 1000 mL of ultrapure water (Milli-Q, Millipore Corporation, Massachusetts, USA) with resistivity of 18.2 cmAll the chemicals were purchased from Sigma Aldrich and used as received without further purification. Cellulose acetate (CA), with Mn=30.000 and acetic acid (≥99.8%) were kindly supplied by Sigma Aldrich.17 wt% cellulose acetate (CA) solutions were prepared by dissolving appropriate amount of CA in 75% concentrations of acetic acid. The solutions were stirred until a homogenous mixture was obtained.

Table 3.1: Composition of Simulated Body Solution (SBF).

S. no.	Reagents	Amount in 1000 ml
1	NaCl	7.996 g
2	NaHCO3	0.355 g
3	KCl	0.225 g
4	K2HPO4.3H2O	0.231 g
5	MgCl2.6H2O	0.311 g
6	1.0 M HCl	39.0 ml
7	CaCl2	0.292 g
8	Na2SO4	0.072 g
9	((HOCH2)3CNH2)	6.118 g
10	1.0 M HCl	Appropriate amount for adjusting the pH~7.4

Table 3.2: Chemical composition and density of Mg, Mg-4Ag and Mg-5Gd used through the study as specified by the supplier.

Alloy	Gd (wt. %)	Ag (wt. %)	Fe (ppm)	Ni (ppm)	Si (ppm)	Mn (ppm)	Co (ppm)	Cu (ppm)	Al (ppm)	Mg	Density [g/cm3]
Mg	-	-	46	4	130	334	<1	14	45	balance	1.740
Mg-4Ag	-	3.88	58	5	79	51	<1	<10	54	balance	1.785
Mg-5Gd	4.99	-	50	6	63	57	<1	<10	41	balance	1.786

3.3 Immersion tests

The Mg samples were ground with SiC papers (provided by Struers, Ballerup, Denmark) with 2000 grits, washed by ultrapure water and then dried it out by the nitrogen stream. Before and after immersion weight of the samples have been measured. They were immersed in 25 mL SBF solution at 37 0.5 °C that was constantly shaking at 100 rpm for 28 days. After every 7 days, the immersed samples were taken out from the solution, treated with the solution comprising of 200 g L^{-1} CrO_3+ 10 g L^{-1} $AgNO_3$ for 5 min[138], cleaned with distilled water and dried. The pH changes of the immersing solutions were also measured during the immersion test for each respective degradation period. Five samples were tested for each group. The corrosion rate *in-vitro* is calculated (mm/y) using the equation as follows [139]:

$$\textbf{Corrosion rate} = \mathbf{K} \times \quad \boldsymbol{m} / (\boldsymbol{A} \times \boldsymbol{t} \times \boldsymbol{\rho})$$

Where the time conversion coefficient K = 8.76 × 10^4, *m* is weight (g) difference before and after immersion, *A* is sample area (cm^2) exposed to solution, *t* is the immersion time (h), and *ρ* is the sample density (g/cm^3) as given in Table 3.1. The collected liquid samples were analyzed for Mg^{2+} ion concentration by ICP-OES (Agilent 720 ES).

3.4 Attenuated Total Reflectance Fourier Transform Infrared (ATR-FTIR) spectroscopy analysis

ATR-FTIR spectroscopy analysis was performed to identify the potential mineralization process of the samples after the incubation in SBF. The spectra were collected at 4 cm^{-1} resolution during 16 scans in a range of 4000 cm^{-1} to 450 cm^{-1}. The air spectrum at background was deducted. The data acquisition analysis was done using the software programme of Spectrum 5.0.2. Fourier self-deconvolution was carried out on FTIR average spectra in amide I region (1600 - 1700 cm^{-1}) by applying 1.8 resolution enhancement factor, which provide information for peaks number along with location. Afterward, Peak Fit. v4.12 program software is used for curve fitting.

3.5 X-Ray Diffraction (XRD) analysis

A D4 Endeavor is used for phase identification based on X-ray powder diffraction, which is Cu K_a radiator (wavelength of 0.15406 nm) Bruker AXS diffractometer and Sol-X energy-dispersive X-ray spectroscopy (EDXS) sensor with the angular range 2Θ of 10º and 80º, the 0.02º step size and 3 seconds counting time.

3.6 Scanning Electron Microscopy (SEM) imaging and EDXS analysis

SEM imaging coupled with EDX detection system was also perform on samples, before and after the coating process, same as after SBF incubation, using the microscope Sirion NC 400, equipped with

EDX detector. EDX analysis was performed in uppermost (coating-related) section to inspect the presence and type of deposited formations.

The surface morphology of differently porous monoliths after each heat treatment as well as after 48h of SBF incubation was examined by SEM imaging on upper surface with the microscope FEI Quanta 200 3D using back-scattered modes and different magnifications. Images were further analysed by ImageJ program to obtain quantitative information regarding grain size, same as semi-qualitative information about porosity and interconnectivity on the surface.

3.7 Electrochemical measurements

Electrochemical measurements of alloys were performed in 1.0 L SBF solutions at 37 0.5°C. The samples were first ground by 2000-grit paper water stream (Struers, Ballerup, Denmark), afterwards, ultrasonically threshed in a bath of 50 vol.% acetone/50 vol.% ultrapure water. Before the measurement specimens were cleaned by ultrapure water and dried. Electrochemical measurements were carried out in a three-electrode system with stagnant circumstances. The prepared specimens were embedded in a Teflon holder and used as the working electrode. A saturated calomel electrode and a graphite rod were working as a reference electrode and a counter electrode respectively. Measurements were accomplished by Autolab PGSTAT204 potenctiostat/galvanostat, which was controlled by Nova 2.1.2 electrochemical program. A 72h procedure was employed. The procedure started with 1h chronopotentiometry measurement at zero current, which was followed by electrochemical impedance spectroscopy (EIS) measurement. EIS measurements were performed also after 3, 5, 36, 48, 60 and 72 h of immersion. Chronopotentiometry measurements have been performed in between the EIS measurements which assisted the stabilisation process. Electrochemical impedance spectra were acquired at E_{OC} (open circuit potential) in 0.1 MHz - 5 mHz frequency range with 10 points by a group of ten and peak to peak amplitude of 10 mV of the excitation potential. The ZView2 program was used for fitting the EIS measured data.

Cyclic polarisation measurements have been carried out subsequently 72 hours of immersion starting at -0.25 V more negative potentials than E_{ocp} and going in the anodic direction using 0.1 mV/s sweep rate. The potential scan was reversed when the current reached a value of 1.0 mA. The cyclic polarisation measurement was finished at potential of -0.25 V more negative that the repassivation potential. The potentiodynamic polarization curves were recorded by automatically changing the electrode potential, starting from 250 mV vs. open circuit potential (E_{ocp}) and continued with increasing potential in the anodic direction by the potential scanning rate of 1 mV/s. Impedance spectra have been recorded at E_{ocp} in between 100 kHz and 10 mHz frequency range by 10 points by a group of ten and the peak to peak amplitude of 10 mV of the excitation potential.

3.8 Electrospinning

Electrospinning process was conducted using pilot-scale electrospinning aparatus ElMarco Nanospider NS LAB 500. In comparison to widespread single needle electrospinning, with low production rate 0.1 – 1 g/h, used Nanospider has the production rate of up to several 10g/h. ElMarco Nanospider is a needle-less electrospinning apparatus with a high voltage power supply (up to 80 kV), feeding unit (a bathtub with rotating electrode – cylinder or wire) and a grounded collector (cylinder or wire electrode), seen in Figure 3.1. When an external electric field is applied, a polymer solution, covering the rotating electrode, is charged, causing the formation of conical droplets, due to the equilibrium of polymer surface tension with applied electric field. With increasing voltage, the electric field overcomes the polymer solutions` surface tension and the jets start to form spontaneously on a free liquid surface, ejected in their optimal position. The polymer jets solidify as they travels towards the collecting electrode and are coated on Magnesium sample attached to the nonwoven fabric on support material.

All nanofibrous samples were electrospun at constant conditions; distance between electrode and the collector plate was 160 mm, applied voltage was 75 kV, time of electrospinning was 40 min, while temperature and humidity of working environment was kept at 20°C and 30%, respectively.

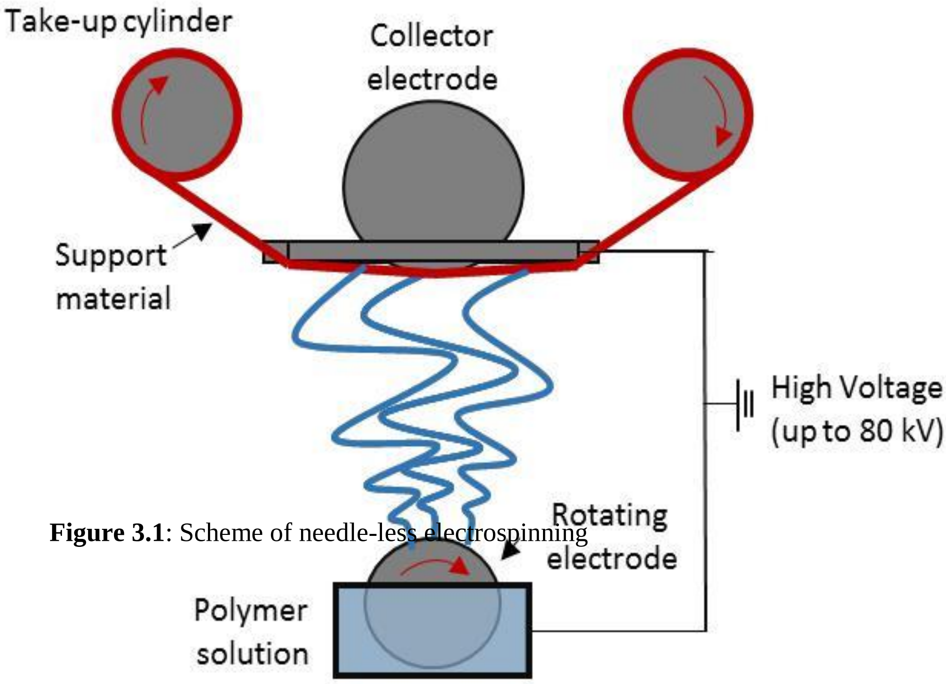

Figure 3.1: Scheme of needle-less electrospinning

3.9 Processing of porous Mg monoliths

Porous Mg monoliths were prepared by powder metallurgy (P/M) process (sintering) using NH_4HCO_3 powder as a space holder material. Liquid hexane was added to avoid the segregation of powders at a volume fraction of 30%. The Mg and NH_4HCO_3 powders were thoroughly mixed according to weight content of NH_4HCO_3 (i.e. 0, 10 and 20 wt. %, respectively). The mixture powders were uniaxially cold-pressed under pressure of 265 MPa into cylindrical green compacts with 13 mm in diameter and 16 mm in thickness. The obtained monoliths were treated further by a two-step heat treatment: (I) T=130°C for 4 h and (II) 550°C for 6 h, under an argon atmosphere in order to burnout the spacer particles and merge the Mg particles into larger grains. The percentage of porosity (P) in the sintered samples was determined according to the following equation [140] $P = (1 - \rho/\rho_s) \times 100\%$ where ρs is the density of Mg and ρ is the density of the porous Mg sample, being determined as volume/mass ratio.

3.10 Chitosan coating

Mg monoliths were ground with SiC abrasive paper down to 1200 grid, rinsed ultrasonically in EtOH and dried in air. Chitosan (1% w/v) water solution was prepared being adjusted to pH of 5.8–6.0 by using HCl and NaOH. The chitosan solution was applied on the surface of porous Mg samples by dip coating procedure at room temperature.

3.11 DOPA/GEL treatment

Dissolved dopamine hydrochloride (2mg/mL) in 10 mM Tris– HCl (pH 8.5) is used for protecting the changes of pH solution and pH-induced oxidation changes the solution colour to dark brown. After that, cleaned monoliths have been dipped into the alkaline dopamine solution. Before GEL-treatment, the Mg monolith was removed after 24 hrs and washed with deionized water and dried it out using stream of nitrogen. The 10 w/v% GEL concentrated solution was produced, solubilised by calm stirring at about 50˚C. EDC and NHS are mixed in the GEL solution with molar ratio of 4/1, which are used for cross-linking of GEL macromolecules. The coating mixture was applied to the surface of the PDA coated Mg Monolith by dip coating procedure. The sample was rinsed with deionized water and dried.

3.12 In *vitro* degradation study

The prepared cylindrical-shape Mg monoliths were weighed (W_i) and submerged into 25 ml of SBF solution of pH 7.4, and the immersion was carried out at 37 0.5˚C with constant shaking at 100 rpm up to 120 hours. At each time point (24, 48, 72, 96 and 120 h, respectively), the submerged samples were taken out from the solution, rinsed gently with deionized water, dried at room conditions for 24 hours and weighed (W_t). The weight loss was calculated according to the following equation: *weight loss* = $(W_i-W_t)/W_i \times 100$ %. The pH changes of the immersing solutions were also measured for respective degradation period. Three samples for each group were tested.

3.13 Compression testing

Uniaxial, unconfined compression test was performed by Shimatzu AG-X plus compression testing machine with 10 kN load cell, according to ASTM E9 standard [141]. The test was performed by displacement control with an applied rate of 1 mm per minute. Before testing, dimension of each sample were measured for calculation of stress (N/mm^2) and strain (%) data, being normalised the measured force (N) and stroke (mm) with surface area (mm^2) and initiate thickness (mm), respectively. Applied forces by dimensional changes is calculated to get compressive modulus along with the slope of the linear region of the stress-strain curve. The maximum stress point (MPa) in the stress-strain curve is used to get the compressive strength.

Chapter 4

Results and discussion

4.1 Degradation and electrochemical corrosion behavior of Mg4Ag and Mg5Gd alloys under *in-vitro* conditions

Figure 4.1 shows the optical micrographs of pure Mg, Mg-4Ag and Mg-5Gd. The average grain sizes were measured by linear intercept method as 35 ± 10.7, 41.6 ± 11.7 and 19 ± 7.2 μm respectively. From the images, it can be observed that no secondary phase appeared at the grain boundaries in considerable amounts. Numerous twins were observed in Mg and Mg-4Ag, which is common in Mg alloys.

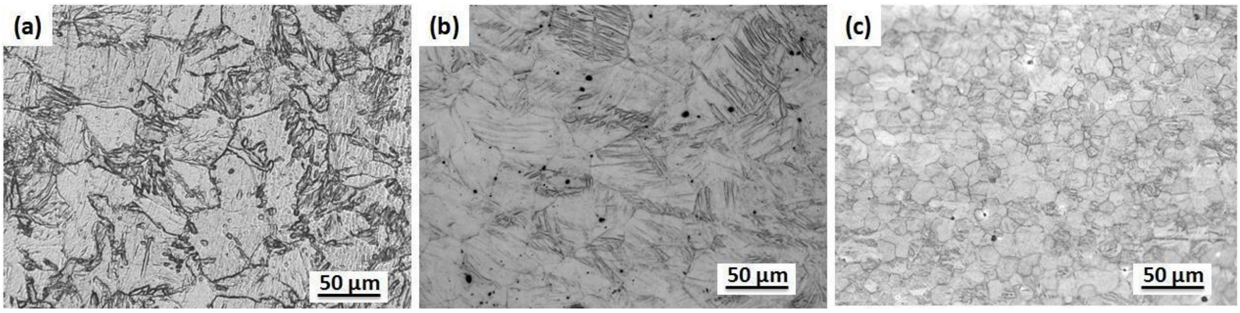

Figure. 4.1: Optical micrographs of a) pure Mg b) Mg-4Ag, and c) Mg-5Gd.

However, Mg-5Gd alloy has smaller grains without significant number of twins. The micro hardness was measured as 42.5 ± 2.6, 68.0 ± 4.1 and 69. 2 ± 3.5 Hv for Mg, Mg-Ag, and Mg-Gd samples respectively. Compared with pure Mg, both the alloys have shown higher hardness which is presumably due to the alloying effect. Interestingly, the increase in hardness was almost the same for Mg-Ag and Mg-Gd alloys.

4.1.1. *In vitro* degradation behavior

The alloys were incubated in the SBF solution at 37±0.5˚C for 28 days, and the pH values of the solutions were monitored as well as corrosion rates were calculated based on the weight loss measurements, followed by quantification of Mg-ions released using ICP-OES as well as ATR-FTIR, XRD and SEM-EDXS analysis.

As may be seen from Figure 4.2, the pH values of SBF solutions with incubated alloys, obviously increases with the immersion time in all the samples, however, the increase is significant for pure Mg compared to Mg-4Ag and Mg-5Gd samples. After four weeks of immersion, the pH value for the pure Mg reaches pH of about 9.5, while that for Mg binary alloys between pH 8.3 - 8.5, the lowest for Mg-

5Gd alloy throughout the incubation period. The measured pH value indicates the release of Mg^{2+} ions [142], which is obviously which is lower in the case of binary alloys.

The corrosion rate Figure 4.3 of pure Mg alloy is also much faster compared to the other binary alloys, reaching a value of 3.34 0.01 mm/y and 0.62 0.04 mm/y after 7 and 28 days of incubation, respectively, whereas, after 28 days ,117.06 0.08 mg/L of Mg^{2+} ions were released. The corrosion rates are decreased in case of Mg-4Ag and Mg-5Gd alloys, reaching a value of 2.05 0.02mm/y and 0.3 0.05mm/y and a release of 65.07 0.06 mg/land 62.36 0.02 Mg^{2+} ions, respectively after 28 days of incubation. The corrosion rate for Mg-4Ag alloy is a bit different compared to Mg-5Gd, showing a higher value initially and decreased slowly after 28 days, reaching the same value. This indicates that a different mechanism exists for alloys during degradation as well as corrosion.

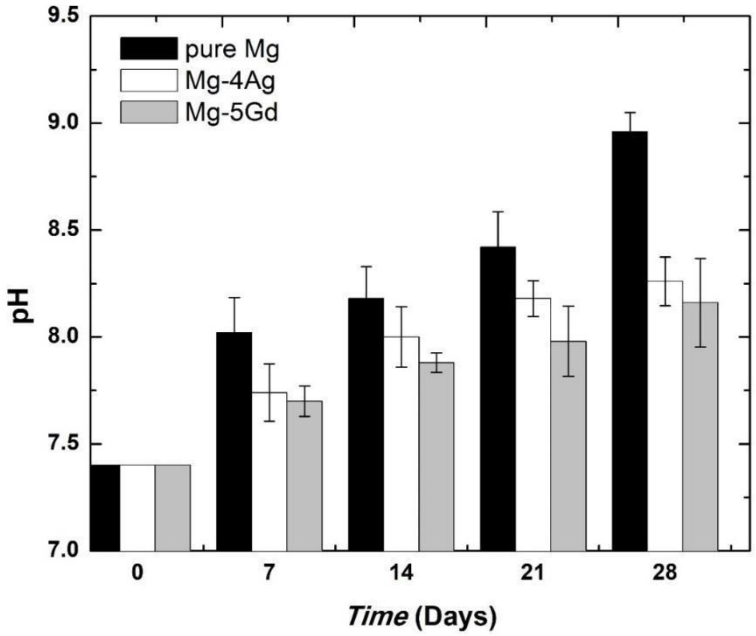

Figure 4.2: pH values of the SBF solution followed by immersing of alloys up to 28 days at 37 0.5˚C.

The ATR-FTIR spectra in the Figure 4.4 for Mg and binary alloys after 28 days of incubation showing the foremost existence of both absorption bands at around 3840-3270 cm^{-1} and 1650-1700 cm^{-1}, attributed to the stretching mode of OH^- associated with $Mg(OH)_2$ and bending mode of adsorbed water molecules, respectively, [143,144]. Moreover, the band at about 2300 cm^{-1} confirms directly adsorbed CO_3^{2-} vibration bands, which can also be seen from the peaks at about 1400-1500 cm^{-1} and 875 cm^{-1}[145]. In addition, a band at 729 cm^{-1} may be associated with the in-plane deformation and out-plane deformation modes of the present $CaCO_3$ [146]. Moreover, the peaks at about 475, 568, 606, cm^{-1} can be confirmed as the bending vibrational bands of PO_4^{3-} ions, while a sharper absorption band at around 1100-1000 cm^{-1} corresponds to the symmetric and asymmetric stretching of PO_4^{3-} respectively [147].

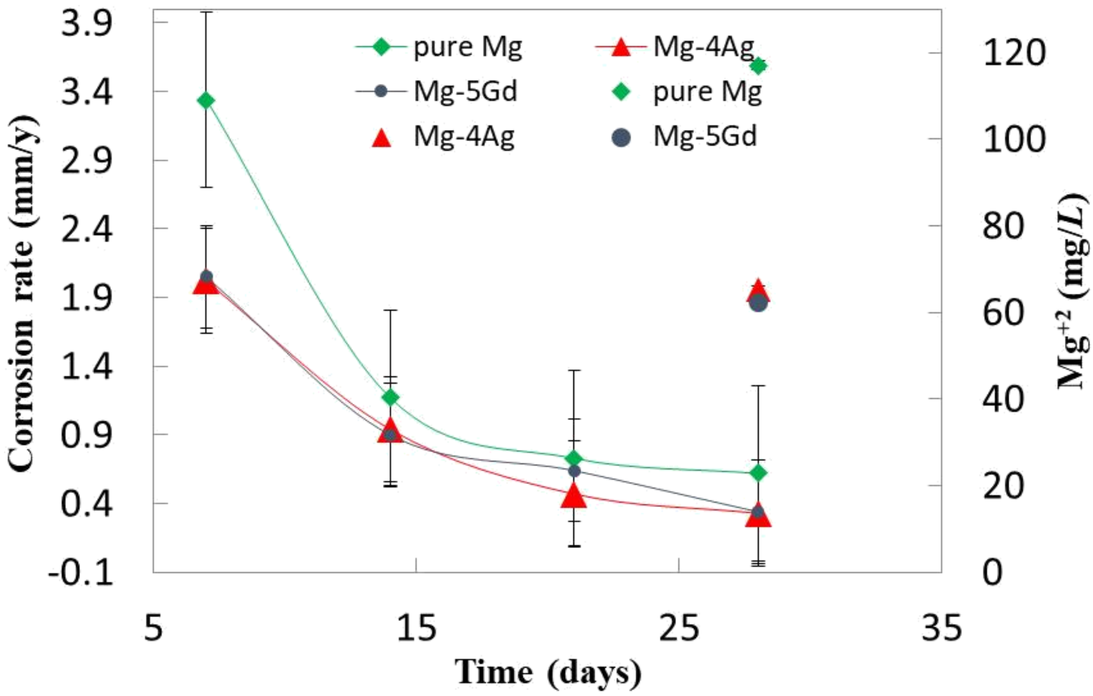

Figure 4.3: Corrosion rates of alloys and Mg-ions release after immersion in SBF solution at 37 0.5˚C for 28 days.

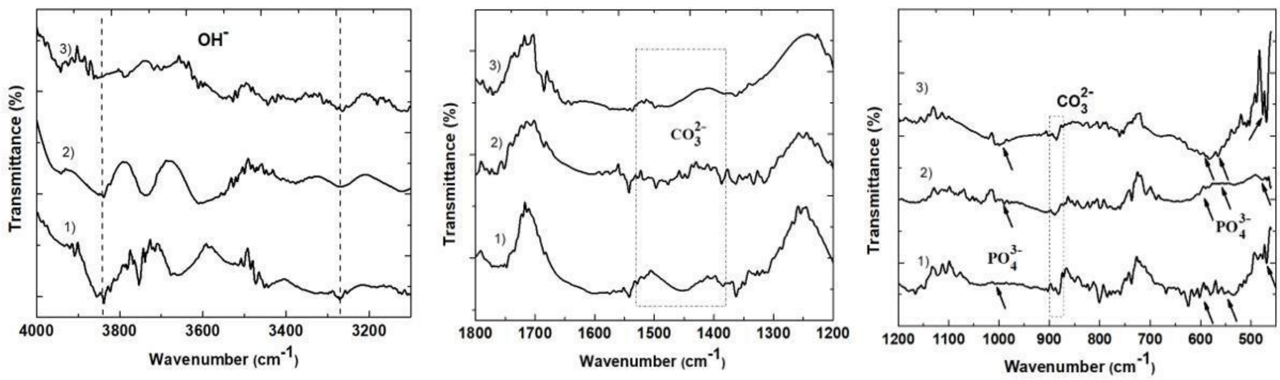

Figure 4.4: ATR-FTIR analysis of 1) pure Mg 2)Mg-4Ag 3)Mg-5Gdalloys after 28 days of incubation in SBF solution at 37 0.5˚C.

The XRD pattern in the Figure 4.5 of the alloys after 28 days of incubation in SBF revealed the presence of hexagonal closed-packed crystalline structure of Mg alloy as confirmed by the peaks at around 32,70, 36.40º, 47.75º, and 57.40º corresponding to the Mg (JCPDS 01-089-7195), and the peaks at 38.21º and 44.16º arise from the MgO (JCPDS 00-030-0794) formed. In the case of both binary alloys, the formation of $Mg(OH)_2$ components are indicated by the peaks identified at 18.5º, 37.50º, 50.69º and 58.79º (JCPDS 01-084-2163), and Ag presence is confirmed at 44.2º ((JCPDS 00-001-1164) for Mg-4Ag alloy. In case of all alloys, the characteristic peaks at 32.25º and 34.46º (JCPDS 00-001-1008), corresponding to an appetite structure are also identified, however much less intensive peaks are formed for both binary alloys compared to pure Mg , which may be of more amorphous in nature.

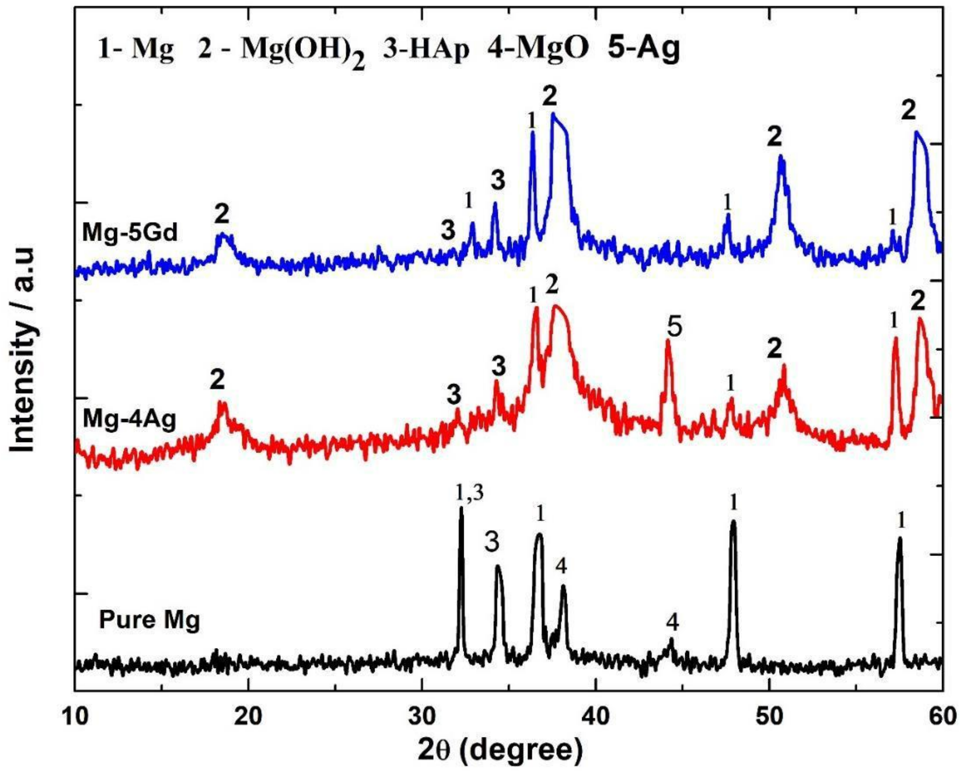

Figure 4.5: XRD analysis of alloys after 28 days of incubation in SBF solution at 37 0.5˚C.

The SEM images of pure in the Figure 4.6 and binary alloys surface in the Figure 4.7 and corresponding EDX measurements Table 4.1 were shown before and after 28 days of incubation in SBF at 37 0.5˚C.

The images of pure Mg alloy in Figure 4.6 revealed the formation of pits with cracks incorporated within the structure, covered with the corrosion products. The corrosion products formed at the surface are not homogenous and some are like needle shaped clusters which are characterized by Mg, C, O, Cl, P, Ca, and Na ions by the EDS are present in Table 4.1. The presence of Cl ions compared to the other elements indicates on the formation of $MgCl_2$ [65] via the reaction of chlorides with oxide (MgO) products, leading to a more dissolution of Mg [148].The formation of CaP apatite structures may be also identified due to the presence of Ca and P, which on the other hand helps to protect the surface and thus decreases corrosion rate [149].

In the case of Mg-4Ag and Mg-5Gd alloys, thick and homogenous porous layer in the Figure 4.7 with the formation of different shaped products were observed, mainly structured from Mg, C, O as well as P and Na ions in case of Mg-5Gd alloy, however, with different ratios and without the presence of Cl ions, indicating that the surface is protected by the other structures being formed. Gd incorporated in Mg-5Gd alloy may reacts with the Cl ions, leading to the formation of $GdCl_3$ as well as further interacting with phosphate ions [150], which is additionally responsible for a decreased corrosion rate, correlating well with the results in Figure 4.3. The Gd element has higher affinity to oxygen when compared to Mg by forming a Gd_2O_3 or $MgGd_2O_4$, which helps the formation of Mg layer from further degradation [151]. There is a possibility of forming secondary phase (precipitates) of Mg_5Gd at the grain boundaries [152– 154], which protects the surface from pitting corrosion, and strengthen the alloy resistance.

On the other hand, the EDS analysis of Mg-4Ag alloy shows much less ratio between O and Mg *vs.* C, compared to Mg-5Gd alloy, indicating the formation of secondary phases like Mg_4Ag or $Mg_{54}Ag_{17}$ [81], acting as a protective layer on the alloy surface and thus further inhibits the degradation rate.

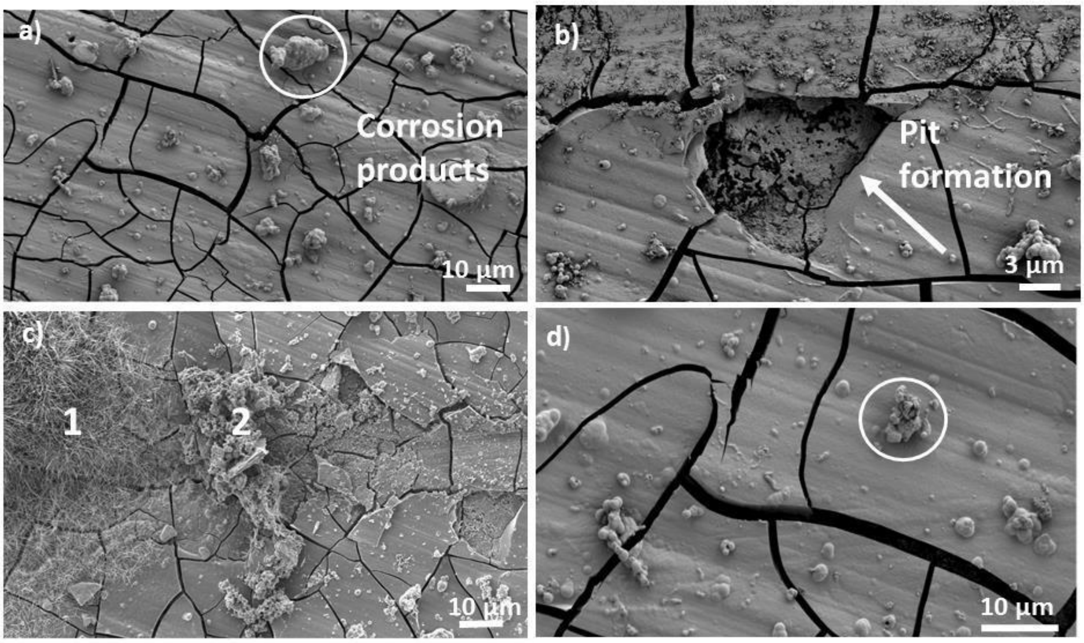

Figure 4.6: SEM images of pure Mg alloy surface showing on the formation of (a,d) corrosion products and cracks, (b) pits and (c) clusters.

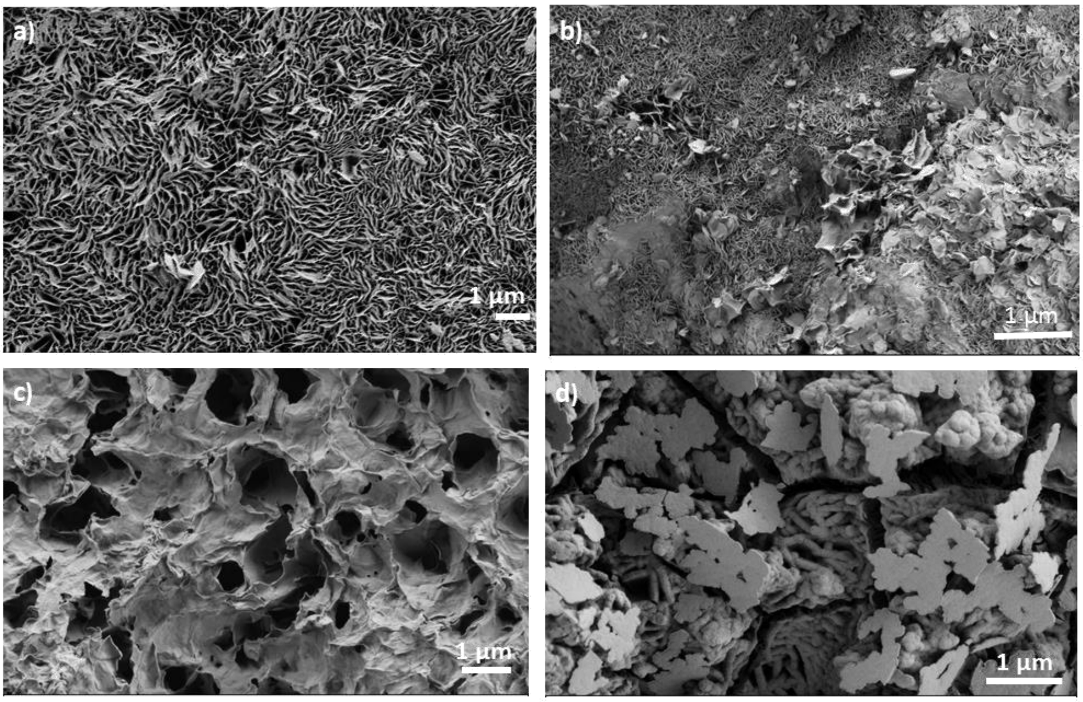

Figure 4.7: SEM images of (a, b) Mg-4Ag and (c, d) Mg-5Gd alloys surface, after 28 days of incubation in SBF at 37 0.5˚C.

Table 4.1: EDS analysis of alloys after 28 days of incubation in SBF at 37 0.5˚C.

Elements (wt%)	Pure Mg	Mg-5Gd	Mg-4Ag
Mg	18.98 3.88	29.86 1.93	30.43 0.74
C	5.66 1.15	11.14 0.94	12.30 0.70
O	54.04 3.35	58.07 2.53	55.78 0.41
P	5.73 3.84	0.25 0.11	-
Ca	6.22 4.11	-	-
Na	1.20 0.82	0.66 0.26	-
Cl	6.75 3.69		
F	0.48 0.47	-	-
Ag	-	-	1.47 0.76

4.2 Electrochemical behavior

4.2.1 Electrochemical Impedance Spectroscopy (EIS) measurements

EIS studies were carried out for pure Mg, Mg-4Ag and Mg-5Gd. In the Figure 4.8 shows Nyquist spectra for pure Mg, Mg-4Ag and Mg-5Gd measured after 1 h, 3 h, 5 h, 36 h, 48 h, 60 h and 72 h immersion in SBF solution at 37 0.5°C. The reason for measuring EIS spectra at relatively long-term immersion periods is to achieve steady state condition [1]. For each system, three replicates were performed in order to check possible outlayers (none were detected as judged based on fitted EIS values by Grubbs statistical test [2]). One out of three replicates for each system is presented.

The shape of Nyquist plots shows in the high frequency region a capacitive loop and in the low frequency region a typical inductive behaviour. Based on that and with the reference to previous reports, [49 50] fitting of the EIS data was performed using the $R_s(R_1Q_1)(R_2Q_2L)$ model in Figure 4.9. Various other possible models were also employed, but the goodness of the fitting procedure (^{2}) was significantly worse compared with the value that was obtained when $R_s(R_1Q_1)(R_2Q_2L)$ EEC model was used (EEC stands for Equivalent Electrical Circuit). In this model, R_s stands for solution resistance, R_1 is the resistance of the ion conducting paths in the surface layer, and R_2 is the charge transfer resistance. C_1 and C_2 (calculated from Q_1 and Q_2 and respective R values using equation EQ.Cx) are associated with the surface layer capacitance (C_1) and with the double layer capacitance at the metal/electrolyte interface (C_2), respectively. L represents the inductive behaviour.

$$C_x = (R_x Q_x)_{1/n_x}/R_x \qquad \text{(EQ.Cx)}$$

The impedance of CPE is calculated as

$$\text{(CPE)} = (\;(\quad)\;)^{-1} \qquad \text{(EQ.CPE)}$$

The CPE describes an ideal capacitor for $n = 1$, or the distribution of the dielectric relaxation times in frequency space for $0.5 < n < 1$.

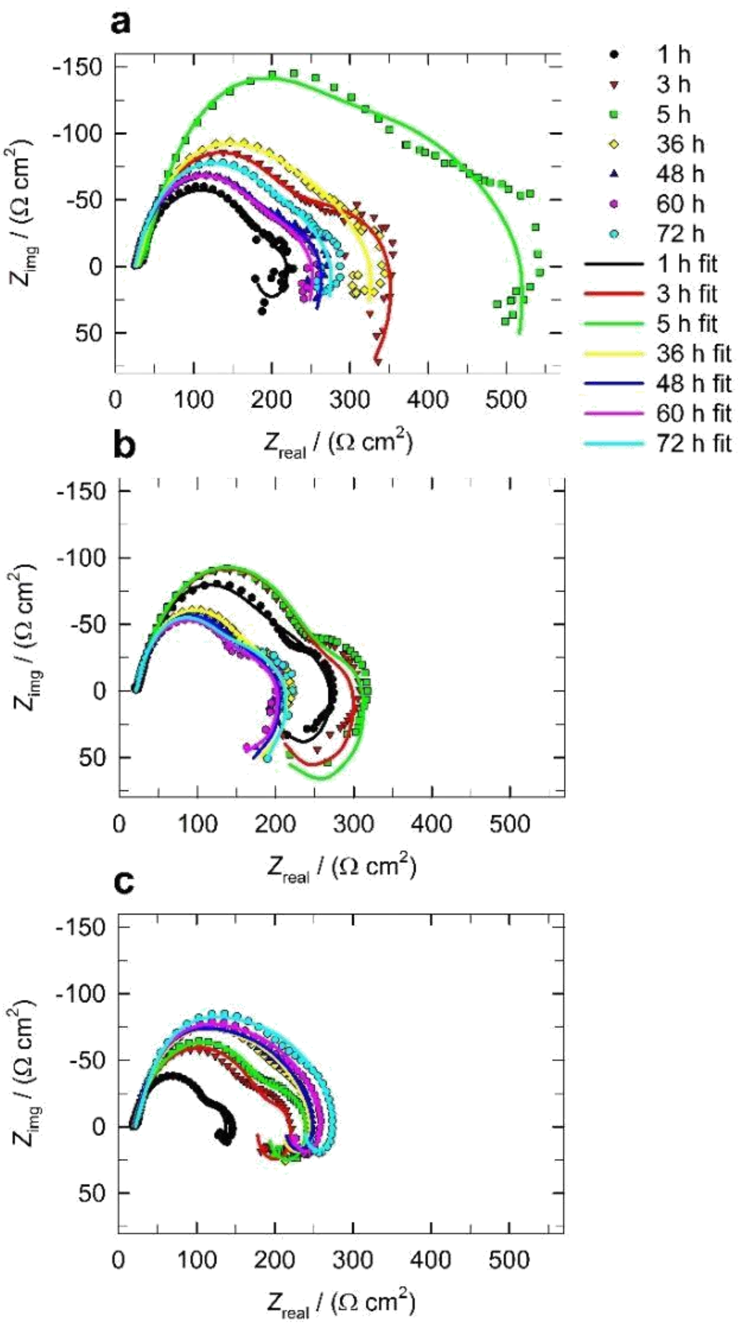

Figure 4.8: Nyquist plots showing measured (dotted symbols) and fitted (solid line) EIS data for a) pure Mg, b) Mg-4Ag, and c) Mg-5Gd measured after 1 h, 3 h, 5 h, 36 h, 48 h, 60 h, and 72 h of immersion in SBF solution at 37 0.5°C.

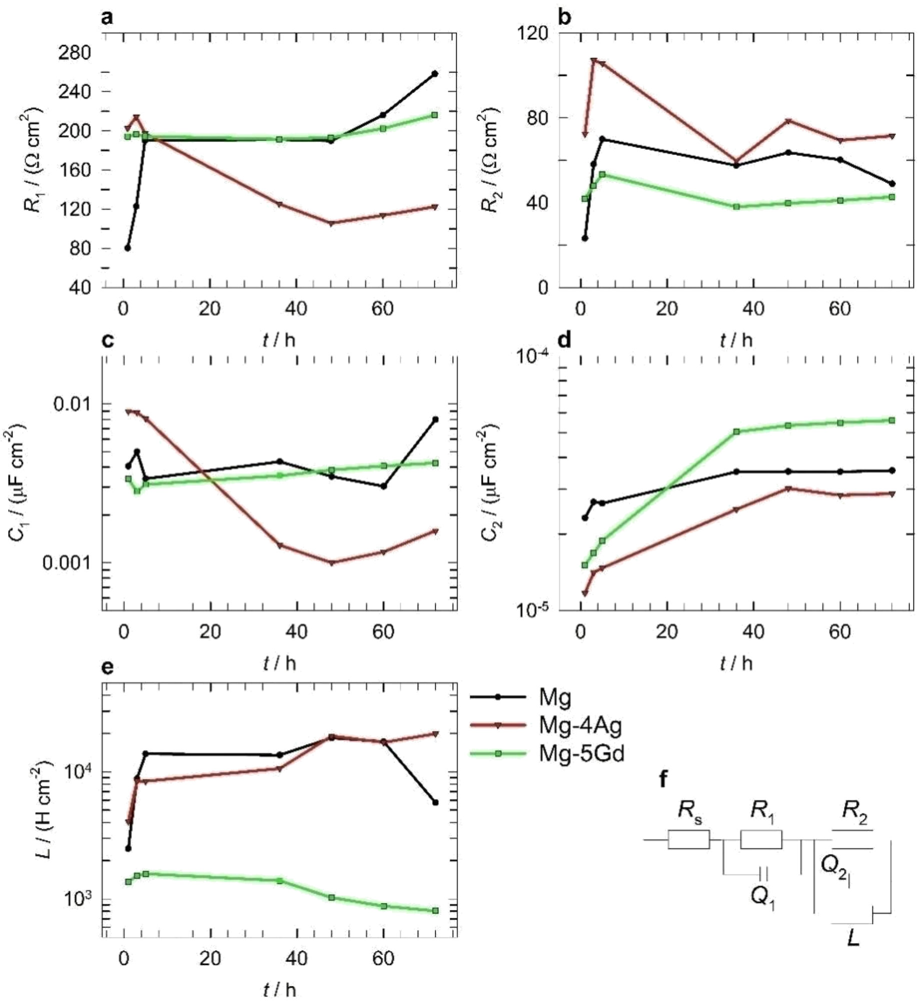

Figure 4.9: Fitted EIS parameters for alloys immersed for 1 h, 3 h, 5 h, 36 h, 48 h, 60 h, and 72 h in SBF at 37 0.5°C, obtained using the $R_s(R_1Q_1)(R_2Q_2L)$ EEC model in Figure f.

Figure 4.9 shows fitted EIS parameters for alloys immersed for different time intervals. The obtained R_1 values representing resistive behaviour of the surface layer composed of oxides and/or hydroxydes are shown in Figure 4.9(a). In general, the R_1 values increase with increasing immersion time for pure Mg and Mg5Gd, whereas the R_1 values decrease with increasing immersion time up to 48 h of immersion (afterwards the R_1 value increase a bit). R_2 values (representing charge transfer resistance) are for an order of magnitude lower compared with R_1 values indicating that the formed surface layer most significantly contributes to the total polarisation resistance (R_p) of the system (R_p is calculated as $R_p = R_1 + R_2$). R_p is a measure of how the metallic material is resisting in transferring the electron to the electroactive species in solution. It has been found that higher the R_p value, lower general corrosion rate is expected. Based on Figures 4.9 (a&b) the highest corrosion resistance can be expected for pure Mg, followed by Mg-5Gd and Mg-4Ag. However, the differences in R_p values for the three systems are not high.

Calculated C_1 values are presented in Figure 4.9(c), and it is seen that for all the three samples the values are changing with increasing immersion time. This relates to the oxide/hydroxide surface layer formation and competitive dissolution process of that layer. On the other hand, C_2 values representing double layer capacitance are in general increases with the increase of immersion time. The increase of double layer capacitance can be explained with the increase of the active surface area (the higher the area of the substrate not covered with surface layer, the higher the capacitance) [4].

Figure 4.9 (e) presents the obtained L values for all three samples immersed in SBF solution. Higher L values are obtained for pure Mg and Mg-4Ag samples compared with Mg-5Gd alloy. The inductive behaviour was previously explained with different surface phenomena. For example, Cao *et al*.
[155] correlated the presence of the inductive loop with localised corrosion or micro-galvanic corrosion occurrence and significant surface film breakdown or galvanic corrosion. Srinivasan *et. al* [157] correlated inductive behaviour with the adsorption of corrosive ions present in the SBF solution. Few investigators have also proposed the above behaviour due to the inductance in a process involving
Mg^{2+}[158,159]. King *et al.*[160] concluded that inductance is associated with the acceleration of anodic dissolution. These observations imply that the inductance process is still not well understood, however, in the research of Mg and its alloys frequently present.

Based on the above results, it may be concluded that for all the systems tested, corrosion is under kinetic-controlled process and inductive behaviour is present. On the other hand, corrosion process does not involve diffusion control (confirmed by the fact that the element describing diffusion did not fit in the most suitable EEC model developed).

4.2.2 Cyclic polarisation measurements

Figure 4.10 shows cyclic polarisation curves for pure Mg, Mg-4Ag, and Mg-5Gd measured after 72 h of immersion in SBF solution at 37 °C. The shapes of all curves indicate active behaviour (minor passive region with expressed breakdown potential E_{bd} is noticed for pure Mg). This behaviour is not present for the Mg-4Ag, and Mg-5Gd alloys. Cyclic polarisation curves for pure Mg and Mg-4Ag shows that the repassivation potential E_{rp} is more positive compared with the open circuit potential E_{oc}, indicating repassivation ability of these two materials (the material can repassivate after the localized corrosion occurrence such as pitting or crevices formation in the forward scan – localize corrosion cease to propagate). On the other hand, E_{rp} is more negative than E_{ocp} for Mg-5Gd indicating that this material does not have repassivation ability [161].

To conclude, the curves in the forward scan for all three systems are at similar current densities confirming that the EIS measurements explained above have no significant difference in general corrosion occurrence between three materials tested is expected.

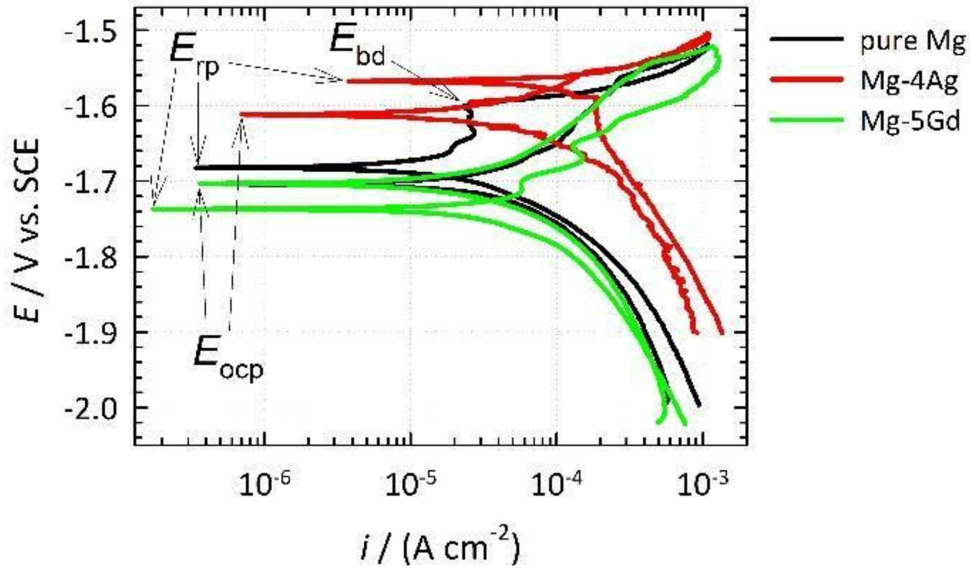

Figure 4.10: Cyclic polarisation measurements for alloys in SBF solution after 72 h at 37 0.5°C.

4.2.3 Summary

General corrosion of the materials tested follow the trend Mg > Mg-5Gd > Mg-4Ag as shown with the EIS measurements, however, the difference between the materials tested is not high. Corrosion of all three materials tested is under kinetic control, but not under diffusion control. Pure Mg and Mg-4Ag have repassivation ability, whereas Mg-5Gd does not possess such property as found based on the cyclic polarisation measurements.

4.3 *In-situ* cross-linked gelatine coating on AZ91 Mg alloy for less-corrosive and surface bioactive orthopaedic application.

4.3.1 Coating characterization

FTIR studies were carried out to confirm the presence of a GEL coating on the Mg alloy surface, its secondary confirmation, as well as to identify the potential mineralization resulting from immersion in SBF media. The FTIR spectra in Figure 4.11 of GEL coated Mg alloy showed a broad absorption band in the region between 3200 - 3100 cm^{-1} is attributed to amide-A stretching within GEL molecule. The signals at about 1645 cm^{-1}, 1539 cm^{-1} and 1236 cm^{-1} were attributed to the amide I, II

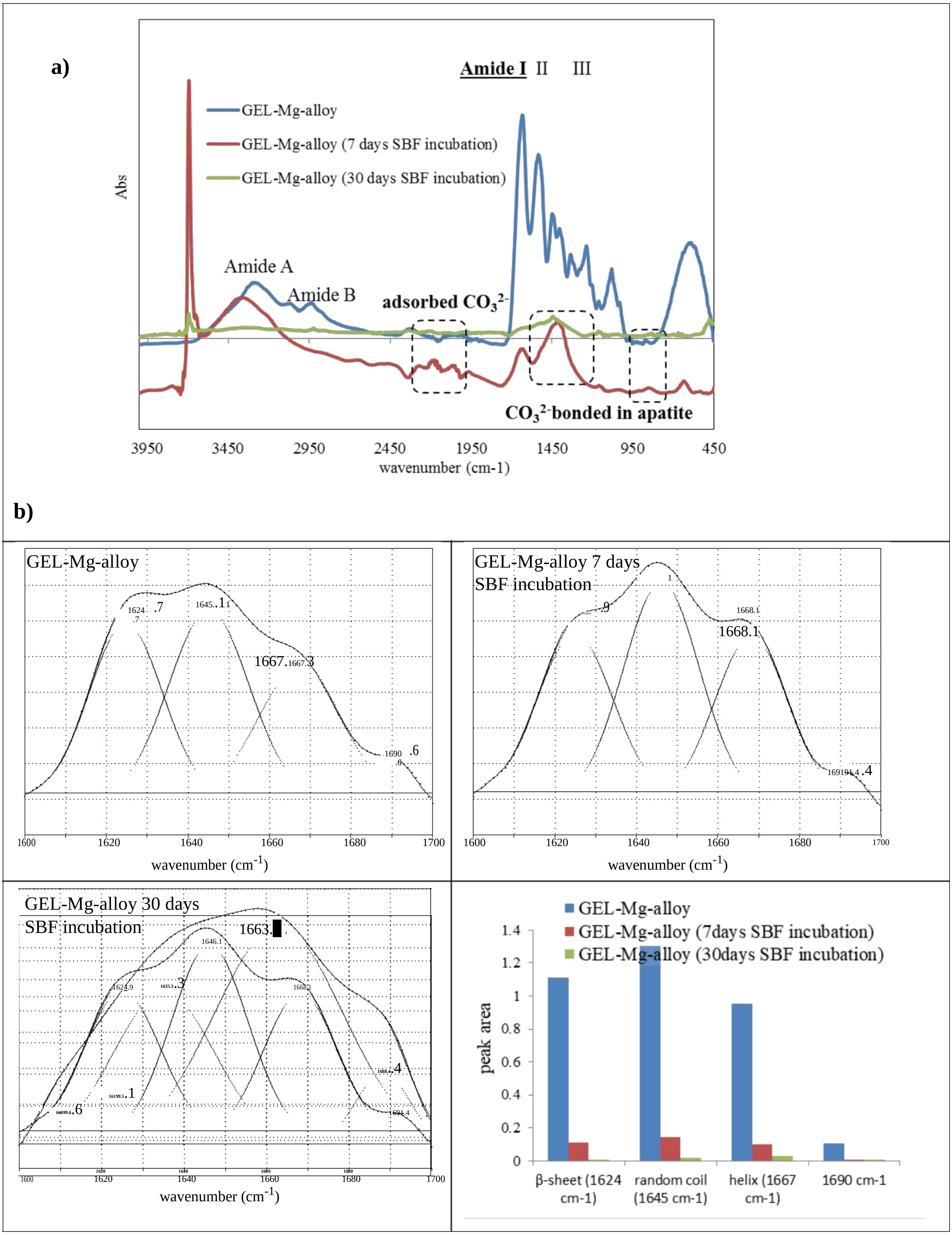

Figure 4.11: a) FTIR absorbance spectra of GEL-coated AZ91 Mg alloy before and after incubation in SBF (pH of 7.4 ±0.2) at 37±0.5 ºC for 7 and 30 days, and b) deconvoluted Amide I (1600-1700cm^{-1}) region of the respective samples with inserted histogram containing deconvolution data

and III groups respectively and all of them showing a typical protein fingerprint. The detailed observation of deconvoluted amide I, as the most useful IR indicator for secondary protein structure, revealed four bands with frequencies centred at around 1624 cm^{-1}, 1645 cm^{-1}, 1667 cm^{-1} and 1690 cm^{-1}, assigned to β-sheet, random coil, polyproline (II-type) helix conformation and intermolecular associations respectively [162]. However, the quantified peak areas (Fig.1b, inserted values) demonstrated the domination of random coil conformation in both cases. Based on our previous study [83], the random coil GEL confirmation was adapted during the casting process, which allowed maximal exposure of the cell recognition amino-acid sequences (i.e., arginine-glycine-aspartates, RGD) and may thus be valuable for primary cell response during biomedical application. Moreover, the 10-fold area reduction for all bands after SBF incubation along with newly appearing carbonate (CO_3^{2-}) related bands (Fig. 1a), indicating the progress of mineralization process. As reported in our previous study [65], the presence of carbonate-related vibration be due to direct adsorption (2000-2300 cm^{-1} region) or may be attributed to apatite presence by being bonded with PO_4^{3-} [163]. However, clear evidence for the presence of PO_4^{3-}vibration (bands at 1049 and 1033 cm^{-1}) has been missing due to its overlapping with GEL spectra, as well as presence of thick carbonate layer [164]. These results would also indicate on the formation of an amorphous, non-stoichiometric type apatite, being already well described [46] as a pre-step-in HAP formation. Only traces of GEL molecules, generally in a helix and random coil conformation, were found on the GEL coated alloy surface after 30 days of incubation; their retention was probably the consequence of extensive inter- and intra-molecular interactions with the Mg surface, as well as amide (CO-NH) cross-linking of GEL provided by EDC/NHS chemistry.It was also ascertained that such a structure should still possess both negative and positive-rich segments under physiological conditions (pH 7.4), where amino groups are protonated and positively charged, whereas carboxylic groups are deprotonated and negatively charged - which remains free after the GEL macromolecule cross-linking and interactions with the Mg alloy surface, and thus be available for interactions with SBF ions.

Apatite formation in SBF solution has been recorded widely as a quick and convenient way to predict bioactivity of biomaterials *in vitro*. Recent literature explains the formation of apatite and the corrosion layers on the AZ91 Mg alloys in the SBF solution [165–167]. Figure 4.12 (i) & (ii) show the FE-SEM images of uncoated and GEL-coated AZ91 alloy surfaces and cross-sections before and after 7 and 30 days of incubation in SBF solution, respectively.

Uncoated AZ91 alloy surface was getting covered with small flower shaped corrosion products after incubation for 7 days (Figure 4.12 (i) c,d) and also a crack was observed on the alloy. In the case of GEL-coated alloy spongy and plate-like structures were identified on the entire surface of the alloy with uniform distribution, which can be favoured by the orientation and conformation of the pre-deposited

40.9 μm thick layer of GEL macromolecules on the alloy surface and their interactions [84]. The formed corrosion products were mainly consisting of Mg, C, O, Cl with small amounts of Ca and P in both uncoated and coated alloys. These corrosion products confirm the presence of oxide layer and the formation of carbonates on the surface which would protect the Mg surface. These results are in good agreement with the FTIR results for the formation of carbonates and oxide layers on the surface and the formed apatite layer helps the bone formation. Mukhametkaliyev *et. al* [167] have also reported similar results for the nanostructured hydroxyapatite coatings on the AZ91 alloy after 7 days of incubation in the SBF solution.

After 30 days of incubation in SBF solution (Figure 4.12 (ii)), several cracks were observed on the surface of the uncoated alloy with white precipitates, while uniformly distributed white and grey corrosion layers observed on the GEL-coated alloy on both the surface and the cross-section-, the formed corrosion products be similar to that of after 7 days. It is worth mentioning that relatively small amount of P, as well as increased amount of Ca were detected in both, GEL- coated, and uncoated samples after 30 days of incubation (Figure 4.12 (ii), EDS figures), compared to 7 days, implying on time-progression of mineralization process. These results demonstrated that the GEL-coating retards the degradation of Mg alloy and forms thick surface layer, which improves the corrosion resistance of the alloy. The calculated corrosion rates were 2.08 and 1.19 mm/year for the uncoated and GEL coated alloys respectively, indicating that the corrosion rate is controlled by the GEL layer.

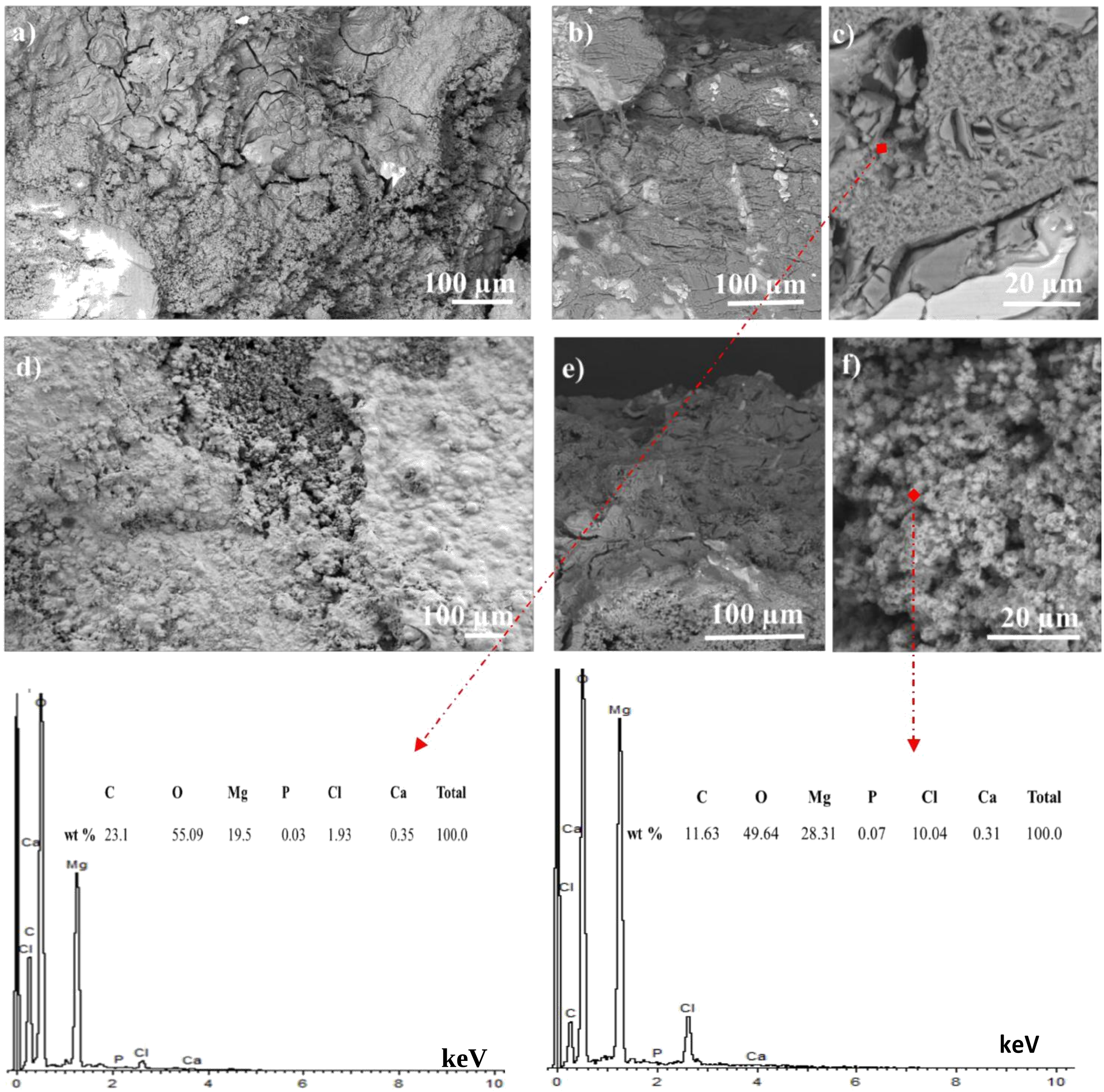

Figure 4.12: (i) FE-SEM images of uncoated AZ91Mg alloy (a) surface and (b) cross-section before incubation; the surfaces of (c,d) uncoated and (e,f) GEL-coated AZ91 alloy after incubation in SBF (pH of 7.4 ±0.2) at 37±0.5 ºC after 7 days. EDS data of selected images shown at the bottom.

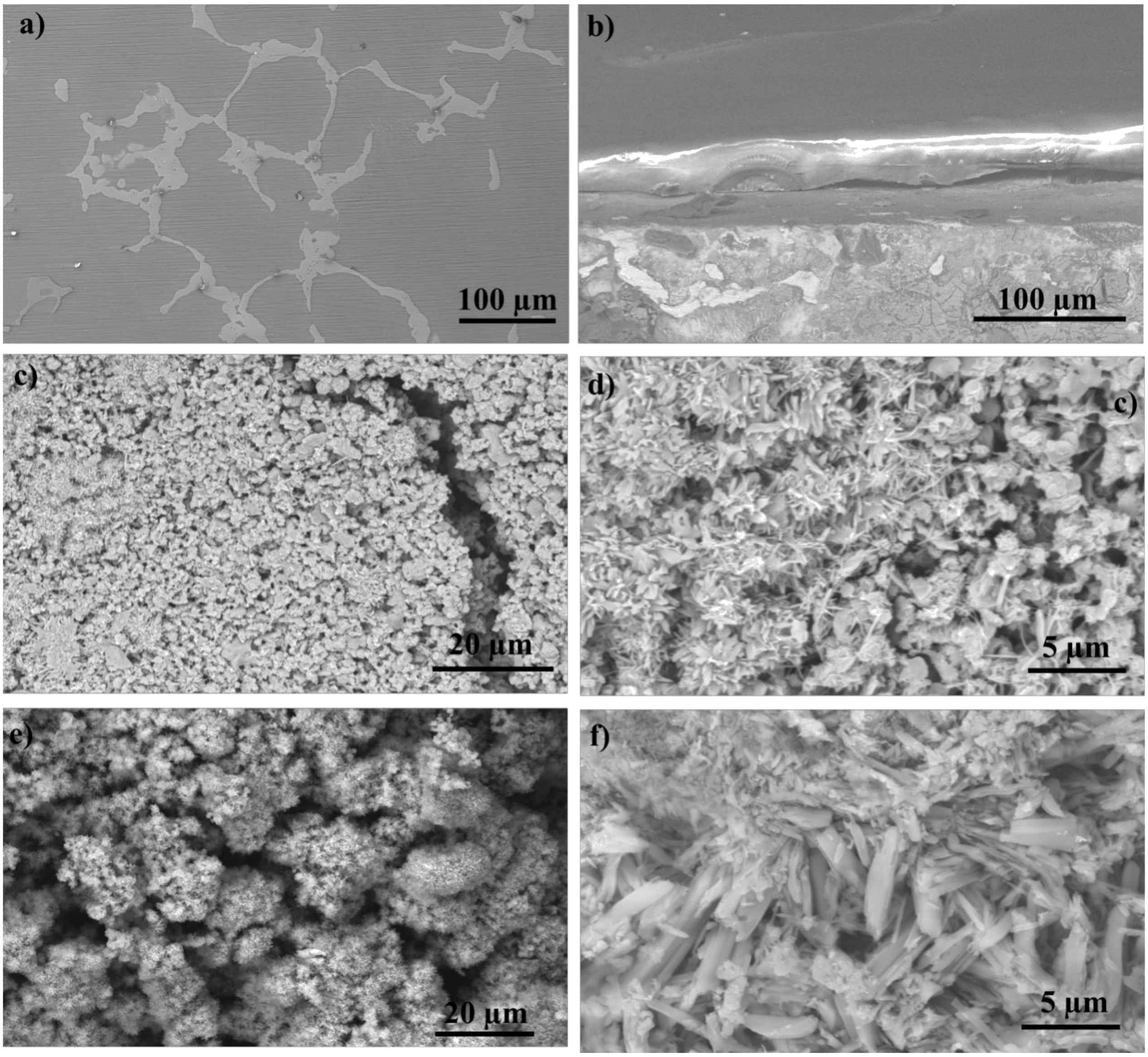

Figure 4.12(ii) : FE-SEM images of uncoated AZ91Mg alloy surface (a) and cross-section (b,c), and GEL-coated AZ91 alloy surface (d) and cross-section (e,f) after incubation in SBF (pH of 7.4 ±0.2) at 37±0.5 ºC after 30 days. EDS data of selected images shown at the bottom..

Figure 4.13 shows the XRD patterns of uncoated and GEL coated alloys before and after incubation for 30 days in SBF solution, confirming the high intensity peaks at 34.4°, 36.6°, 47.8°and 63.4° and 72° corresponding to the structure of magnesium (JCPDS card no. 35-0821). The broad peak around 20° confirmed the presence of GEL [85], and the peaks at 18.5°, 32.5°, 50.5° and 58.5° are corresponding to $Mg(OH)_2$ (JCPDS card no. 044-1482), which confirms the presence of oxide layer on the surface.

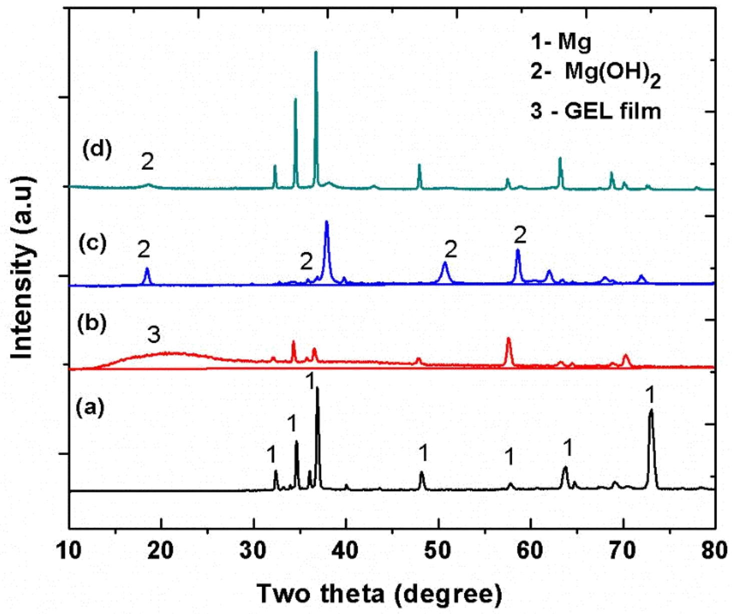

Figure 4.13: XRD patterns of (a) uncoated and (b) GEL-coated AZ91 Mg alloys before incubation, and (c) uncoated and (d) GEL-coated AZ91 Mg alloy after incubation in SBF solution (pH of 7.4 ± 0.2) at 37 ± 0.5 ºC for 30 days.

The variations in pH-values at different immersion times are presented in Figure 4.14 (a). The uncoated alloy showed much higher pH values during the whole time of incubation compared to the GEL-coated alloy. Furthermore, the pH values of the solution for uncoated and coated alloys increased with different slopes with increasing immersion duration. After 30 days of immersion, uncoated sample reached the value of about pH 10, while that of GEL-coated alloy was about pH 8.3, indicating kinetically faster degradation rate of uncoated Mg alloy. During the immersion, Mg has dissolved and combined with OH^- leading to the formation of $Mg(OH)_2$, which was confirmed by the FTIR and XRD studies. In the case of the GEL-coated sample, the GEL layer suppressed the dissolution of Mg and accelerated the formation of thick oxide layer in the SBF solution.

4.3.2 Electrochemical corrosion behavior

The potentiodynamic polarization curves in the Figure 4.14 (b),acquired for the uncoated and GEL-coated Mg alloys revealed that the uncoated alloy had a fairly negative corrosion potential (E_{corr}) in SBF of about -1.53 V, which was shifted to about -1.50 V for the GEL-coated alloy. It can also be seen that, the corrosion current density (i_{corr}) of the coated alloy was lower than that of the uncoated one, indicating a reduction of corrosion rate for the GEL-coated alloy. For all the tested electrodes, the active dissolution parameters E_{corr}, and i_{corr} values are shown in Table 4.2 has confirmed this.

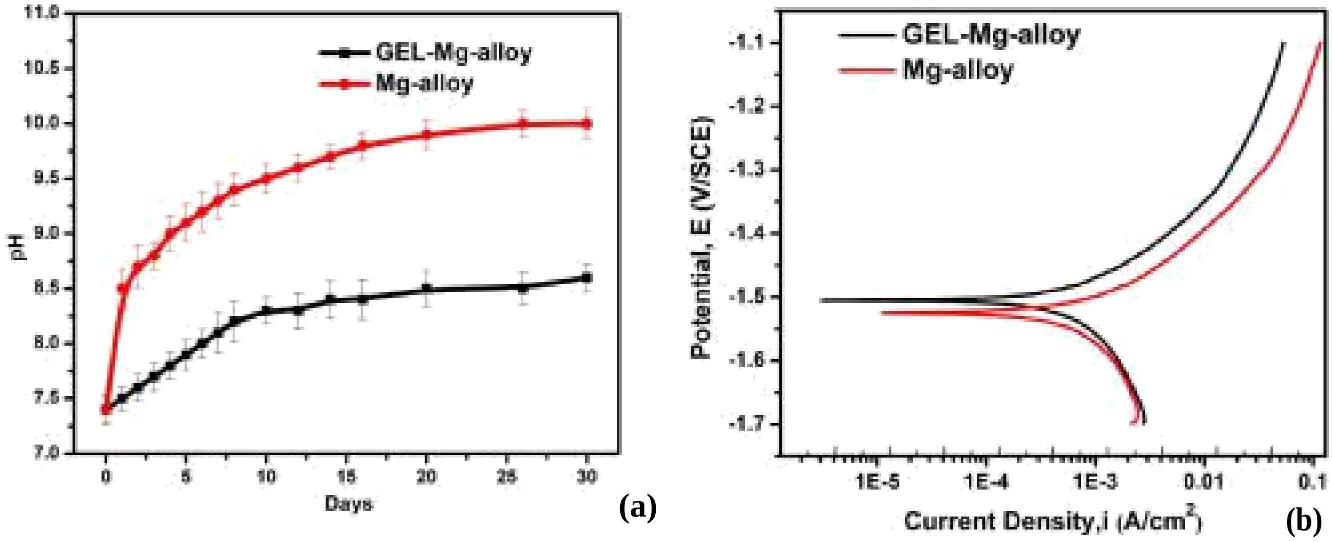

Figure 4.14: (a) Change in pH values of SBF solution with immersed uncoated and GEL-coated AZ91 Mg alloys at 37±0.5 ºC (b) Potentiodynamic polarization curves of uncoated and GEL-coated AZ91 Mg alloy tested in SBF (pH of 7.4±0.2) at 37±0.5 ºC.

Table 4.2: a) Electrochemical parameters of uncoated and GEL-coated AZ91 Mg alloy.

Sample	**i_{corr} (mA/cm^2)**	**E_{corr} (V)**
Uncoated AZ91 Mg alloy	1.05	-1.53
GEL-coated AZ91 Mg alloy	0.79	-1.50

EIS studies were carried out for the uncoated and GEL-coated AZ91 Mg alloys as a function of immersion time in SBF solution to extract more information on their electrochemical corrosion behaviour. Figure 4.15 represents the EIS Nyquist and Bode plots of uncoated in the Figure 4.15 (a,b) and GEL-coated in the Figure 4.15 (c,d) of AZ91 Mg alloys up to 24 h. It has been observed that the Nyquist plots of uncoated alloy consisted of a capacitive loop along with an inductive loop at low-frequency region. Interestingly GEL coated alloy consisted of two capacitive loops and an inductive loop. The high-frequency loop is attributed to the charge transfer between the coating/electrolyte interfaces. The capacitive loop appeared at the middle frequency region is attributed to charge transfer process at coating/substrate and substrate/electrolyte interface of coated and uncoated alloy respectively. The middle frequency loop diameter of the GEL-coated Mg alloy is relatively higher

Table 4.2: b) Comparison of corrosion currents of AZ91 alloy from literature

Alloy	Solution	***E*corr** (V vs.SCE)	***i*corr** (μA cm^{-2})
AZ91	Blood plasma	-1.53	
AZ91	NaCl	-1.518	
AZ91	NaCl+K_2HPO_4	-1.774	
AZ91	NaCl+K_2HPO_4+ $NaHCO_3$	-1.789	
AZ91	SBF	-1.836	3.75
AZ91	m-SBF	-1.713	65.7
AZ91D	Hank solution	-1.36	297
AZ91D	Hank solution	-1.528	22.56
AZ91E	Hank solution	-1.593	4.927
AZ91D	SBF(In the present study)	-1.53	1.03

(Figure 4.15 (c)) than that of the uncoated Mg alloy Figure 4.15 (a)indicating that the deposited GEL layer protected the underneath metal from the corrosion.

The appearance of an inductive loop at the low-frequency region can be attributed mainly to the adsorption of aggressive ions and severe localized attack of magnesium substrate [160,168]. Further, it can be seen from the figures that the diameter of the capacitive loop increased as the immersion duration was increased for uncoated, as well as GEL-coated Mg alloy, indicating that the corrosion product formed on the surface in the SBF solution improved their corrosion resistance. In particular, the diameter of the capacitive loop was relatively high for the GEL-coated alloy compared with that of the uncoated alloy, which confirmed the effectiveness of the GEL coatings. The precipitation of carbonated calcium phosphate compounds and oxide layers Figure 4.12 (i) &(ii) onto the alloy surface could be the reason for the improved corrosion resistance.

Bode plots (Phase angle vs. Frequency and IZI vs. Frequency) of uncoated and GEL coated AZ91 Mg alloys in SBF solution with varying exposure times have been represented in Figure 4.15 (b & d) respectively. The phase angle maxima at 10^2 Hz slightly decrease as the exposure duration is

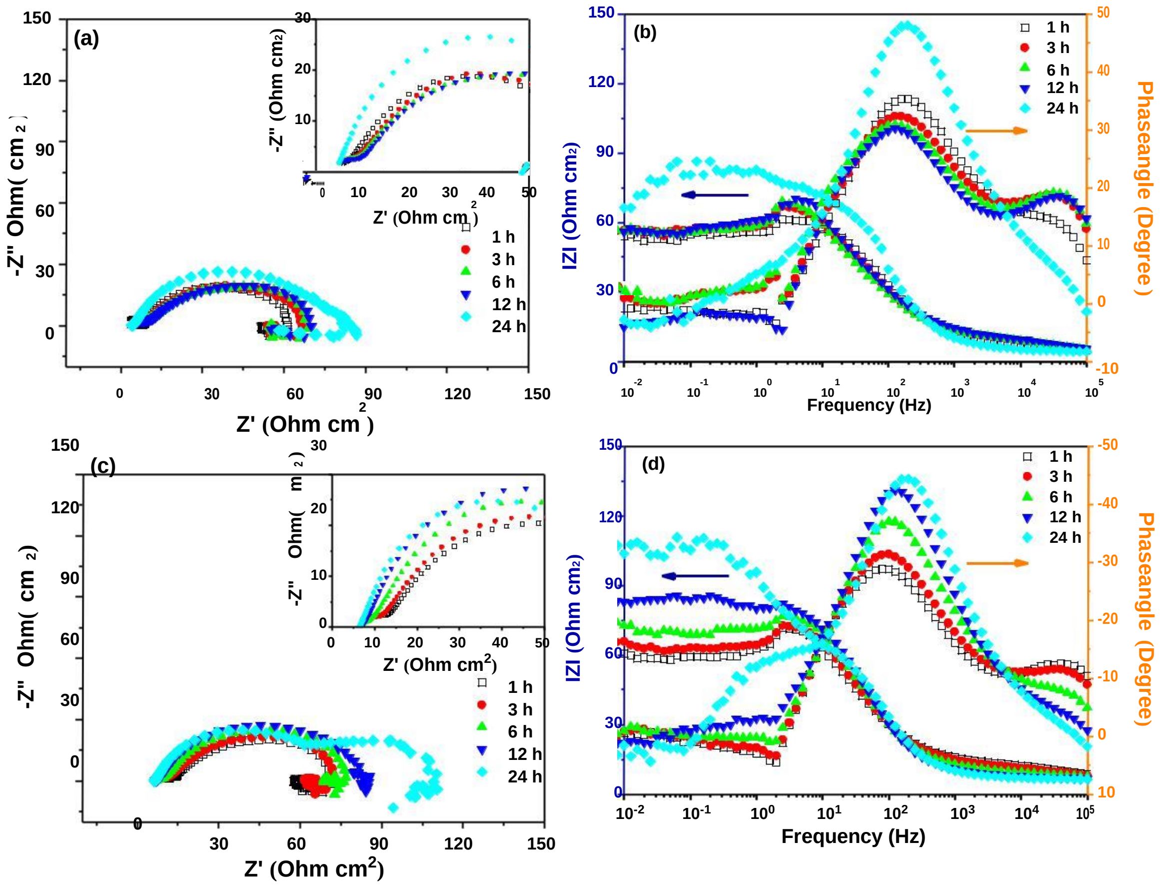

Figure 4.15: Nyquist and Bode plots of (a, b) uncoated and (c, d) GEL-coated Mg alloys as a function of time in SBF (pH of 7.4±0.2) at 37±0.5 ºC.

increased and up to 12 h, further it increases for 24 h. Interestingly in the case of GEL coated alloy, the phase angle maxima were increasing as the exposure duration was increased, which confirms that the capacitive behaviour of GEL coated alloy. Furthermore, increase in phase angle maxima is attributed to passivation of the alloy in SBF solution. A decrease in phase angle maxima in both uncoated and coated alloys are attributed to the adsorption of corrosive ions and further dissolution of Mg. It can be seen from the impedance magnitude at low frequency of bode plots that, the IZI value increases as the exposure duration is increased confirming the barrier behaviour of GEL coatings. However, a significant increase in IZI was not noticed up to 12 h for uncoated alloy and a marginal increase was noticed at 24 h, confirming that the corrosion product formed on the surface is not effective to control the corrosive ion penetration as in the case of GEL coated alloy.

Further, curve fitting analysis was performed with the obtained EIS results and the Equivalent Circuits (EC) are given in the Figure 4.16 The fitting parameters are summarized in Table 3 and also given in Figure 4.17(a-d).The experimental and fitted plots are given in Figure 4.18 , which shows that the fitted values are in well agreement with that of experimental results. EC consisted mainly of two-time constants along with the inductive behaviour for the coated alloy in the Figure 4.16 (b) and uncoated alloy consisted of single time constant with an inductive behaviour in the Figure 4.16 (a)[169,170].

It can be seen from Figure 4.16 that the R_1 value of the GEL-coated Mg alloy is attributed to the presence of GEL coating. In addition to that, the GEL-coated alloy exhibited higher R_1 after 24 h of incubation due to the formation of the corrosion product layer consisting mainly of calcium phosphate compounds. R_1 and CPE_1 provided information about the barrier properties of the GEL layer. As can be seen from Figure 4.17 (C) ,the R_1 value increased, and CPE_1 value decreased as the immersion duration was increased, which indicates that the barrier property of the GEL coating [171]. The precipitation of calcium phosphate compounds also contributed to the improved corrosion resistance. The R_2 and CPE_2 depict the charge transfer process at the interface layer. A gradual increase in R_2 value was noticed for the uncoated and GEL-coated alloy, indicating the higher charge transfer resistance. CPE_2 values were also consistent with the R_2 values. The R_L and L values can be attributed to the inductive behaviour of the uncoated and GEL-coated alloys. In the case of the uncoated alloy, the increase in R_L and L values was noticed up to 6 h, and further a decreasing trend was noticed, which was attributed to the degradation of the Mg. However, the GEL-coated alloy exhibited an opposite trend in R_L and L values confirming the extended corrosion protection of GEL coating in SBF solution.

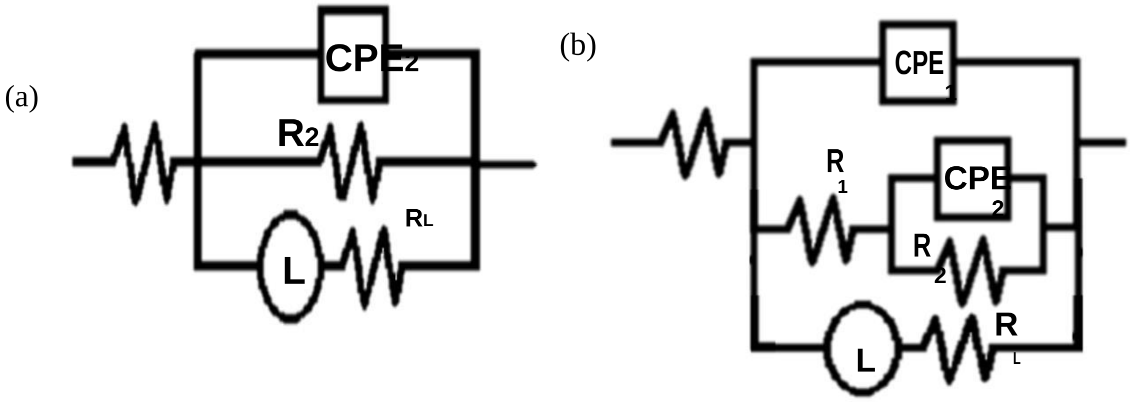

Figure 4.16 : Equivalent circuit used for curve fitting of obtained EIS results {R_s - solution resistance, R_1 - electrolytic diffusion resistance, and R_2 - charge transfer resistance CPE_1, CPE_2 - Constant phase elements (CPE) of the newly formed layer and double layer capacitance respectively; R_L - inductive resistance and L – inductance}.

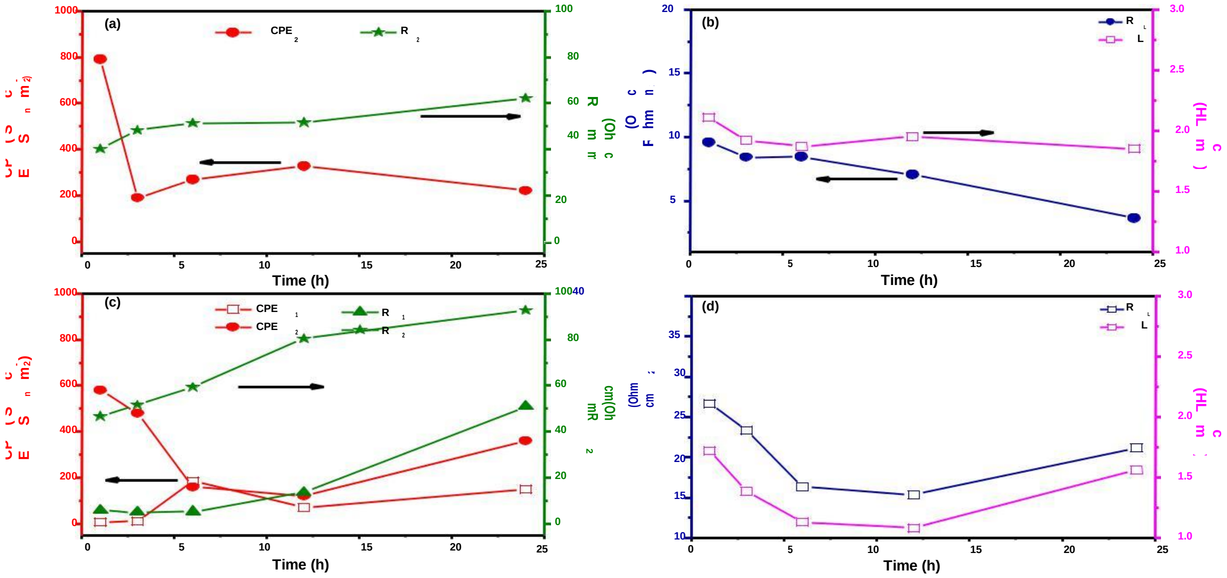

Figure 4.17:EC parameters of (a, b) uncoated and (c, d) GEL-coated Mg alloy in SBF (pH of 7.4±0.2) at 37±0.5 ºC and different time intervals.

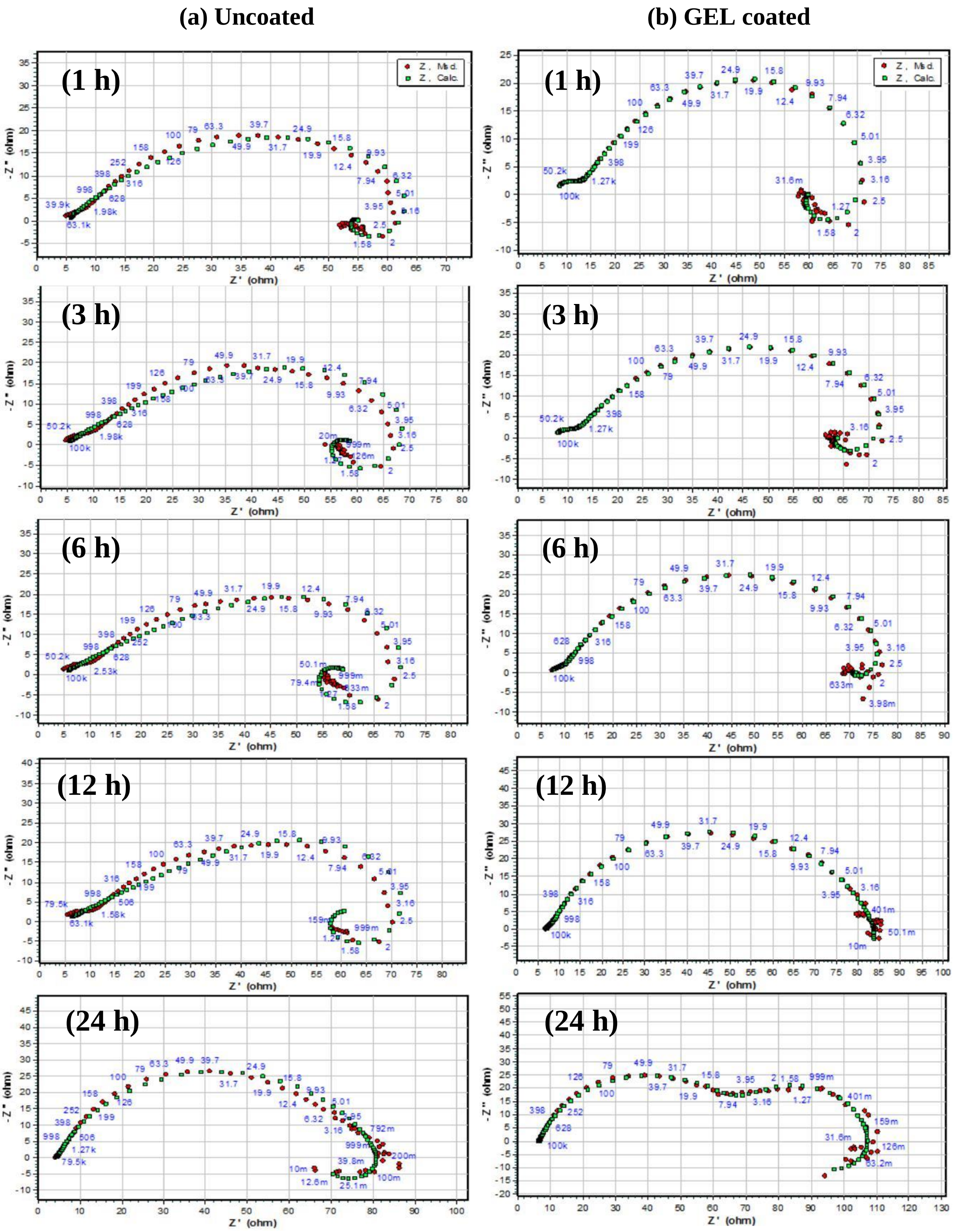

Figure 4.18: Equivalent Circuit (EC) fitted EIS curves as a function of immersion time (1, 3, 6, 12 and 24h) for uncoated and GEL-coated Mg alloys in SBF (pH of 7.4±0.2) at 37±0.5 ºC.

Table 4.3: Equivalent circuit parameters of uncoated and Gel coated AZ91 alloys

Sample	Time (h)	R_s (Ω cm^2)	CPE1 (μS s cm^{-2})	n_1	R_1 (Ω cm^2)	CPE2 (μS s cm^{-2})	n_2	R_2 (Ω cm^2)	R_L (Ω cm^2)	L (H cm^{-2})	Error (χ^2)
Uncoated AZ91 D	1	5.25	-	-	-	790.0	0.572	40.3	9.59	2.11	0.0035
	3	4.42	-	-	-	189.8	0.438	48.2	8.42	1.92	0.0053
	6	4.32	-	-	-	269.3	0.399	51.4	8.45	1.87	0.0055
	12	4.80	-	-	-	327.8	0.381	51.6	7.05	1.95	0.0061
	24	4.49	-	-	-	221.1	0.764	62.2	3.64	1.85	0.0021
GEL Coated AZ91 D	1	7.48	7.37	0.823	5.75	580.4	0.662	46.6	26.6	1.72	0.0004
	3	7.23	10.0	0.817	4.98	485.7	0.678	51.6	23.3	1.38	0.0005
	6	6.76	185.9	0.633	5.23	164.4	0.781	59.3	16.3	1.13	0.0005
	12	6.82	70.7	0.807	13.5	125.4	0.803	80.4	15.3	1.08	0.0002
	24	6.63	154.1	0.808	50.9	362.8	0.985	92.8	21.2	1.56	0.0001

4.3.4 Summary

In-situ cross-linking of gelatine (GEL) coating by carbodiimide chemistry was successfully applied on the surface of the AZ91 Mg alloy by a dip coating technique. The presence of GEL was confirmed by the FTIR spectroscopy and SEM imaging, resulted to a coating morphology with complete and uniform surface coverage and the formation of spongy-flower like carbonate containing mineral structures after 30 days of immersion in simulated body fluid. Moreover, an extended (from 2.08 to 1.19 mm/year) corrosion protection of GEL-coated AZ91 Mg alloy in SBF solution was confirmed by electrochemical studies, which may provide a bio-safer pH environment (pH 8.3) during potential *in vivo* application. Therefore, the proposed cross-linked, GEL-based coating can be an alternative for neat Mg alloys, offering improved degradation behaviour in orthopaedic applications; however, further studies are required to improve the mechanical stability and the long-term corrosion protection ability of such a coating.

4.4 Electrochemical studies of electrospun coated cellulose acetate (CA) on magnesium surface

4.4.1 Electrochemical Impedance studies:

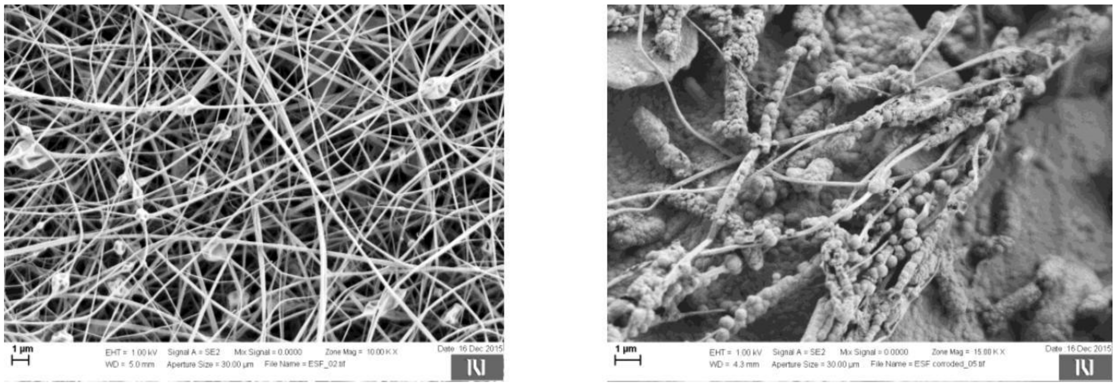

(a) **(b)**

Figure 4.19: FE-SEM images of Mg alloy surface coated with CA nanofibers a)before and b) after the electrochemical testing in SBF at 37°C for 24 h.

Figure 4.19 shows the electrospun coated CA SEM micrographs. Fiber diameter is observed from 250-400nm Figure 4.20 compares the Nyquist and Bode plots of uncoated Figure 4.20 (a & b) and CA coated Figure 4.20 (c & d) pure Mg as a function of immersion time in SBF solution. It is observed from these figures that the corrosion behavior is different between the uncoated and coated pure Mg. Two capacitive loops along with an inductive loop was appeared for the uncoated pure Mg in the studied frequency range. Furthermore, the diameter of the capacitive loops significantly varied as the immersion duration was varied in SBF solution. The capacitive loop diameter increased as the immersion duration was increased up to 12 h and decreased for 24 h. In addition to that, a marginal increase was noticed for 48 and 72 h. interestingly similar trend was noticed in the case of coated pure Mg as well. However, the diameter of the capacitive loop drastically increased indicating that, coating significantly improves the corrosion resistance. The high and low frequency capacitive loops could be attributed to electrolyte/surface layer and surface layer/ substrate respectively for the uncoated pure Mg. In the case of coated pure Mg, CA coating act as surface layer. Furthermore, the capacity loop diameter significantly increased compared to uncoated sample confirming the influence of CA coating on the control of electrolyte diffusion to the substrate. The inductive loop was well distinguished for uncoated pure Mg, whereas the inductive loop was not observed for CA coated pure Mg till 48 h and the loop was appeared at 72 h indicating that, the CA effectively resist the electrolyte penetrationand control the corrosion rate. The inductive loop could be attributed to adsorption of aggressive ions and resulting corrosion product formation on the surface.

EIS Bode plots as a function of immersion time in SBF solution at 37 ± 0.5 ºC for uncoated and CA coated pure Mg are shown in Figure 4.20 (b and d) respectively. The phase angle maxima appeared for the uncoated pure Mg in the frequency range 10^3 to 10^1 indicating the capacitive behavior of surface layer. Phase angle value decreased further when the frequency approaches 10^{-2} Hz, indicating the degradation of surface layer. Interestingly, in the case of CA coated pure Mg, the phase angle value was higher (10^3 to 10^{-2} Hz) and decline in the phase angle was noticed up to 12 h, indicating the capacitive behavior and increase of corrosion resistance. However, the phase

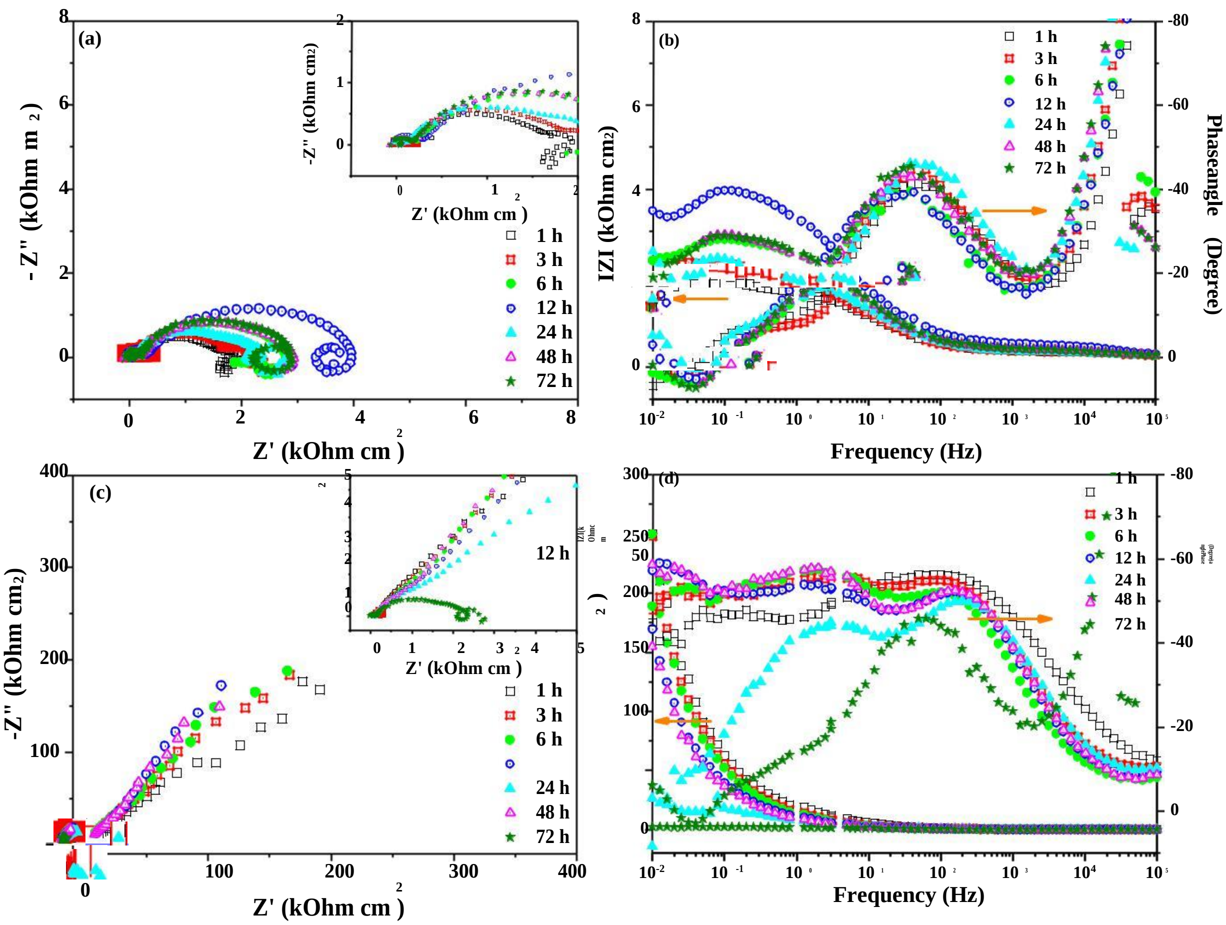

Figure 4.20: EIS Nyquist and Bode plots of (a & b) uncoated and (c & d) CA coated pure Mg as a function of immersion time Mg in SBF solution at 37 ± 5 ºC.

angle decreased for 24 and 72 h indicating the degradation of surface layer and decreases the corrosion resistance. IZI values of CA coated pure Mg was several orders higher than that of uncoated pure Mg.

Figure 4.21 (a & b) shows the equivalent circuit (EC) model used for curve fitting of EIS results and the obtained EC parameters are summarized in Table 4.4. The error percentage was less (χ^2 ~10^{-3}) which shows that good agreement exists between the experimental result and calculated results Figure 4.22 (a & b).

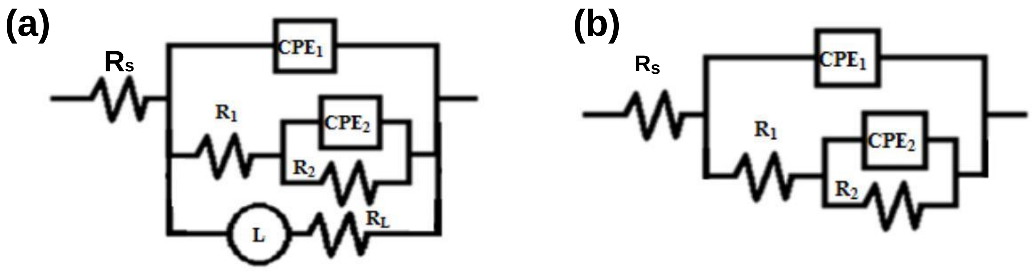

Figure 4.21: Equivalent circuit models (a) Uncoated and CA coated after 72 h and (b) CA coated (R_s - solution resistance, R_1 - electrolytic diffusion resistance, and R_2 - charge transfer resistance; CPE_1 & CPE_2 - Constant Phase Elements (CPE) of the newly formed layer and double layer capacitance respectively; R_L - inductive resistance and L - inductance) used for curve fitting of EIS results.

It can be seen from the results that, CPE_1 decreased (43.8 to 2.96 µS s^n cm^{-2}**)** and R_1 values increased (0.189 to 0.302 kΩ cm^2) up to 12 h. Then the CPE_1 values increased for 24 and 72 h indicating the poor corrosion resistance of uncoated pure Mg. Similar trend was also noticed for CA coated pure Mg, however, a significant increase in R_1 values were noticed indicating that, CA coating increases the corrosion resistance in SBF solution. Interestingly the charge transfer resistance (R_2) values were several orders higher than that of uncoated pure Mg confirming better corrosion resistance extended by CA coating. R_2 value was increased for about 2000 and 960 times higher after 1 and 12 h of immersion in SBF solution for CA coated pure Mg compared to uncoated pure Mg. Similarly, CPE_2 values also decreased after 12 h further confirming the capacitive behavior of the coating. In addition to that the corrosion products mainly consisting of carbonated Calcium (Ca) and Phosphate (PO_4^{3-}) compounds could be responsible for the decrease of corrosion resistance as the immersion duration is increased. These results clearly indicate that, the CA coatings significantly improve the charge transfer resistance values by forming a stable surface layer.

Table 4.4: Equivalent circuit curve fitting parameters of EIS results as a function of time.

Immersion duration (h)	CPE_1 ($\mu S\ s^n\ cm^{-2}$)	n_1	R_1 ($k\Omega\ cm^2$)	CPE_2 ($\mu S\ s^n cm^{-2}$)	n_2	R_2 ($k\Omega\ cm^2$)	R_L ($\Omega\ cm^2$)	L ($H\ cm^{-2}$)	Error (χ^2)
	Uncoated								
1	43.8	0.581	0.189	10.8	0.819	0.259	50.6	326.7	0.0055
3	6.79	0.756	0.213	41.2	0.656	0.356	71.7	0.057	0.0027
6	3.82	0.769	0.239	31.4	0.717	2.006	633.0	2503	0.0015
12	2.96	0.632	0.302	29.8	0.672	3.121	781.1	1799	0.0026
24	68.1	0.414	0.296	46.9	0.965	1.944	335.4	1032	0.0042
48	4.04	0.814	0.219	29.8	0.735	2.688	6.952	5.241	0.0075
72	65.9	0.656	0.191	25.2	0.754	2.051	673.6	2114	0.0025
Coated									
1	9.664	0.668	2.688	11.14	0.711	533.03	-	-	0.0020
3	18.75	0.579	3.134	13.65	0.856	2711.0	-	-	0.0008
6	11.02	0.719	3.584	11.42	0.555	2805.0	-	-	0.0021
12	10.05	0.728	3.688	19.47	0.577	2993.0	-	-	0.0025
24	10.96	0.710	3.558	23.01	0.793	17.707	-	-	0.0088
48	9.181	0.771	3.939	13.50	0.601	1498.0	-	-	0.0027
72	8.815	0.785	1.33	40.51	0.701	2.1530	220.70	9.643	

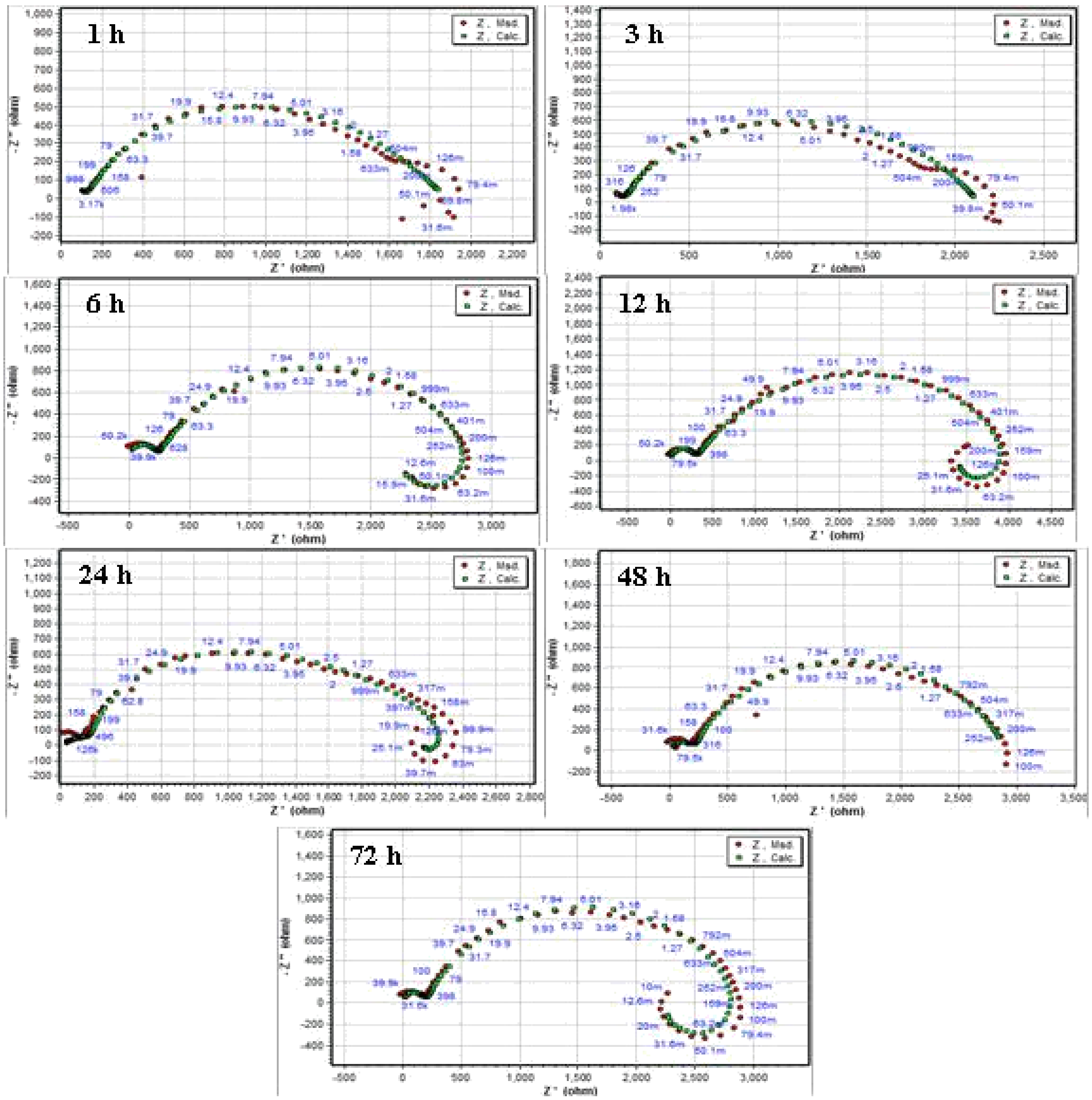

Figure 4.22: (a) Equivalent circuit curve fitting plots of CA coat ed pure Mg as a function of time.

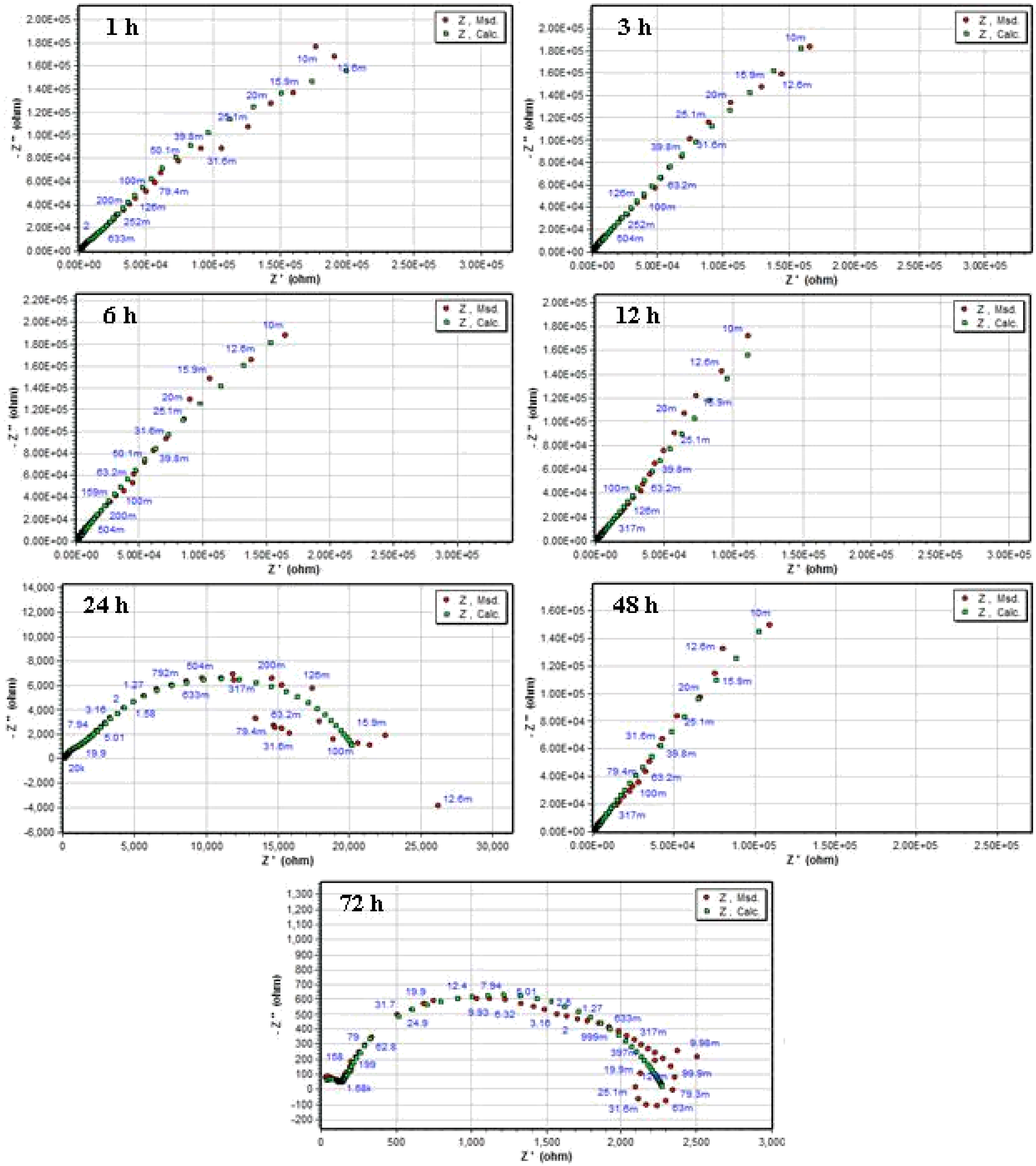

Figure 4.22: (b) Equivalent circuit curve fitting plots of CA coated pure Mg as a function of time.

4.4.2 Cellulose Acetate –Mg Mechanism:

Cellulose Acetate (CA) is acetylated cellulose derivative with degrees of acetylation of around 40-50 %. The rest of the functional groups are –OH and to some extend even –COOH. The zeta potential values at physiological pH have been determined to be between -10 mV and -12 mV.

The acetylation of cellulose makes it more hydrophobic when compared to cellulose. Static contact angles for CA membranes have been determined to be around 80 ° (acetylation degree = 40 %). The hydrophobicity of film coatings play an important role in salt ion transfer. Water represents an ideal environment for salts like NaCl to dissociate, due to its dipole nature. The dissociated ions get hydrated by water molecules and as such diffuse through swollen polymer films. Thus, polymers with a high hydrophilic nature will absorb lot of water, get swollen and increase the amount of transported NaCl through the films. The hydrophobic CA films absorb little amounts of water and therefore limit the transportation of NaCl through the film coatings (Figure, reaction c). The hydrophobic environment of the polymer is also less favourable for the dissociation of the NaCl which also results in lower ion sorption (Figure, reaction b). The polymer-ion and polymer-water interactions in this case have no influence on the NaCl diffusion. The amount of transported salt ions can therefore be directly correlated with the acetylation degree of the CA, since the latter directly influences the hydrophobic nature of CA.

Furthermore, the –COOH groups of CA dissociate at physiological pH and introduce negative charge to the CA backbone ($-COO^-$). The charge of the polymer has an important influence on the ion sorption. It generally increases the hydrophilicity of the polymer which increases the water sorption capacity. But on the other hand, the charged groups can be neutralised by the oppositely charged salt ions and the salt counter ions will be attracted to lower degree. In the case of CA and NaCl, the dissociated Na+ will be attracted to the negatively bound –COO-groups and the Cl- ions will act as counter ions. The concentration of Cl- in the polymer structure in such scenarios is lower, due to repulsion forces between the Cl- and the –COO-, than in the case of uncharged polymers where ion pairs move through the swollen polymers film in dependence of the amount of water uptaken by the polymer film (Figure, reaction a). This however is only valid for low salt concentrations. At higher concentrations these forces are screened and the polymer will absorb more salt ions. Subsequently, negatively charged CA coatings will reduce the amount of Cl- passing through the film and reacting with the magnesium alloy at low salt concentrations and attract more salt ions at higher salt concentrations. In both cases, this effect is minor in the case of CA, since the amount of –COOH groups is negligible.

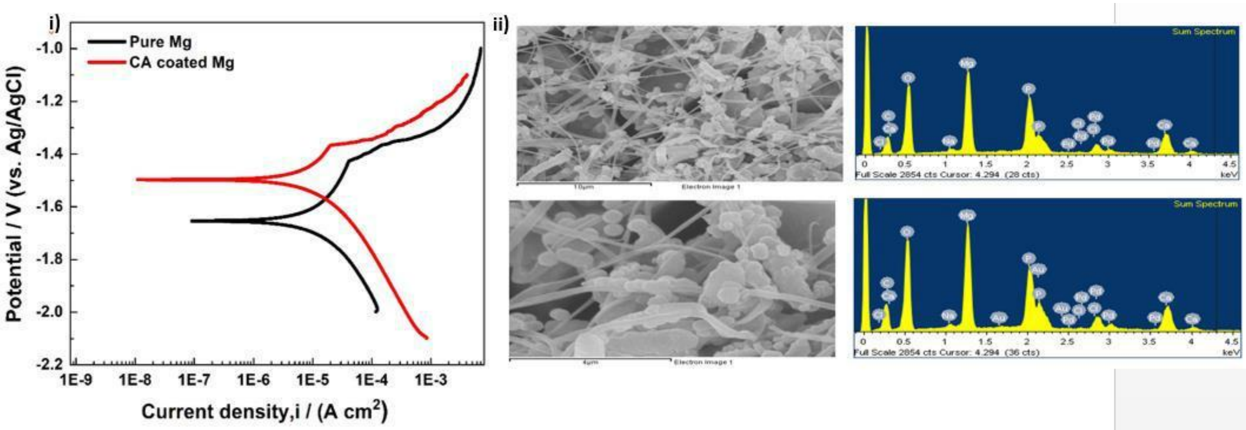

Figure 4.22: c) i) potentiodynamic polarization studies of Pure Mg and CA coated Mg after incubation of SBF solutions at 37±0.5 ºC. ii) EDS analysis of CA coated samples after the corrosion test.

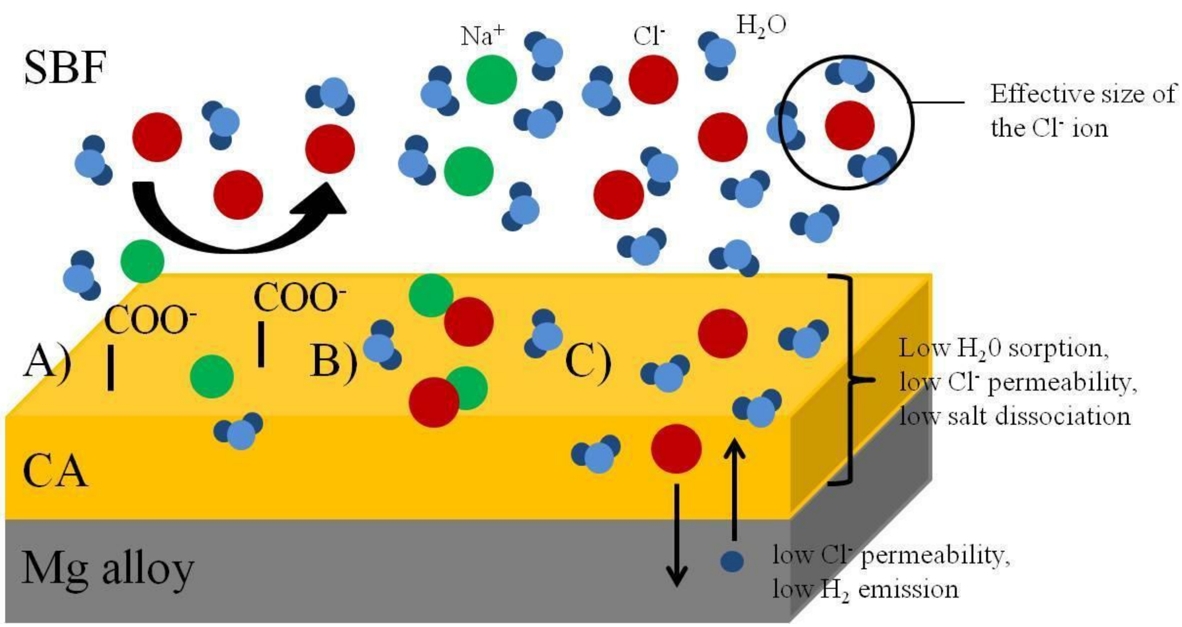

Figure 4.22 : d) Mechanism of CA-coated Mg in SBF solution

.

4.4.3 Potentiodynamic polarization studies:

The potentiodynamic polarization curves for magnesium and CA coated Magnesium sample SBF solution in the potential range from −2.2 V to −0.5 V vs. Ag /AgCl/1.0 M KCl are shown in Figure. 4.22 c i).The corrosion potential (Ecorr) value for pure Mg is found to be -1.65V. The Ecorr value for plasma treated ungrounded alloy is found to be −1.50 V it is shifted towards more negative potential; indicates the better corrosion resistance for CA coated alloy.

Figure 4.2.2 c ii) shows the EDS analysis of the CA coated samples after the corrosion test. EDS analysis shows the presence of Mg, O, Ca, P after incubation in SBF for 24h.The presence of oxygen shows the formation of oxide layer on the surface which protects the surface from corrosion. The presence of Ca and P (1.47) indicates on the formation of hydroxyapatite.

4.4.3 Summary

In the present study, the coated CA nanofibers were characterized by using FE-ScanningElectron Microscopy (FE-SEM). Fiber diameter is observed from 250-400 nm .The SEM observations of the samples indicate white precipitates on the samples. EDS analysis shows the presence of Mg, O, Ca, P. The presence of Ca and P and O indicates the formation of hydroxyapatite. Nano fibrous sample shows better corrosion resistance when compared to pure magnesium.

4.5 The chitosan coating and processing effect on physiological corrosion behaviour of porous magnesium monoliths

4.5.1 Monoliths processing and microstructure characterization

Figure 4.23 SEM micrographs of upper surfaces of porous Mg monoliths after heat treatment (I) and (II). Porosities within the monoliths obtained by partial evaporation of ammonium bicarbonate were mostly open type pores, which depends on the type of original powders used. The pore space structure after space holder removal displays irregular shaped macro pores inside the sintered material. According to SEM images, two types of pores were observed after sintering, the first type with a diameter up to 100 µm and the second type pores with diameters range between 150-500 µm (indicated by arrows in Figure 4.23 (f)). Observations indicated that the porosity increased from 14% via 30% to 40% with increasing the ammonium bicarbonate content.

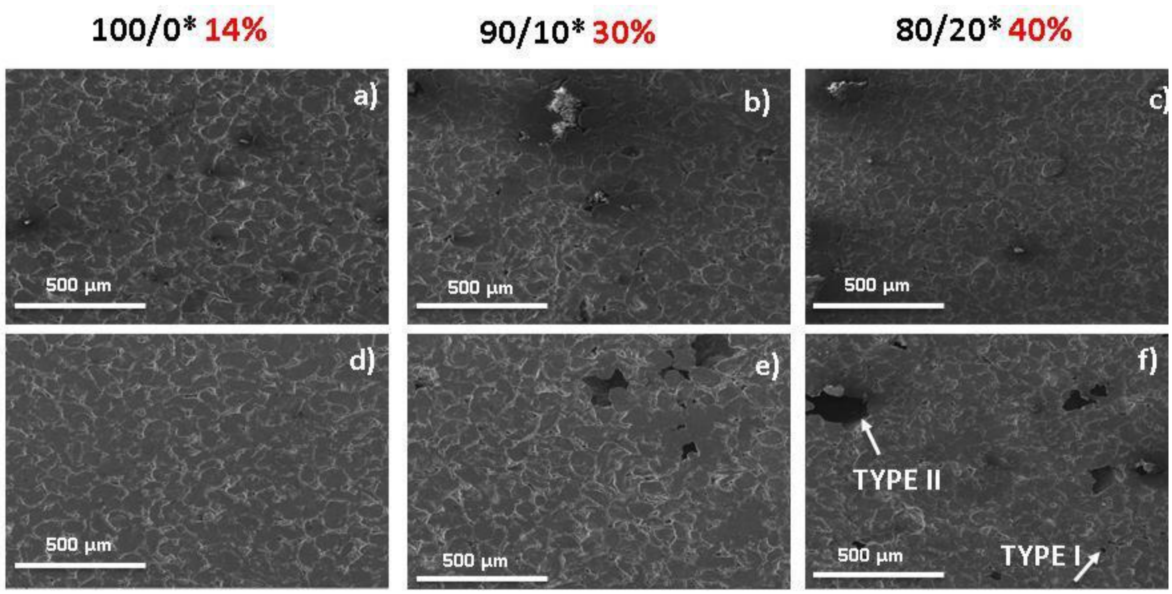

Figure 4.23: SEM images of Mg monolith surfaces after first (at 130°C; a, b and c) and second (at 550°C; d, e and f) heat treatment, corresponding to different Mg/NH4HCO3 ratio* (100/0, 90/10 and 80/20).

4.5.2 Coating identification and evaluation of monoliths stability

A film-forming properties of chitosan [173] were utilized to advance the Mg monolith coating process, results in good surface coverage. Its presence was confirmed by inspected FTIR spectral lines (Figure 4.24), where typical chitosan-related spectral bands were identified within chitosan-coated Mg monolith: the broad absorption line in the region between 3200-3500 cm^{-1} attributed to -OH and -NH stretching, signals at about 1632 cm^{-1}, 1555 cm^{-1} and 1380 cm^{-1}

attributed to the amide I, II, and III modes of the residual N-acetyl groups, respectively, as well as band at about 1150 cm^{-1} being related to the anti-symmetric stretching of C-O-C bridge and at about 1080 cm^{-1} to skeletal vibration involving the C-O stretching [174]. The small (3-8 cm^{-1}) shifting in bands position within OH-related region in case of chitosan-coated Mg monoliths from those in neat chitosan indicated on possible hydrogen bonding with $Mg(OH)_2$ or MgO segments, being present on monolith surface, as will be discussed later within XRD data evaluation.

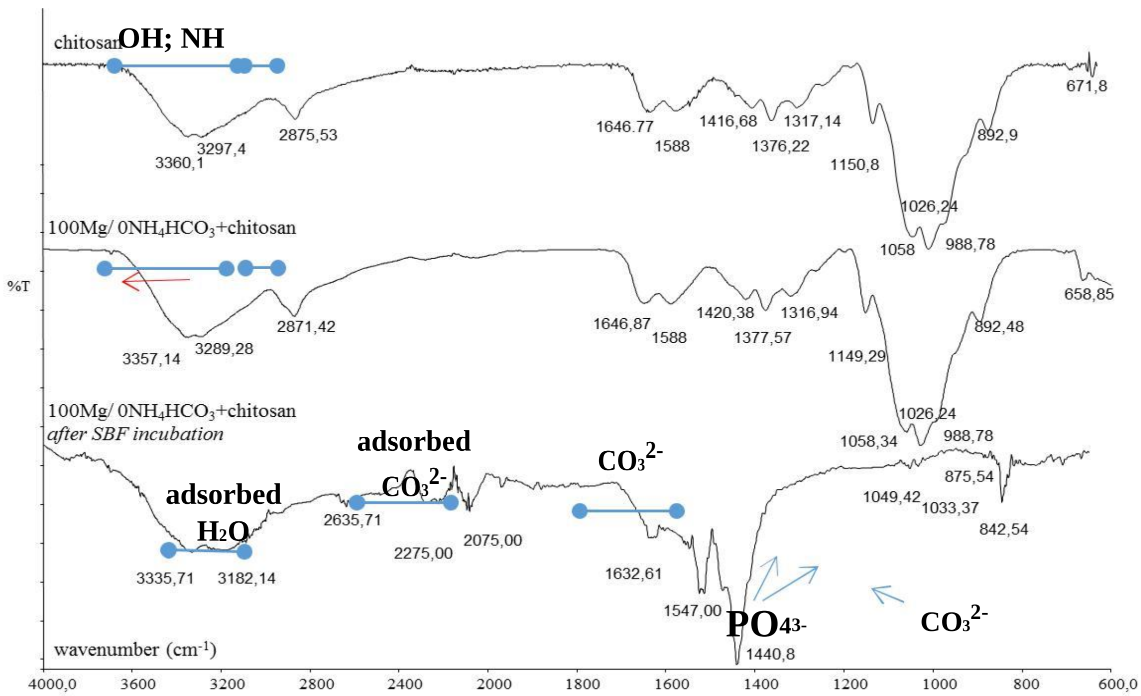

Figure 4.24: ATR-FTIR spectra of chitosan and chitosan-coated Mg monoliths prepared with the lowest (14%) porosity, before and after 48h incubation in SBF solution at 37°C.

According to the anticipated Mg-chitosan interaction Figure 4.25(a), the presence of chitosan layer is expected to improve the physiological stability of the monolith, affecting both the complex degradation/corrosion process and simultaneous mineralization potential by means of SBF ions deposition Figure 4.25(b). Indeed, the process of bio-corrosion occurred *in vivo* after Mg alloy implantation was approved [175] to proceed through simultaneous and complex mechanisms composed of $Mg(OH)_2$ formation (due to Mg dissolution and surface alkalization), further exchange with soluble $MgCl_2$ (which readily progress the degradation process), Ca^{2+} and PO_4^{3-}deposition on non-dissolved $Mg(OH)_2$, and finally formation of hydroxyapatite, acting as protective layer against further degradation. In order to evaluate the initial effect of chitosan coating on Mg monolith physiological stability, the 48h incubation in SBF media was performed and traced by FTIR and XPS spectroscopy's. As seen from FTIR spectra on Figure 4.24 , the SBF incubation significantly alter the spectra profile of chitosan-coated Mg monolith, showing the dominant presence of carbonate (CO_3^{2-}) - related vibration as directly adsorbed (2000-2300 cm^{-1} region) or arising from formed apatite (being approved by bands at about 1547 cm^{-1}, 1440 cm^{-1}, and 840 cm^{-1}), being ionically bonded to $-PO_4^{3-}$ groups (bands at about 1049 cm^{-1}, 1049 cm^{-1}, 1033 cm^{-1}) [163]. A very low intensity of the later (PO_4^{3-} - related) vibration band, which is normally followed by less intensive carbonate-related band, may be a consequence of thick carbonate layer [164], as well as indicate on the formation of amorphous, non-stoichiometric type apatite, being already well described [176] as pre-step in hydroxyapatite formation.

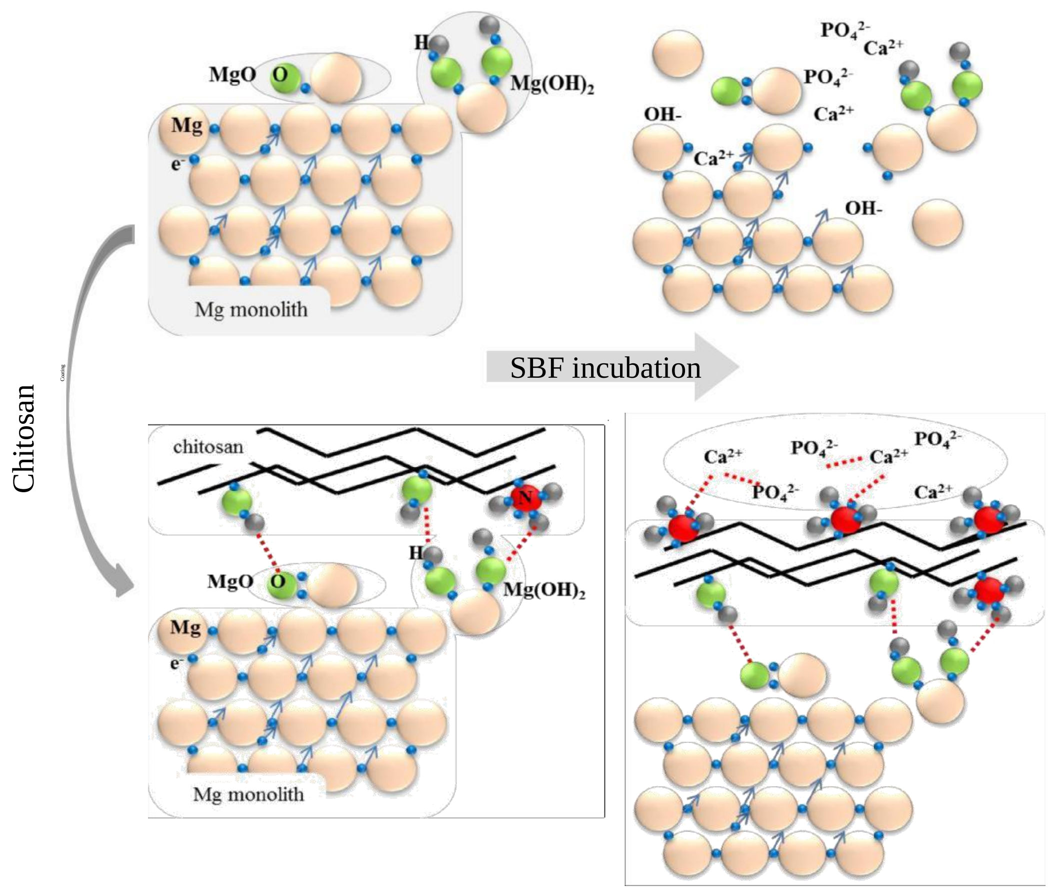

a) b)

Figure 4.25: (a). Anticipated surface and bulk phenomena of uncoated (above) and chitosan-coated (below) Mg-monolith, taking place before (a) and after (b) incubation in SBF media.

On the other hand, the XRD analysis of uncoated and chitosan-coated Mg monolith (of 14% porosity) after 48 h of incubation in SBF (Figure 4.26), revealed the presence of typical crystal planes of hydroxyapatite (visible in up-right inserted spectral lines) [175], being however (due relative low intensity) not the dominant crystalline fraction found on the Mg-monolith surface. Indeed, beside typical Mg (2theta) angles at 32°, 48°, 57° and 67° degrees for (010) (012) (110) (20) planes, the major corrosion product is $Mg(OH)_2$ as being already reported for similar experimental set-up in [14, 15]. The retention of chitosan after 48 h of incubation can anyhow not be identified with 100% accuracy due to the overlapping of $Mg(OH)_2$ with chitosan-related XRD peak, typically observed as broad peak at ~20° degrees [177].

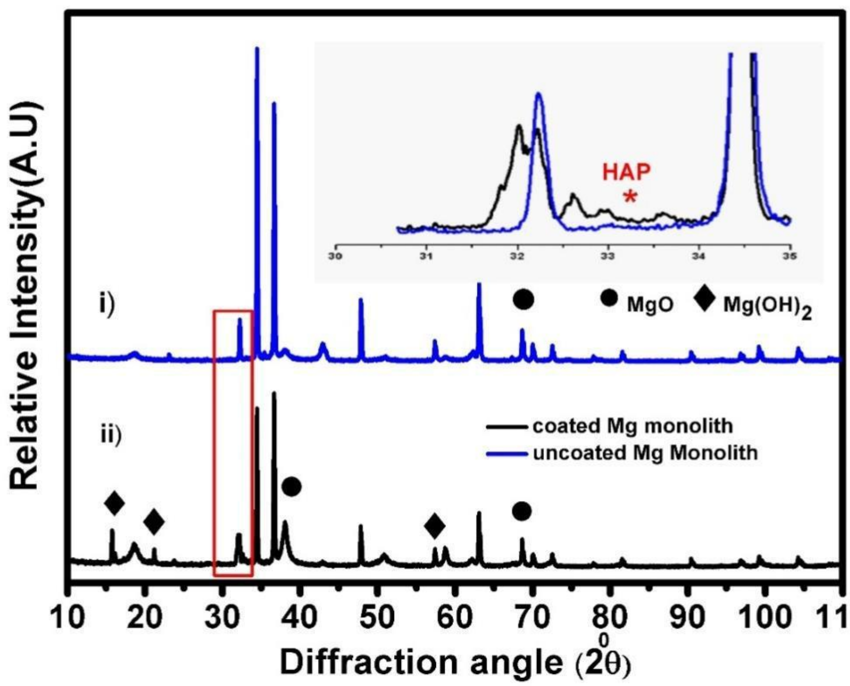

Figure 4.26: XRD spectra of i) uncoated and ii) chitosan-coated (14% porous) Mg monolith after 48 h of incubation in SBF solution. The spectral lines in HAp-related region within both samples are inserted in higher magnification for visualization purpose.

Complementary to spectroscopically-examined surface-related changes, the bulk degradation rate (being related to the removal or dissolution of Mg ions and chitosan) were evaluated gravimetrically by tracking the weight loss of monoliths and pH changes of immersion solutions as a function of time for both uncoated and chitosan-coated monoliths of different porosities. As seen from Figure 4.27(a), the weight-loss phenomenon was most significant in case of low (14%) porosity monoliths, which is increased with the increased immersion time. This corresponds to the highest grain polydispersity as well as the highest presence of grain-interfaces covered with MgO and $Mg(OH)_2$, being already elaborated by SEM image analysis for the same sample. On the other hand, the comparison between weight-loss and pH values for the uncoated and chitosan-coated Mg monoliths (Figure 4.27(b)) reveal significant variations in kinetic data between differently-porous samples, even in all cases, the chitosan protective role in degradation/corrosion process was also identify. Indeed, the weight-loss difference (between uncoated and chitosan-coated monoliths) increased twice within 120 h of incubation (from 16% to 32%) for the lowest (14%) porous monolith, leading to 6-9 % pH difference. On the other hand, the monoliths with 30% and 40% porosity gave an opposite trend during the same period, i.e. the reduction of weight-loss from about 40% to 24% and from about 50% to 22%, respectively, and significant pH change (from 8.2% to 12.7%) only in case on 40% porous sample. This result clearly implies on a protective function of chitosan layer, acting as a barrier between the porous Mg monolith surface and SBF electrolytes. This leads to a decreased degradation rate with progression of incubation, being most effective in the lowest porous monolith while at highly-porous ones the chitosan coating also penetrates, leaving the surface irregularities. The elaborated pH change is direct consequence of the corrosion process where the Cl^- ion from SBF media progressively exchange with $-OH^-$ ions within the $Mg(OH)_2$, being present on monoliths surface, leading to media alkalinity which is dominating in lowest porosity samples. In case of chitosan-coated monoliths, the surface oxides are not accessible to SBF ions to same extent, which decelerate the degradation and consequently diminish the alkalization. Due to chitosan insolubility in high pH media, these behaviour is expected to further prolong, which however need to be confirmed, although the chitosan films processed separately (using the same coating procedure) shows relatively high physiological stability (<13% weight-loss) in 15 days of SBF incubation.

EDX analysis with respective SEM micrographs (Figure 4.28 and 4.29) provide additional proof of fastest degradation of 14% porous sample. It was found that the presence of Mg, O and Cl elements in selected areas, and the calculations by the semi-quantitative ratio between these elements (inserted Table.4.1**)** could confirm the presence of Mg-oxide products and $MgCl_2$ being known to speed up the corrosion process due to its solubility [178]. Moreover, large diversity of structures, from needle- to globular- and flakes-like minerals were found as dominant on this sample (Figure 4.28) indicated by arrow. In opposite, less diversity in elements release was identified in 30% porous monolith, while Cl ions absent in case of 40% porous sample, demonstrating on higher presence of MgO related precipitates (Figure 4.29(C). Interestingly, the mineralization products were not identified on none of the samples, which may be due to the presence of too densely covered corrosion products.

a)

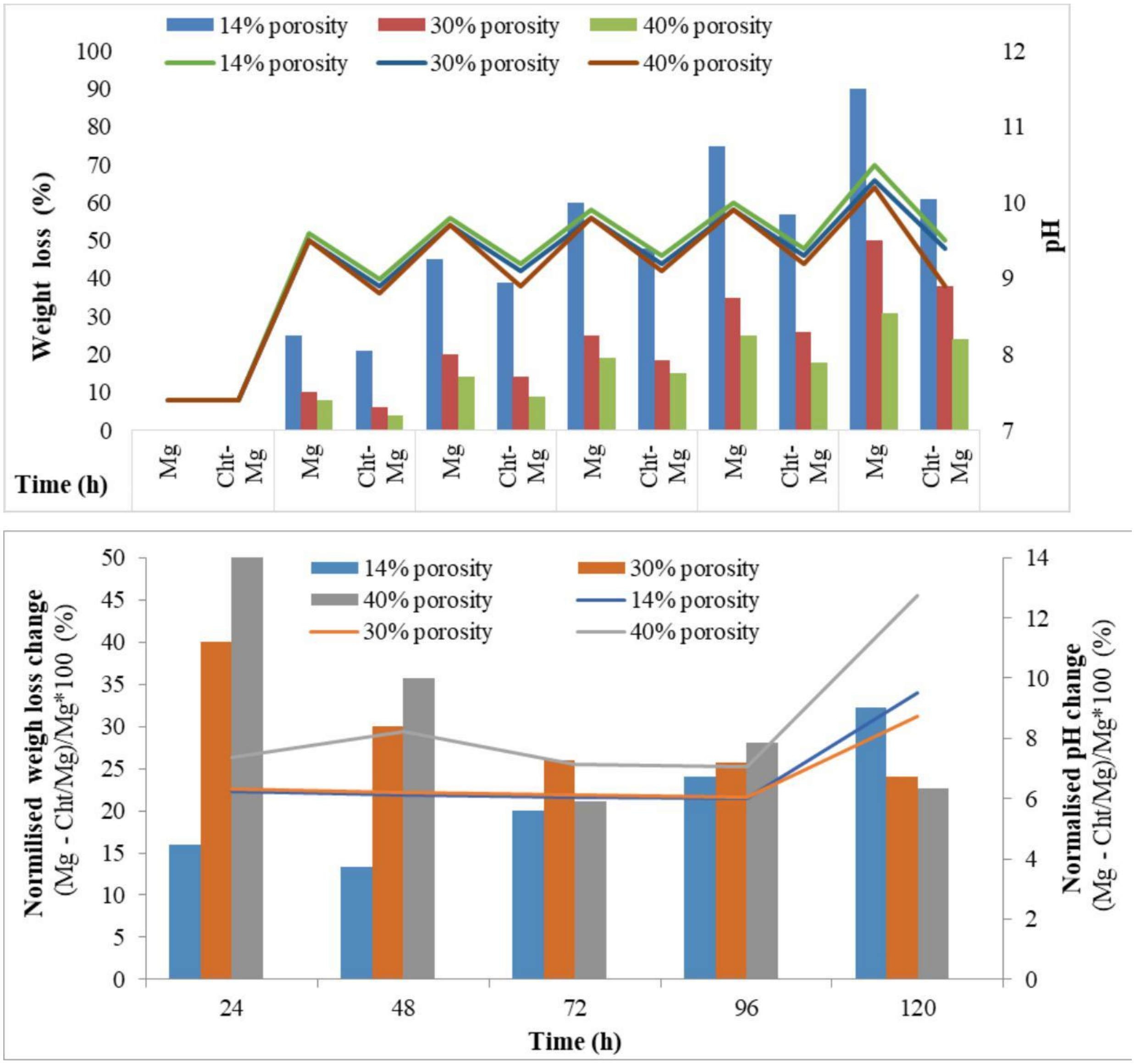

b)

Figure 4.27: The weight-loss of uncoated and chitosan-coated Mg monoliths of different porosity, and pH changes of SBF solution during 120 h of incubation at 37°C.

For better visualization of relative changes, the normalized weight-loss and pH of uncoated (Mg) respective to chitosan-coated (Cht-Mg) monoliths are presented in the graph below (b).

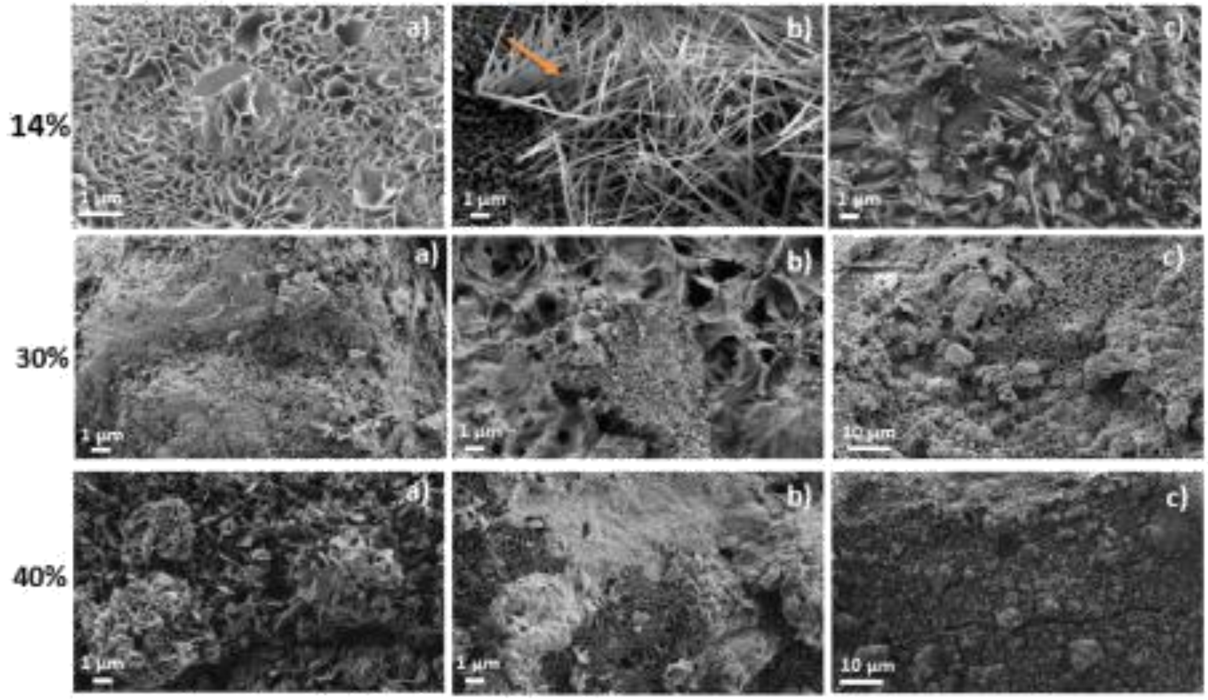

Figure 4.28: SEM images of chitosan-coated Mg monoliths of different porosity (14%, 30% and 40%) with different magnifications (A, B and C) after 48 h immersion in the SBF solution at 37°C.

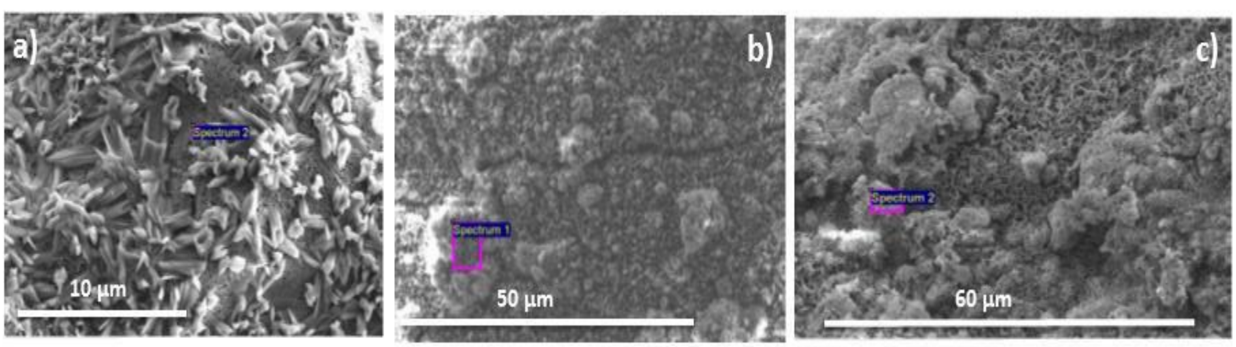

Figure 4.29: SEM-EDX analysis of chitosan-coated Mg monoliths with different porosity (A 14%, B 30%, and C 40%) after 48 h immersion in the SBF solution at 37°C.

Table 4.5: EDS elements weight and atomic percentages

Porosity	Element	Element (wt%)	Element (atomic %)
14%	O	60.54	70.51
	Mg	36.31	27.83
	Cl	3.15	1.66
30%	O	61.78	71.47
	Mg	35.68	27.30
	Cl	2.36	1.23
40%	O	62.33	71.55
	Mg	37.67	28.45

4.5.3 Mechanical properties of monoliths

The effects of different porosity as well as chitosan coating on the mechanical properties of Mg monoliths were followed by samples compressions testing. The stress-strain curves being presented on figure 4.30, exhibit the typical liner elastic regime at low strain in all samples, however, the low porosity (14%) monolith differ significantly from the others due to typical brittle failure profile, without plastic deformation, while all other one's exhibit yield peak, followed by softening and strain hardening regimes being especially pronounced in chitosan-coated Mg monoliths. The increase of porosity, negatively effect on the compression strength, reducing it for about 70% and at the same time positively effect on the elastic modulus by its increasing for the same (about 70%) extend in case of non-coated and chitosan-coated Mg monoliths with 40% of porosity. Moreover, the chitosan coating does not significantly affect the elastic modulus in low porosity sample, while, in case of highly porous a significant (about 40%) modulus reduction was measured, which directly indicate on porosity guided-elasticity, as well as on possibility for tuning of the same by controlling the Mg monoliths processing. Importantly, the obtained compression values closely match the properties of cancellous bone having 50-1000 MPa modulus and 4-12 MPa strength [32], while being much below of compact bone tissue with 17000-20000 MPa modulus and >150 MPa strength, which indicate on monoliths applicability as supporting, rather than self-standing implantation material. The PCL coatings on 35-40% porous Mg after incubation of 72h, by L.Tayebi *et al.*, showed the compressive strength of 8.8MPa [17] while the chitosan coated Mg after 120h incubation, in the present study, remarkable enhancement on compressive strength is about 26 Mpa, indicates the compatible chitosan coating on the Mg monolith.

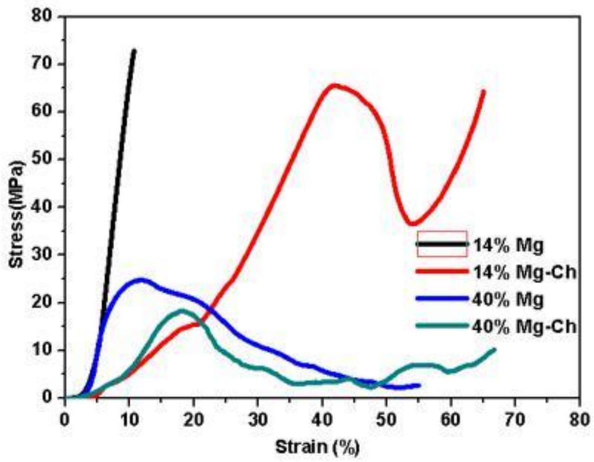

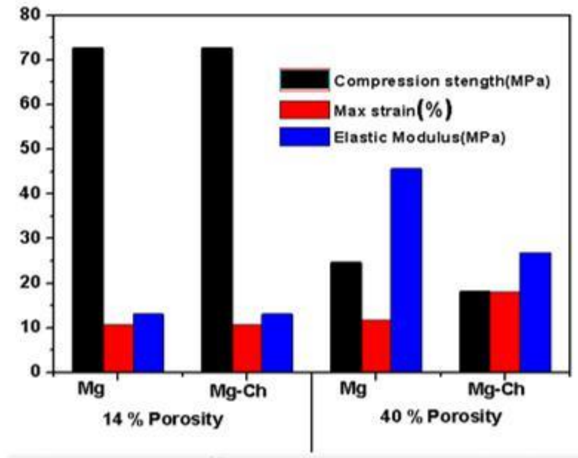

Figure 4.30: Stress-strain diagram of uncoated and chitosan-coated (14% and 40% porous) Mg monoliths (left) with extracted data for compression strength (MPa), maximum strain (%) and elastic modulus (MPa) for the same data set (right).

4.5.4 Summary

Powder metallurgy process was used to produce different porous Mg monoliths followed by dip-coating of natural biopolymer chitosan and confirmed porous structure and coatings on the monolith by structural studies. The untreated Mg monolith undergoes considerable degradation in SBF while the chitosan treatment retards the degradation and also encourages the formation of apatite layer over the sample surface. Among the different porosities attempted, 40% porous monolith was found to impart maximum resistance to the sample. Therefore, chitosan surface treatment is proposed for better longevity, as well as bioactivity of Mg monoliths to be used as biomedical implants, however, like supporting, rather than self-standing implantation material due to compression strength limitations.

4.6 *In-vitro* Studies of Polydopamine/Gelatin surface modified Porous Magnesium monoliths to control degradation rate.

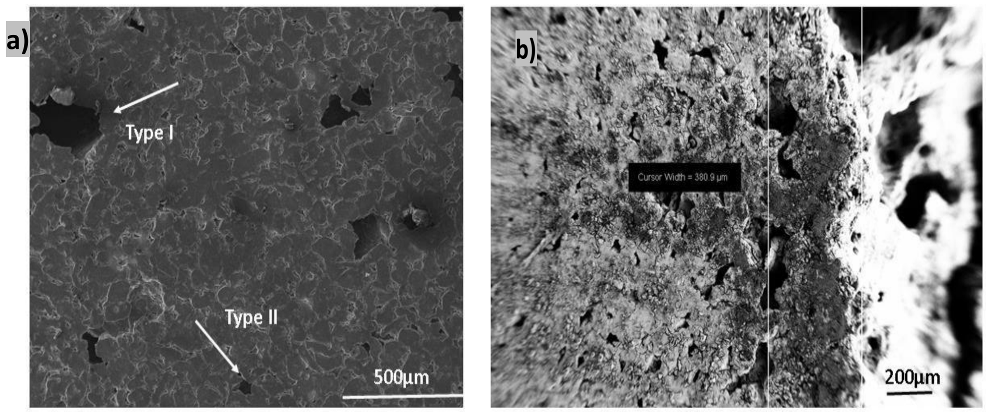

Figure 4.31: a) SEM micrograph of Mg Monolith b) PDA/GEL coated Mg monolith.

SEM micrograph of the the prepared Mg monolith shown in Figure 4.31(a) consist of two types of pores, type 1 have diameter above 250µm, and type II having up to 100 µm, the porosity volume fractions of the produced monoliths were calculated using Eq. (1), and in the range of 40-45% Figure 4.31(b) shows the PDA/GEL coated Mg monolith, the coating penetrates into the pores and formed a thick layer. The thickness of the layer is approximately 380 µm.

4.6.1 *In vitro* degradation testing

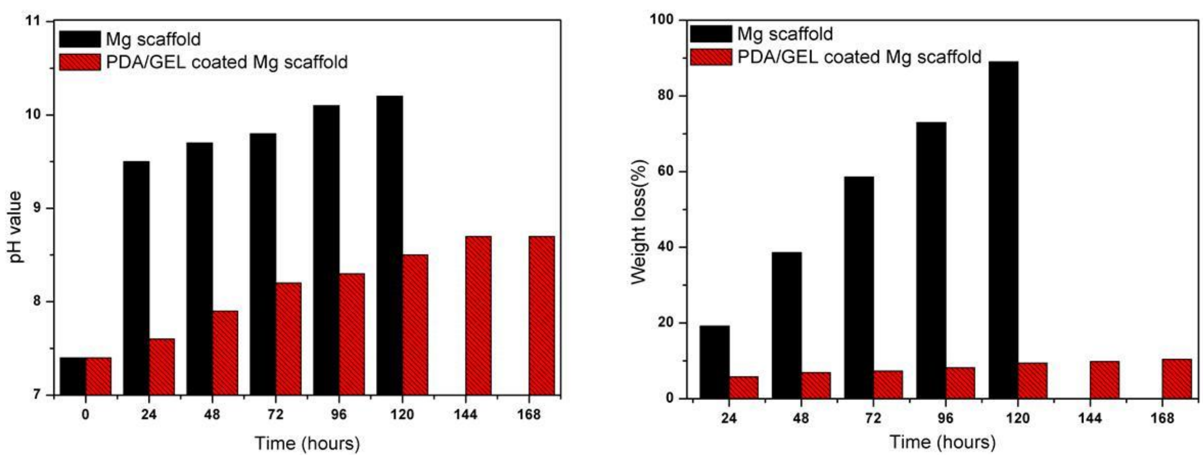

Figure 4.32: Typical results of the pH and weight loss measurements during immersion tests in SBF solution at 37˚C.

In-vitro degradation behaviour of the Mg monolith was investigated by the immersion test [160]. The monoliths were immersed for different time periods, measured the weight loss and pH as shown in Figure 4.32. Immersion factors such as immersion solution pH value variation indicate the corrosion behaviour of the coated/uncoated samples. The presence of physiological salt ions can aggressively attack the Mg and accelerate its degradation.

The weight loss vs. immersion time and pH vs. immersion time in SBF have been shown in the Figure 4.32. The difference in the weight loss for the coated and uncoated sample can be observed clearly from 24h. The visual inspection confirmed the formation of thin grey layer during first few hours of immersion in SBF indicating formation of $Mg(OH)_2$ followed by deposition of white layer consisting of corrosion products. The weight loss for uncoated sample increases from 20% to 90% from 24 h to 120 h. The uncoated sample dissolves completely after 120h. The Dopa/Gel coated sample shows the 5.8% weight loss for first 24h. Weight loss percentage increases with increase in immersion time. The change in weight loss% for the Dopa/Gel coated samples is very less compared to uncoated samples. Similarly, the pH change with immersion time can easily be observed from Figure 4.32(b). Coated monoliths displayed a lower pH value compared to the uncoated samples. The pH values for uncoated samples increases from 7.5 to 10.2 from 24h to 120h, followed by the monolith dissolution. While for the Dopa/Gel coated samples the pH change is not very significant. A pH value of 8.7 is observed for 168 h. The stabilized pH indicates that the coating protects the surface of the Mg monolith [11].

4.6.2. Chemical Composition of PDA/GEL Layer Fabricated on Magnesium monolith

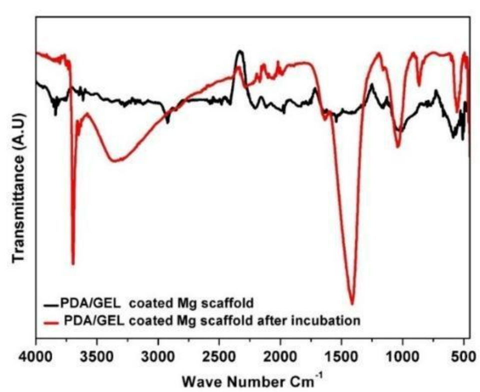

Figure 4.33: FTIR spectra of PDA/GEL coated Mg monolith before and after incubation in SBF solution after 168h.

FTIR was performed to study the corrosion products, and the spectra acquired from samples soaked in the SBF solutions before and after168h.The spectra are displayed in Figure 4.33

PDA/GEL-coated Mg shows broad absorption band in the region 3200-3100 cm^{-1}, attributed to amide-A stretching and signals at about 1643 cm^{-1}, 1534 cm^{-1} attributed to the amide bands [179], respectively. Adsorption bands located in the range of 1567 cm^{-1}, originating from the C–C stretching vibration of benzene rings and the N–H bending of the PDA structure, and 3600-3100cm^{-1} corresponding to catechol groups [180], further confirm that PDA was successfully coated on Mg-monolith.

After 168h of incubation in SBF solution, the broad absorption band from 3700 to 2500 $cm^{-1}$is attributed to the stretching vibration of the hydroxyl group. This broadband stems mainly from water, with strong H-bonding inside the structure. In contrast, a sharp absorption peak at about 3692 $cm^{-1}$is observed for the sample soaked in solution. This higher position peak is related to the free hydroxyl group indicating the presence of magnesium hydroxide [181]. The band at 1635 cm^{-1} arises from H_2O bending vibration. The apparent absorption bands at 1158 and 1038 cm^{-1} correspond to phosphate and the broadband from 864 $cm^{-1}$and 1400 cm^{-1} originates from carbonate[182]. The bands at 560 and 670 cm^{-1} correspond to hydroxyl groups mainly from magnesium hydroxide. The 450–550 cm^{-1} band can be ascribed to Mg–O bonding (MgO) [183].

4.6.3. Coating characterization

Figure 4.31(b) shows the surface of PDA/GEL coated Mg monolith consists of pores which are interconnected with, relatively uniform distribution. The PDA layer formation covers these pores on the surface; it acts as supporting inner layer which restricts corrosion; PDA/GEL coatings improve the corrosion resistance of the monolith. The SEM images show that after incubation in the SBF solution, some cracks are observed on the surface Figure 4.33(b), needle-like particles Figure 4.33(c) of HA formed on the pore structure of the surface and the flower type structure formed Figure 4.33(d).

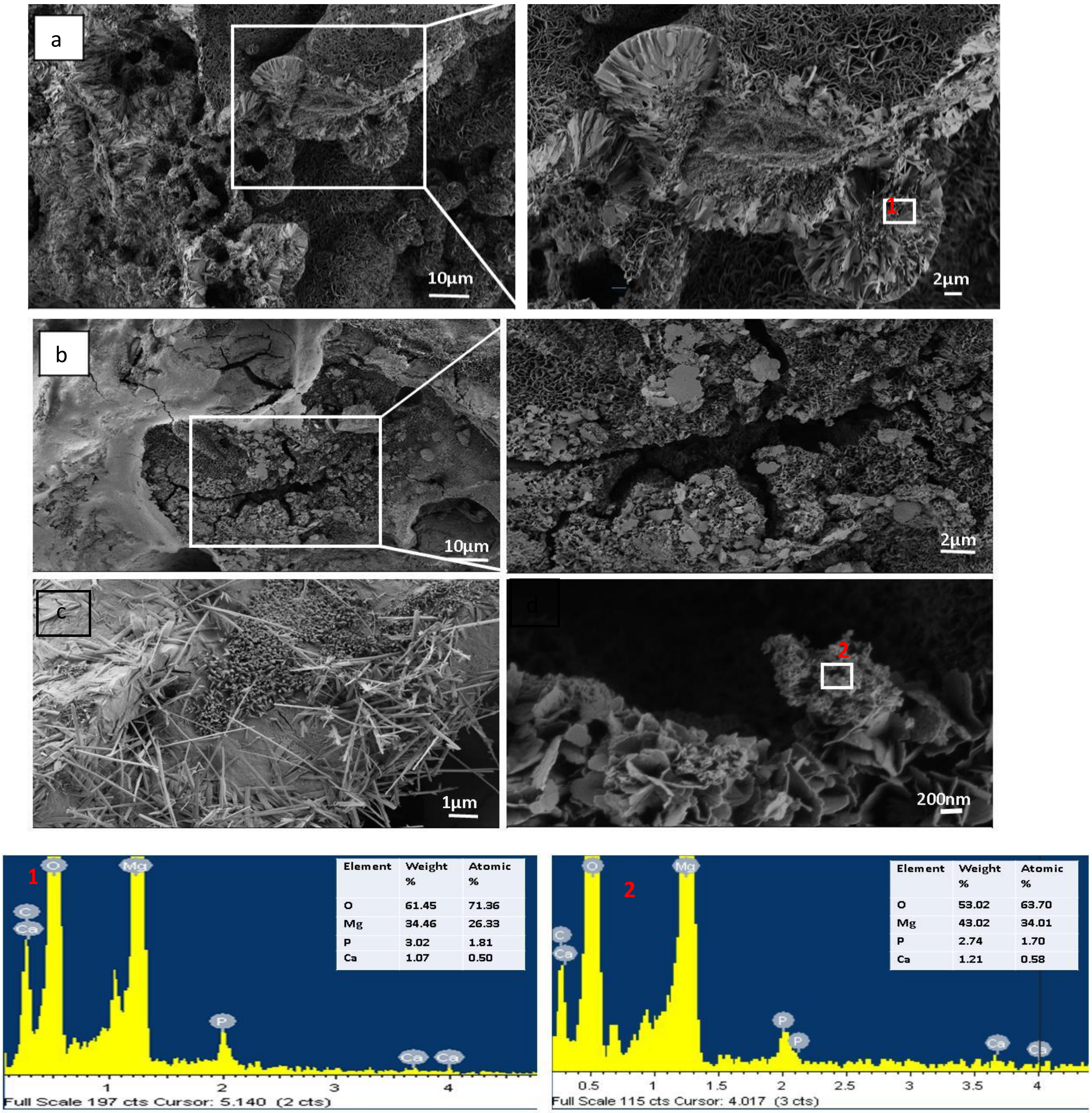

Figure 4.34: SEM and EDS of PDA/GEL coated Mg monolith after incubation in SBF solution after 168hours.

EDS analysis was employed to evaluate the elemental compositions of the PDA/GEL coated monolith, and the spectra are shown in Figure 4.34. Mg, O, and P, Ca are observed on both the surfaces, the presence of O element is due to the oxidization or passivation of the surface. Oxygen content of the corrosion surface can present the main corrosion product content because oxygen is the most abundant element in the corrosion products of Mg alloy. Moreover, Ca and P are obviously observable for the PDA/GEL coated Mg monolith, which preliminarily confirms the formation of HA coatings.

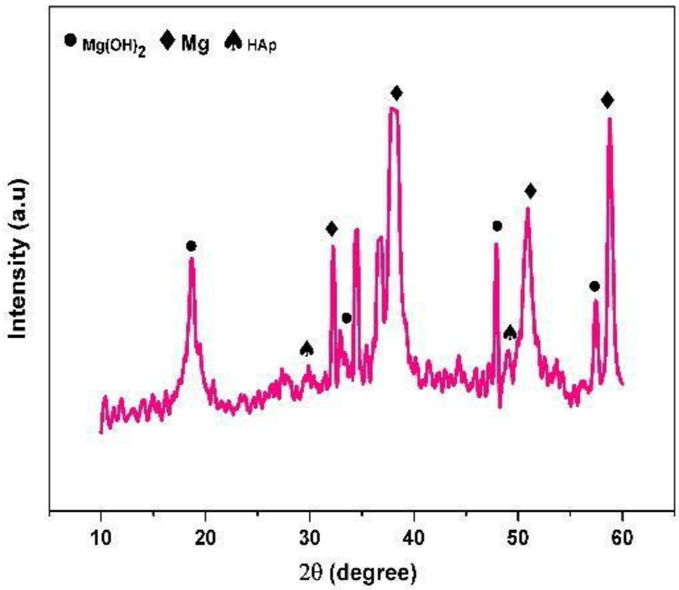

Figure 4.35: XRD analysis of PDA/GEL coated Mg monolith after incubation in SBF solution after 168 hours.

On the other hand, the XRD analysis PDA/GEL coated Mg Monolith after the incubation in SBF (Figure 4.35), revealed the presence of typical crystal planes of hydroxyapatite, magnesium hydroxides which is good agreement with the EDS results.

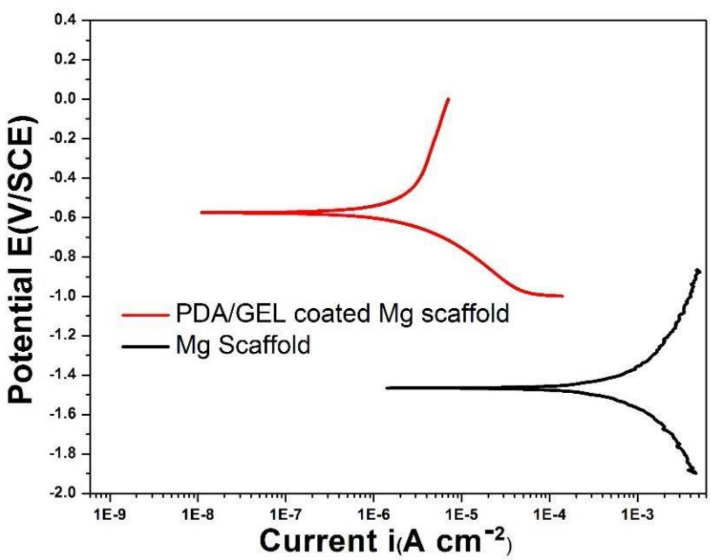

Figure 4.36: PDP plots of Mg Monolith and DOPA/GEL Mg monolith.

Figure 4.36 shows the PDP studies for the uncoated and PDA/GEL coated monoliths. The ability of the PDA/GEL coating to protect Mg surface from corrosion in SBF solution studied by electrochemical experiments. The difference in the polarization curves between the untreated sample and the sample is shown Figure 4.36 .The polarization curve of coated monoliths shows of corrosion potential to more positive values (-1466 mV) compared to uncoated monolith (-640 mV), and the coated samples have a much smaller corrosion current density, thereby indicating that the coated monolith has a much better corrosion than uncoated one. Table 4.6 summarizes the E_{corr} and I_{corr} of coated and uncoated monoliths. The E_{corr} of coated monolith decreases to a less negative value compared to uncoated, indicating an insignificant affinity to corrode, in the case of Icorr also lowest values are observed for coated monolith.

Table 4.6: Electrochemical data from the polarization curves

Sample	Ecorr/V	Icorr/μA /cm^2	Rp/kΩ
Mg Monolith	-1.466	326.2	10
PDA/GEL Mg monolith	-0.640	1.43	70

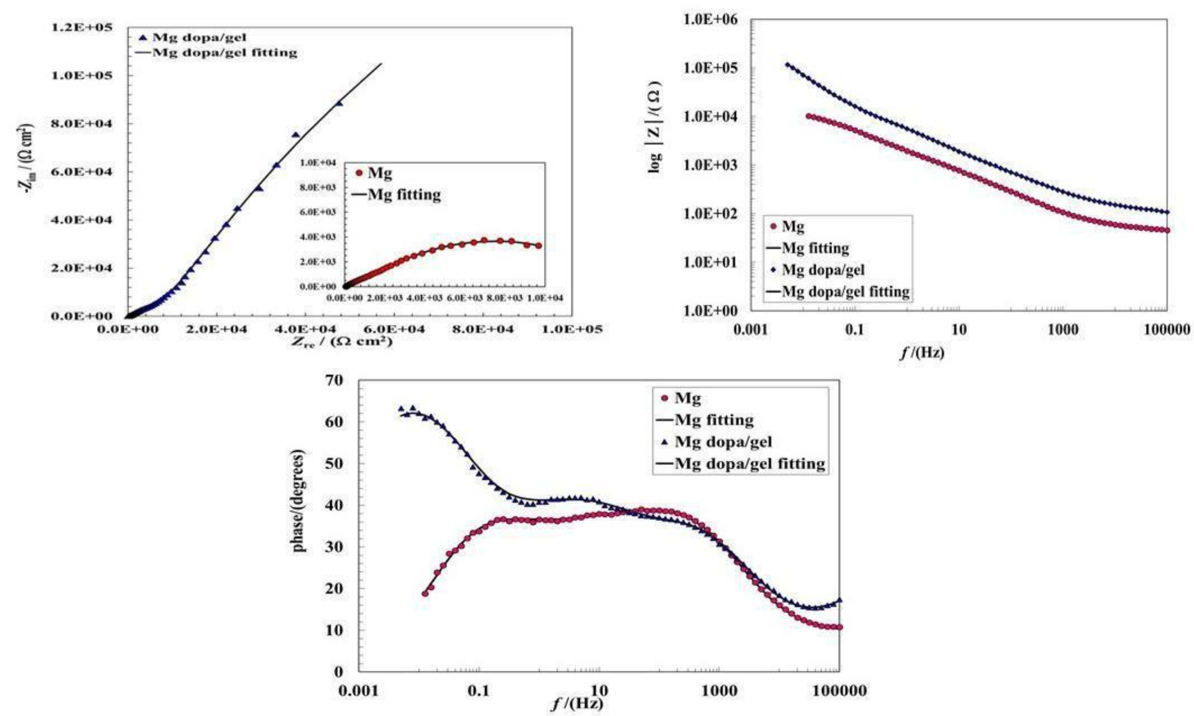

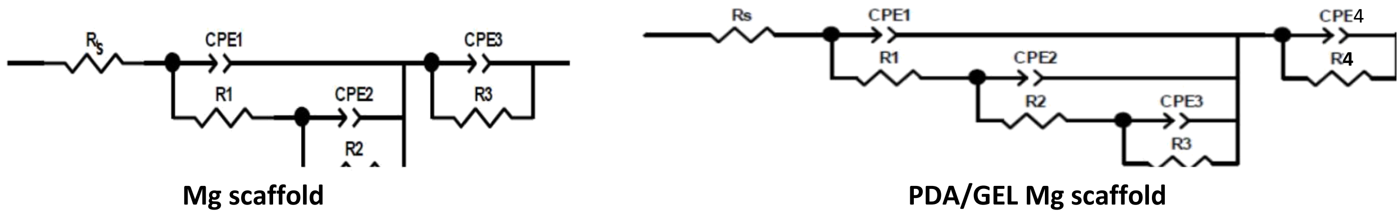

Figure 4.37: Nyquist and Bode Plots Mg Monolith and DOPA/GEL Mg monolith with equivalent circuits.

Table 4.7: Equivalent circuit curve fitting parameters of EIS results

Sample	C_1 (F cm^{-2})	n_1	R_1 (cm^2)	C_2 (F cm^{-2})	n_2	R_2 (cm^2)	C_3 (F cm^{-2})	n_3	R_3 (cm^2)	C_4 (F cm^{-2})	n_4	R_4 (cm^2)
Mg monolith	6.5047E-08	0.9797	11.62	3.0528E-05	0.5413	9.67E+02	4.8575E-04	0.6189	1.37E+04			
PDA/GEL-coated Mg monolith	4.54E-09	0.6104	99.06	4.608E-06	0.6993	2.41E+02	4.516E-05	0.5444	1.10E+04	1.471E-05	0.8804	9.25E+05

The polarisation resistance (R_p) values for uncoated sample was around 10 kΩ cm^2, whereas for the PDA /GEL coated Mg monolith samples were found to be 70 kΩ cm^2. Nyquist curve is shown in Figure 4.36. The dopa/GEL coated Mg monolith displays larger diameter compared to the uncoated sample. The PDA/GEL layer acts as barrier layer and improves the corrosion resistance.

Electrochemical impedance spectroscopy (EIS) provides a rapid and convenient technique to evaluate the performance of organic coated metals(Table 4.7). The coating system's resistance generally degrades with time. This degradation is associated with ion and water penetration into the coating and the subsequent electrochemical (corrosion) reaction at the coating/metal interface.

The impedance spectra can be divided into three different parts: the high frequency part (HF) part represents the properties of the coating, the second segment is approximately within the middle frequency region, and the low-frequency (LF) part represents the reactions occurring at the bottom of the pores of the coating or on the interfacial Mg oxide/hydroxides layer underneath the coating.

The first-time constant within the high frequency region (R_1CPE_1) could represent the charge-transfer process of metal dissolution, where R_1 describes the charge-transfer resistance and the constant phase element CPE_1 relating to the double layer capacitor (as n_1 is almost equal to 1). The parameter which represent double layer capacitance, C_{dl} is normally absent on protective systems. The beginning of its detection occurs with the initiation of the electrochemical activity of the metal substrate. Thus, C_{dl} appears after film degradation or when defects exist. The R_1 CPE_1 elements show in the case of PDA/GEL coating the impedance with the interface reaction between the film (PDA/GEL coati) and substrate (Mg). With respect to the fact that the value of the parameter n_1= 0.6104 it could be stated that the first loop (R_1 CPE_1) appeared at the high frequency region is attributed to the pore resistance, which relates the corrosion process occurring within pores of coating (Table 4.7). The second and the third segment (R_2 CPE_2,R_3 CPE_3) are approximately within the middle frequency region. On the basis of the Bode magnitude plot which represents the impedance modulus versus frequency, the delamination of the coating (the penetration of the electrolyte into the micro porosity of the organic film) from the substrate can be affirmed. The horizontal section of the line at lower frequencies (in our case between 10 – 1 Hz) is characteristic for this phenomenon. Moreover, the third relaxation, R_3CPE_3 is ascribed to the diffusion process; the parameter n_3 was found to be around 0.5. This means that Cl^-containing electrolyte soaked to the metal/coating interface, and started corrosion lead to formation of MgO and/or Mg $(OH)_2$. Since magnesium alloys are highly electrochemically activity, corrosion usually propagates quickly once the corrosive electrolyte reaches Mg surface. Observed passivation phenomenon was attributed to the blockage of the pathways by the corrosion products. This statement could be affirmed with the fact that resistance R_2 and $\boldsymbol{R}_3$ had increased.

Finally the fourth relaxation, R_4CPE_4 (within the lowest frequency region), could be ascribed to the process where the formed MgO and/or Mg $(OH)_2$ probably filled the gaps within the PDA/GEL coating. This could be confirmed by increasing values of the impedance parameters i.e., R_4 and n_4. The resistance value $\boldsymbol{R}_4$ has been increased again and it is for a one order of magnitude higher than that of the sample without coating (Mg monolith - $\boldsymbol{R}_3$).

From this viewpoint, good protective properties were achieved with PDA/GEL coating.

4.6.4. Mechanical Properties

The compressive strength of the uncoated Mg monolith after 24 hour decreases from 48 to 15 MPa because of degradation of Mg in SBF solution. In the case of PDA/GEL coated Mg monoliths, higher in the compression strength when compared to uncoated one after 24 hours. The compression strength is good even after the incubation of 336 hrs. it confirms the PDA/GEL layer protects the magnesium surface, when compared to other coatings on the Mg monoliths [42-46], PDA/GEL, exhibits the better mechanical properties as shown below Table 4.8. . When compared to other coatings on the Mg scaffolds, PDA/GEL exhibits the better mechanical properties as shown below table.4.9

Table 4.8: Compressive strength of the Mg monolith, and PDA/GEL Mg monolith before immersion test and after the immersion of the samples for 24, 144 and 336h in SBF solution.

Compressive Strength (MPa)	Immersion time (h)			
	0h	24h	144h	336h
Mg Monolith	48	15.82	-	-
PDA/GEL Mg monolith	48	28.89	27.45	8.74

In this study, PDA and GEL were used to coat the corrosion protective and bio - functionalization coating, marked PDA/GEL conversion coating, on magnesium monoliths. The fabrication of the PDA/GEL conversion coating is simple and less cost and easily available. PDA/GEL coating Mg monoliths attach the functional groups such as primary amines, hydroxyl and carboxyl groups acts a bio-functional groups which helps to decrease the corrosion rate on the magnesium monoliths. PDA/GEL coating penetrates into the pores and binding with the magnesium were expected to perform good corrosion resistance to the monolith in the SBF solution. From the PDP and EIS measurements, PDA/GEL Mg monolith resulting a lowest corrosion current density and higher polarization resistance from the impedance compared to Mg monolith. PDA/GEL coating layer acts as barrier and stops the ions exchange between the Mg monolith and the SBF solution, leads to decrease the release of the magnesium ions. The

Table 4.9: Mechanical properties of porous Mg biomaterials

Materials	**Porosity (%)**	**Compression strength (MPa)**		**Reference**
		Before immerison in artificial body fluids	**After immerison in artificial body fluids**	
Cancellous bone		0.2-80	-	[184]
PDA/GEL Mg scaffold	40-45	48	T=24h, c=28.89 T=144h, c=27.45 T=336h, c=8.74	Present work
Porous Mg	40-45	48	T=24h, c=15.82	
Porous Mg	50	30	-	[185]
HAp/Mg scaffold	60	15		
Porous Mg	35-40	52	T=24h, c=12.2	[16]
Porous Mg	54-55	41-46	-	[186]
Porous Mg	35	27	-	[187]
Mg scaffold/6% PCL	35-40	52	T=24h, c=22 T=48h, c=14 T=72h, c=8.8	[17,188]
Mg scaffold/6PCL-BG	35-40	52	T=24h, c=36 T=48h, c=29 T=96h, c=20 T=144h, c=17	[15]
Mg scaffold/PCL-BaG/Gel-BaG	35-40	44	T=24h, c=36.08 T=72h, c=28.6 T=120h, c=27.72 T=144h, c=18.48 T=240h, c=14.5	[189]

T = time period, c = compression strength.

immersion tests also shown the excellent corrosion resistance to the PDA/GEL coatings, because of PDA layer enables the gelatin B immobilization[190], became more dense and blocks the ions exchange and also expected to be the attached bio-functional groups of PDA/GEL structure chemically hinders the release of magnesium ions.

4.6.5. Summary

This work is done on Mg Monolith and PDA/GEL coated Mg Monolith for tissue engineering applications. This novel PDA/GEL on Mg monolith gives rise biopolymer non-toxic coat. The following conclusions were investigated:

1. FTIR, XRD and SEM and analysis of the coated films indicated the formation of a stable compact and smooth passive film of Mg $(OH)_2$ and HA incorporated in the Mg monolith which is useful for biomedical applications.

2. PDA/GEL coating has the highest polarization resistance of 70kΩ cm^2 due to the complete coverage of Mg surface protecting it from corrosion.

3. Lowest corrosion current density of 1.43 μA cm^{-2} was observed for compared to uncoated due to the enhancement of the protective properties of the passive layer for this coating.

4. PDA/GEL coating has enhanced mechanical properties compared to other

coatings Confirming its high protection for bone.

Chapter 5

5.1 Conclusions:

1. General corrosion resistance of the materials tested follow the trend Mg-4Ag > Mg-5Gd > Mg as shown with the EIS measurements, however, the difference between the materials tested is not high. Corrosion of all three materials tested is under chemical reaction control, but not under diffusion control. Pure Mg and Mg-4Ag have repassivation ability, whereas Mg-5Gd does not possess such property as found based on the cyclic polarisation measurements.

2. *In-situ* cross-linking of gelatine (GEL) coating by carbodiimide chemistry was successfully applied on the surface of the AZ91 Mg alloy by a dip coating technique. The presence of GEL was confirmed by the FTIR spectroscopy and SEM imaging, resulted to a coating morphology with complete and uniform surface coverage and the formation of spongy-flower like carbonate containing mineral structures after 30 days of immersion in simulated body fluid. Moreover, an extended (from 2.08 to 1.19 mm/year) corrosion protection of GEL-coated AZ91 Mg alloy in SBF solution was confirmed by electrochemical studies, which may provide a bio-safer pH environment (pH 8.3) during potential *in vivo* application. Therefore, the proposed cross-linked, GEL-based coating can be an alternative for uncoated Mg alloys, offering improved degradation behaviour in orthopaedic applications; however, further studies are required to improve the mechanical stability and the long-term corrosion protection ability of such a coating.

3. The coated CA nanofibers were characterized by using FE-Scanning Electron Microscopy (FE-SEM). Fiber diameter is observed from 250-400 nm. The SEM observations of the samples indicate white precipitates on the samples. EDS analysis shows the presence of Mg, O, Ca, P. The presence of Ca and P and O indicates the formation of hydroxyapatite. Electrochemical studies identified that Nano fibrous sample shows better corrosion resistance when compared to pure magnesium. Very low current density was obtained for CA coated Magnesium compared to that of pure Mg, EIS results exhibited high corrosion resistance indicating a highly stable film on CA coated Mg compared to pure magnesium.

4. Powder metallurgy process was used to produce different porous Mg monoliths followed by dip-coating of natural biopolymer chitosan, which confirmed porous structure and coatings on the monolith by structural studies. The untreated Mg monolith undergoes considerable degradation in SBF while the chitosan treatment retards the degradation and also encourages the formation of apatite layer over the sample surface among different porosities attempted, 40% porous monolith was found to impart maximum resistance to the sample. Therefore, chitosan surface treatment is proposed for better longevity, as well as bioactivity of Mg monoliths for biomedical implants, however, it may be useful for supporting, rather than self-standing implantation material due to compression strength limitations.

5. PDA/GEL coating on Mg monolith yielded a stable layer of non-toxic biopolymer. FTIR, XRD and SEM and analysis of the coated films indicated the formation of a stable compact and smooth passive film of $Mg(OH)_2$ and HA incorporated in the Mg monolith which is useful for biomedical applications. Coating sample shows the highest polarization resistance of 70kΩ cm^2 due to the complete coverage of Mg surface protecting it from corrosion. PDA/GEL coating has enhanced mechanical properties compared to other coatings.

5.2 Scope for future work:

Since chitosan-based polymersand cellulose and gelatine are naturally occurring materials and abundant in nature and are biocompatible, the urge to employ those polymers as coating materials for the magnesium-based implants have been increased largely over the last years. The coatings generated from these green polymers showed promising results in regard of reduction of corrosion rate, improved mechanical properties. Also, they were involved in minimizing the speed of degradation rate of both alloys such pure magnesium and magnesium-based alloys. They also, appeared to promote cell adhesion, migration and proliferation of osteoblast cells. Even though only a very few studies have been performed with cellulose-based polymers, to investigate the performance of the coating related to corrosion inhibition for bone-related applications, elobarate studies in the utilization of especially, several new functional cellulosic materials are still being carried out in order to obtain a mechanically stable magnesium-based implants with tailored surface and corrosion properties for bone engineering applications.

Chapter 6

6.1 REFERENCES:

[1] Y.F. Zheng, X.N. Gu, F. Witte, Biodegradable metals, Mater. Sci. Eng. R Reports. 77 (2014) 1–34. doi:10.1016/j.mser.2014.01.001.

[2] H. Li, Y. Zheng, L. Qin, Progress of biodegradable metals, (2014).

[3] Y. Chen, Z. Xu, C. Smith, J. Sankar, Recent advances on the development of magnesium alloys for biodegradable implants, Acta Biomater. 10 (2014) 4561–4573. doi:10.1016/J.ACTBIO.2014.07.005.

[4] F. Witte, Reprint of: The history of biodegradable magnesium implants: A review., Acta Biomater. 23 Suppl (2015) S28-40. doi:10.1016/j.actbio.2015.07.017.

[5] Q. Chen, G.A. Thouas, Metallic implant biomaterials, Mater. Sci. Eng. R Reports. 87 (2015) 1–57. doi:10.1016/j.mser.2014.10.001.

[6] K.F. Farraro, K.E. Kim, S.L.-Y. Woo, J.R. Flowers, M.B. McCullough, Revolutionizing orthopaedic biomaterials: The potential of biodegradable and bioresorbable magnesium-based materials for functional tissue engineering, J. Biomech. 47 (2014) 1979–1986. doi:10.1016/j.jbiomech.2013.12.003.

[7] R.B. Minkowitz, S. Bhadsavle, M. Walsh, K.A. Egol, Removal of Painful Orthopaedic Implants After Fracture Union, JBJS. 89 (2007). http://journals.lww.com/jbjsjournal/Fulltext/2007/09000/Removal_of_Painful_Orthopaedic_Implants_After.3.aspx.

[8] A.R. Amini, C.T. Laurencin, S.P. Nukavarapu, Bone Tissue Engineering: Recent Advances and Challenges, Crit. Rev. Biomed. Eng. 40 (2012) 363–408. doi:10.1615/CritRevBiomedEng.v40.i5.10.

[9] F. Mahyudin, L. Widhiyanto, H. Hermawan, Biomaterials in orthopaedics, Adv. Struct. Mater. 58 (2016) 161–181. doi:10.1007/978-3-319-14845-8_7.

[10] A.R. Amini, J.S. Wallace, S.P. Nukavarapu, Short-Term and Long-Term Effects of Orthopedic Biodegradable Implants, J. Long. Term. Eff. Med. Implants. 21 (2011) 93– 122. doi:10.1615/JLongTermEffMedImplants.v21.i2.10.

[11] A. Oriňák, R. Oriňáková, Z. Králová, A. Turoňová, M. Kupková, M. Hrubovčáková, J. Radoňák, R. Džunda, Sintered metallic foams for biodegradable bone replacement materials, J. Porous Mater. 21 (2014) 131–140. doi:10.1007/s10934-013-9757-4.

[12] Y. Chen, Z. Xu, C. Smith, J. Sankar, Recent advances on the development of magnesium alloys for biodegradable implants., Acta Biomater. 10 (2014) 4561–4573. doi:10.1016/j.actbio.2014.07.005.

[13] L. Pompa, Z.U. Rahman, E. Munoz, W. Haider, Surface characterization and cytotoxicity response of biodegradable magnesium alloys., Mater. Sci. Eng. C. Mater. Biol. Appl. 49 (2015) 761–8. doi:10.1016/j.msec.2015.01.017.

[14] C.E. Wen, Y. Yamada, K. Shimojima, Y. Chino, H. Hosokawa, M. Mabuchi, Compressibility of porous magnesium foam: dependency on porosity and pore size, Mater. Lett. 58 (2004) 357–360. doi:10.1016/S0167-577X(03)00500-7.

[15] M. Yazdimamaghani, M. Razavi, D. Vashaee, L. Tayebi, Surface modification of biodegradable porous Mg bone scaffold using polycaprolactone/bioactive glass composite., Mater. Sci. Eng. C. Mater. Biol. Appl. 49 (2015) 436–44. doi:10.1016/j.msec.2015.01.041.

[16] M. Yazdimamaghani, M. Razavi, D. Vashaee, L. Tayebi, Development and degradation behavior of magnesium scaffolds coated with polycaprolactone for bone tissue engineering, Mater. Lett. 132 (2014) 106–110. doi:10.1016/j.matlet.2014.06.036.

[17] M. Yazdimamaghani, M. Razavi, D. Vashaee, L. Tayebi, Development and degradation behavior of magnesium scaffolds coated with polycaprolactone for bone tissue engineering, Mater. Lett. 132 (2014) 106–110. doi:10.1016/j.matlet.2014.06.036.

[18] X.N. Gu, Y.F. Zheng, A review on magnesium alloys as biodegradable materials, Front. Mater. Sci. China. 4 (2010) 111–115. doi:10.1007/s11706-010-0024-1.

[19] A. Madhankumar, E. Thangavel, S. Ramakrishna, I.B. Obot, H.C. Jung, K.S. Shin, Z.M. Gasem, H. Kim, D.-E. Kim, Multi-functional ceramic hybrid coatings on biodegradable AZ31 Mg implants: electrochemical, tribological and quantum chemical aspects for orthopaedic applications, RSC Adv. 4 (2014) 24272–24285. doi:10.1039/C4RA02363C.

[20] P. Dauphin-Ducharme, J. Mauzeroll, Surface Analytical Methods Applied to Magnesium Corrosion., Anal. Chem. (2015). doi:10.1021/ac504576g.

[21] Y. Liu, K. Li, T. Luo, M. Song, H. Wu, J. Xiao, Y. Tan, M. Cheng, B. Chen, X. Niu, R. Hu, X. Li, H. Tang, Powder metallurgical low-modulus Ti–Mg alloys for biomedical applications, Mater. Sci. Eng. C. 56 (2015) 241–250. doi:10.1016/j.msec.2015.06.010.

[22] R.K. Singh Raman, S. Jafari, S.E. Harandi, Corrosion fatigue fracture of magnesium alloys in bioimplant applications: A review, Eng. Fract. Mech. 137 (2015) 97–108. doi:10.1016/j.engfracmech.2014.08.009.

[23] X. Zhang, X.W. Li, J.G. Li, X.D. Sun, Preparation and characterizations of bioglass ceramic cement/ca-p coating on pure magnesium for biomedical applications, ACS Appl. Mater. Interfaces. 6 (2014) 513–525. doi:10.1021/am404574t.

[24] A. Zomorodian, F. Brusciotti, A. Fernandes, M.J. Carmezim, T. Moura e Silva, J.C.S. Fernandes, M.F. Montemor, Anti-corrosion performance of a new silane coating for corrosion protection of AZ31 magnesium alloy in Hank's solution, Surf. Coatings Technol. 206 (2012) 4368–4375. doi:10.1016/j.surfcoat.2012.04.061.

[25] H. Brar, M. Platt, M. Sarntinoranont, P. Martin, M. Manuel, Magnesium as a biodegradable and bioabsorbable material for medical implants, JOM. 61 (2009) 31–34. doi:10.1007/s11837-009-0129-0.

[26] M.P. Staiger, A.M. Pietak, J. Huadmai, G. Dias, Magnesium and its alloys as orthopedic biomaterials: A review, Biomaterials. 27 (2006) 1728–1734. doi:10.1016/j.biomaterials.2005.10.003.

[27] Y. Chen, S. Zhao, B. Liu, M. Chen, J. Mao, H. He, Y. Zhao, N. Huang, G. Wan, Corrosion-Controlling and Osteo-Compatible Mg Ion-Integrated Phytic Acid (Mg-PA) Coating on Magnesium Substrate for Biodegradable Implants Application, Appl. Mater. Interfaces. 6 (2014) 19531–19543.

[28] P.K. Bowen, C.T. McNamara, O.P. Mills, J. Drelich, J. Goldman, FIB-TEM Study of Magnesium Corrosion Products after 14 Days in the Murine Artery, ACS Biomater. Sci. Eng. 1 (2015) 919–926. doi:10.1021/acsbiomaterials.5b00044.

[29] M.P. Staiger, A.M. Pietak, J. Huadmai, G. Dias, Magnesium and its alloys as orthopedic biomaterials: a review., Biomaterials. 27 (2006) 1728–34. doi:10.1016/j.biomaterials.2005.10.003.

[30] G. Song, Control of biodegradation of biocompatable magnesium alloys, Corros. Sci. 49 (2007) 1696–1701. doi:10.1016/j.corsci.2007.01.001.

[31] X.N. Gu, W.R. Zhou, Y.F. Zheng, Y. Liu, Y.X. Li, Degradation and cytotoxicity of lotus-type porous pure magnesium as potential tissue engineering scaffold material, Mater. Lett. 64 (2010) 1871–1874. doi:10.1016/j.matlet.2010.06.015.

[32] F. Geng, L. Tan, B. Zhang, C. Wu, Y. He, J. Yang, K. Yang, Study on beta-TCP Coated Porous Mg as a Bone Tissue Engineering Scaffold Material, J. Mater. Sci. Technol. 25 (2009) 123–129.

[33] S. Cabeza, G. Garcés, P. Pérez, P. Adeva, Properties of WZ21 (%wt) alloy processed by a powder metallurgy route., J. Mech. Behav. Biomed. Mater. 46 (2015) 115–26. doi:10.1016/j.jmbbm.2015.02.022.

[34] Y.H. Xia, B.P. Zhang, C.X. Lu, L. Geng, Improving the corrosion resistance of Mg-4.0Zn-0.2Ca alloy by micro-arc oxidation., Mater. Sci. Eng. C. Mater. Biol. Appl. 33 (2013) 5044–50. doi:10.1016/j.msec.2013.08.033.

[35] T.S.N. Sankara Narayanan, I.S. Park, M.H. Lee, Strategies to improve the corrosion resistance of microarc oxidation (MAO) coated magnesium alloys for degradable implants: Prospects and challenges, Prog. Mater. Sci. 60 (2014) 1–71. doi:10.1016/j.pmatsci.2013.08.002.

[36] Y. Chen, H. Qian, X. Wang, P. Liu, G. Yan, L. Huang, J. Yi, To improve corrosion resistance and hemocompatibility of magnesium alloy via cathodic plasma electrolytic deposition combined with surface thiol-ene photopolymerization, Mater. Lett. 158 (2015) 178–181. doi:10.1016/j.matlet.2015.05.163.

[37] M.A. Surmeneva, A.I. Tyurin, T.M. Mukhametkaliyev, T.S. Pirozhkova, I.A. Shuvarin, M.S. Syrtanov, R.A. Surmenev, Enhancement of the mechanical properties of AZ31 magnesium alloy via nanostructured hydroxyapatite thin films fabricated via radio-frequency magnetron sputtering., J. Mech. Behav. Biomed. Mater. 46 (2015) 127–36. doi:10.1016/j.jmbbm.2015.02.025.

[38] Q.T. and H. Liu, Electrophoretic deposition and characterization of nanocomposites and nanoparticles on magnesium substrates, Nanotechnology. 26 (2015) 175102. http://stacks.iop.org/0957-4484/26/i=17/a=175102.

[39] A.M. Kumar, S.H. Kwon, H.C. Jung, Y.H. Park, H.J. Kim, K.S. Shin, Fabrication and Electrochemical Corrosion Behavior of PEO Coatings on Strip-Cast AZ31Mg Alloy in 3 . 5 % NaCl Solution, (2014).

[40] Y.F. Zheng, X.N. Gu, F. Witte, Biodegradable metals, Mater. Sci. Eng. R Reports. 77 (2014) 1–34. doi:10.1016/j.mser.2014.01.001.

[41] M.H. Kang, H. Do Jung, S.W. Kim, S.M. Lee, H.E. Kim, Y. Estrin, Y.H. Koh, Production and bio-corrosion resistance of porous magnesium with hydroxyapatite coating for biomedical applications, Mater. Lett. 108 (2013) 122–124. doi:10.1016/j.matlet.2013.06.096.

[42] Z. Zhen, T.F. Xi, Y.F. Zheng, Surface Modification of Magnesium and its Alloys for Biomedical Applications, Elsevier, 2015. doi:10.1016/B978-1-78242-078-1.00011-6.

[43] S. Kunjukunju, A. Roy, M. Ramanathan, B. Lee, J.E. Candiello, P.N. Kumta, A layer-by-layer approach to natural polymer-derived bioactive coatings on magnesium alloys, Acta Biomater. 9 (2013) 8690–8703. doi:10.1016/j.actbio.2013.05.013.

[44] R.-C. Zeng, X.-T. Li, S.-Q. Li, F. Zhang, E.-H. Han, In vitro degradation of pure Mg in response to glucose, Sci. Rep. 5 (2015) 13026. http://dx.doi.org/10.1038/srep13026.

[45] F. Witte, The history of biodegradable magnesium implants: A review, Acta Biomater. 6 (2010) 1680–1692. doi:10.1016/j.actbio.2010.02.028.

[46] W. Ding, Opportunities and challenges for the biodegradable magnesium alloys as next-generation biomaterials, Regen. Biomater. 3 (2016) 79–86. doi:10.1093/rb/rbw003.

[47] R.K.S. Raman, S.E. Harandi, Understanding Corrosion-Assisted Cracking of Magnesium Alloys for Bioimplant Applications BT - Magnesium Technology 2016, in: A. Singh, K. Solanki, M. V Manuel, N.R. Neelameggham (Eds.), Springer International Publishing, Cham, 2016: pp. 343–346. doi:10.1007/978-3-319-48114-2_66.

[48] F. Witte, J. Fischer, J. Nellesen, H.A. Crostack, V. Kaese, A. Pisch, F. Beckmann, H. Windhagen, In vitro and in vivo corrosion measurements of magnesium alloys, Biomaterials. 27 (2006) 1013–1018. doi:10.1016/j.biomaterials.2005.07.037.

[49] M.P. Staiger, A.M. Pietak, J. Huadmai, G. Dias, Magnesium and its alloys as orthopedic biomaterials: A review, Biomaterials. 27 (2006) 1728–1734. doi:10.1016/j.biomaterials.2005.10.003.

[50] M. Niinomi, Recent metallic materials for biomedical applications, Metall. Mater. Trans. A. 33 (2002) 477–486. doi:10.1007/s11661-002-0109-2.

[51] F. Witte, Reprint of: The history of biodegradable magnesium implants: A review, Acta Biomater. 23 (2015) S28–S40. doi:10.1016/j.actbio.2015.07.017.

[52] A. Pietak, P. Mahoney, G.J. Dias, M.P. Staiger, Bone-like matrix formation on

magnesium and magnesium alloys, J. Mater. Sci. Mater. Med. 19 (2008) 407–415. doi:10.1007/s10856-007-3172-9.

[53] F. Witte, V. Kaese, H. Haferkamp, E. Switzer, a. Meyer-Lindenberg, C.J. Wirth, H. Windhagen, In vivo corrosion of four magnesium alloys and the associated bone response, Biomaterials. 26 (2005) 3557–3563. doi:10.1016/j.biomaterials.2004.09.049.

[54] X. Liu, J. Sun, F. Zhou, Y. Yang, R. Chang, K. Qiu, Z. Pu, L. Li, Y. Zheng, Micro-alloying with Mn in Zn–Mg alloy for future biodegradable metals application, Mater. Des. 94 (2016) 95–104. doi:10.1016/j.matdes.2015.12.128.

[55] Y. Estrin, S.S. Nene, B.P. Kashyap, N. Prabhu, T. Al-Samman, New hot rolled Mg-4Li-1Ca alloy: A potential candidate for automotive and biodegradable implant applications, Mater. Lett. 173 (2016) 252–256. doi:10.1016/j.matlet.2016.03.052.

[56] T.A. Grünewald, H. Rennhofer, B. Hesse, M. Burghammer, S.E. Stanzl-Tschegg, M. Cotte, J.F. Löffler, A.M. Weinberg, H.C. Lichtenegger, Magnesium from bioresorbable implants: Distribution and impact on the nano- and mineral structure of bone, Biomaterials. 76 (2016) 250–260. doi:10.1016/j.biomaterials.2015.10.054.

[57] K.F. Farraro, K.E. Kim, S.L.-Y. Woo, J.R. Flowers, M.B. McCullough, Revolutionizing orthopaedic biomaterials: The potential of biodegradable and bioresorbable magnesium-based materials for functional tissue engineering., J. Biomech. 47 (2014) 1985. doi:10.1016/j.jbiomech.2013.12.003.

[58] D. Zhao, S. Huang, F. Lu, B. Wang, L. Yang, L. Qin, K. Yang, Y. Li, W. Li, W. Wang, S. Tian, X. Zhang, W. Gao, Z. Wang, Y. Zhang, X. Xie, J. Wang, J. Li, Vascularized bone grafting fixed by biodegradable magnesium screw for treating osteonecrosis of the femoral head., Biomaterials. 81 (2016) 84–92. doi:10.1016/j.biomaterials.2015.11.038.

[59] M.S. Uddin, C. Hall, P. Murphy, Surface treatments for controlling corrosion rate of biodegradable Mg and Mg-based alloy implants, Sci. Technol. Adv. Mater. 16 (2015) 53501. doi:10.1088/1468-6996/16/5/053501.

[60] T.S.N. Sankara Narayanan, I.S. Park, M.H. Lee, Strategies to improve the corrosion resistance of microarc oxidation (MAO) coated magnesium alloys for degradable implants: Prospects and challenges, Prog. Mater. Sci. 60 (2014) 1–71. doi:10.1016/j.pmatsci.2013.08.002.

[61] Y.L. Song, Y.H. Liu, S.R. Yu, X.Y. Zhu, Q. Wang, Plasma electrolytic oxidation coating on AZ91 magnesium alloy modified by neodymium and its corrosion resistance, Appl. Surf. Sci. 254 (2008) 3014–3020. doi:10.1016/j.apsusc.2007.10.043.

[62] X. Ren, Y. Feng, J. Guo, H. Wang, Q. Li, J. Yang, X. Hao, J. Lv, N. Ma, W. Li, Surface modification and endothelialization of biomaterials as potential scaffolds for vascular tissue engineering applications, Chem. Soc. Rev. 44 (2015) 5680–5742. doi:10.1039/C4CS00483C.

[63] C.L. Chu, X. Han, F. Xue, J. Bai, P.K. Chu, Effects of sealing treatment on corrosion resistance and degradation behavior of micro-arc oxidized magnesium alloy wires, Appl. Surf. Sci. 271 (2013) 271–275. doi:10.1016/j.apsusc.2013.01.175.

[64] Z. Jia, P. Xiong, Y. Shi, W. Zhou, Y. Cheng, Y.F. Zheng, T. Xi, S. Wei, Inhibitor encapsulated, self-healable and cytocompatible chitosan multilayer coating on biodegradable Mg alloy: a pH-responsive design, J. Mater. Chem. B. (2016). doi:10.1039/C6TB00117C.

[65] H. Reddy Tiyyagura, R. Rudolf, S. Gorgieva, R. Fuchs-Godec, V.R. Boyapati, K.M. Mantravadi, V. Kokol, The chitosan coating and processing effect on the physiological corrosion behaviour of porous magnesium monoliths, Prog. Org. Coatings. 99 (2016) 147–156. doi:10.1016/j.porgcoat.2016.05.019.

[66] H.M. Wong, K.W.K. Yeung, K.O. Lam, V. Tam, P.K. Chu, K.D.K. Luk, K.M.C. Cheung, A biodegradable polymer-based coating to control the performance of magnesium alloy orthopaedic implants, Biomaterials. 31 (2010) 2084–2096. doi:10.1016/j.biomaterials.2009.11.111.

[67] Y. Chen, S. Zhao, M. Chen, W. Zhang, J. Mao, Y. Zhao, M.F. Maitz, N. Huang, G. Wan, Sandwiched polydopamine (PDA) layer for titanium dioxide (TiO<inf>2</inf>) coating on magnesium to enhance corrosion protection, Corros. Sci. 96 (2015) 67–73. doi:10.1016/j.corsci.2015.03.020.

[68] F. Gong, J. Shen, R. Gao, X. Xie, X. Luo, Enhanced corrosion resistance of magnesium alloy by a silane-based solution treatment after an in-situ formation of the Mg(OH)2 layer, Appl. Surf. Sci. 365 (2016) 268–274. doi:10.1016/j.apsusc.2016.01.028.

[69] Y. Wang, Z. Huang, Q. Yan, C. Liu, P. Liu, Y. Zhang, C. Guo, G. Jiang, D. Shen, Corrosion behaviors and effects of corrosion products of plasma electrolytic oxidation coated AZ31 magnesium alloy under the salt spray corrosion test, Appl. Surf. Sci. 378 (2016) 435–442. doi:10.1016/j.apsusc.2016.04.011.

[70] Z. Wei, P. Tian, X. Liu, B. Zhou, In vitro degradation, hemolysis, and cytocompatibility of PEO/PLLA composite coating on biodegradable AZ31 alloy., J. Biomed. Mater. Res. B. Appl. Biomater. 103 (2015) 342–54. doi:10.1002/jbm.b.33208.

[71] N.J. Ostrowski, B. Lee, A. Roy, M. Ramanathan, P.N. Kumta, Biodegradable poly(lactide-co-glycolide) coatings on magnesium alloys for orthopedic applications, J. Mater. Sci. Mater. Med. 24 (2013) 85–96. doi:10.1007/s10856-012-4773-5.

[72] O. Jeon, S.J. Song, S.-W. Kang, A.J. Putnam, B.-S. Kim, Enhancement of ectopic bone formation by bone morphogenetic protein-2 released from a heparin-conjugated poly(l-lactic-co-glycolic acid) scaffold, Biomaterials. 28 (2007) 2763–2771. doi:10.1016/j.biomaterials.2007.02.023.

[73] S. Gorgieva, V. Kokol, Processing of gelatin-based cryogels with improved thermomechanical resistance, pore size gradient, and high potential for sustainable protein drug release, J. Biomed. Mater. Res. - Part A. 103 (2015) 1119–1130. doi:10.1002/jbm.a.35261.

[74] T. Kokubo, H. Takadama, How useful is SBF in predicting in vivo bone bioactivity?, Biomaterials. 27 (2006) 2907–15. doi:10.1016/j.biomaterials.2006.01.017.

[75] N. Li, Y. Zheng, Novel Magnesium Alloys Developed for Biomedical Application: A

Review, J. Mater. Sci. Technol. 29 (2013) 489–502. doi:10.1016/j.jmst.2013.02.005.

[76] E. Willbold, X. Gu, D. Albert, K. Kalla, K. Bobe, M. Brauneis, C. Janning, J. Nellesen, W. Czayka, W. Tillmann, Y. Zheng, F. Witte, Effect of the addition of low rare earth elements (lanthanum, neodymium, cerium) on the biodegradation and biocompatibility of magnesium., Acta Biomater. 11 (2015) 554–62. doi:10.1016/j.actbio.2014.09.041.

[77] Q. Peng, X. Hou, L. Wang, Y. Wu, Z. Cao, L. Wang, Microstructure and mechanical properties of high performance Mg–Gd based alloys, Mater. Des. 30 (2009) 292–296. doi:10.1016/j.matdes.2008.04.069.

[78] X. Zhang, Y. Wu, Y. Xue, Z. Wang, L. Yang, Biocorrosion behavior and cytotoxicity of a Mg–Gd–Zn–Zr alloy with long period stacking ordered structure, Mater. Lett. 86 (2012) 42–45. doi:10.1016/j.matlet.2012.07.030.

[79] A.Srinivasan, C. Blawert, Y. Huang, C.L. Mendis, K.U. Kainer, N. Hort, Corrosion behavior of Mg–Gd–Zn based alloys in aqueous NaCl solution, J. Magnes. Alloy. 2 (2014) 245–256. doi:10.1016/j.jma.2014.08.002.

[80] D. Tie, F. Feyerabend, N. Hort, D. Hoeche, K.U. Kainer, R. Willumeit, W.D. Mueller, In vitro mechanical and corrosion properties of biodegradable Mg-Ag alloys, Mater. Corros. 65 (2014) 569–576. doi:10.1002/maco.201206903.

[81] D. Tie, F. Feyerabend, W.-D. Müller, R. Schade, K. Liefeith, K.U. Kainer, R. Willumeit, Antibacterial biodegradable Mg-Ag alloys, Eur. Cells Mater. 25 (2012).

[82] A. Myrissa, N.A. Agha, Y. Lu, E. Martinelli, J. Eichler, G. Szakács, C. Kleinhans, R. Willumeit-Römer, U. Schäfer, A.-M. Weinberg, In vitro and in vivo comparison of binary Mg alloys and pure Mg, Mater. Sci. Eng. C. 61 (2016) 865–874. doi:http://dx.doi.org/10.1016/j.msec.2015.12.064.

[83] S. Gorgieva, J. Strancar, V. Kokol, Evaluation of surface/interface-related physicochemical and microstructural properties of gelatin 3D scaffolds, and their influence on fibroblast growth and morphology., J. Biomed. Mater. Res. A. (2014) 11–13. doi:10.1002/jbm.a.35076.

[84] Z. Yang, Y. JiangCorrespondence to: College of, L.X. Yu, B. Wen, F. Li, S. Sun, T. Hou, Preparation and characterization of magnesium doped hydroxyapatite–gelatin nanocomposite, J. Mater. Chem. 15 (2005) 1807. doi:10.1039/b418015c.

[85] G. Dhanaraj, A. Karthika, K. Louis, surendiran Mohan, K. Soundarapandian, Fabrication of divalent ions substituted hydroxyapatite/gelatin nanocomposite coating on electron beam treated titanium: mechanical, anticorrosive, antibacterial and bioactive evaluations, RSC Adv. (2015). doi:10.1039/C5RA05624A.

[86] V. Chiono, E. Pulieri, G. Vozzi, G. Ciardelli, A. Ahluwalia, P. Giusti, Genipin-crosslinked chitosan/gelatin blends for biomedical applications, J. Mater. Sci. Mater. Med. 19 (2008) 889–898. doi:10.1007/s10856-007-3212-5.

[87] M. Cheng, J. Deng, F. Yang, Y. Gong, N. Zhao, X. Zhang, Study on physical properties and nerve cell affinity of composite films from chitosan and gelatin solutions, Biomaterials. 24 (2003) 2871–2880. doi:10.1016/S0142-9612(03)00117-0.

[88] A.A. Haroun, V. Migonney, Synthesis and in vitro evaluation of gelatin/hydroxyapatite graft copolymers to form bionanocomposites, Int. J. Biol. Macromol. 46 (2010) 310–316. doi:10.1016/j.ijbiomac.2010.01.005.

[89] W.Y. Chan, K.S. Chian, M.J. Tan, In vitro metal ion release and biocompatibility of amorphous Mg67Zn28Ca5 alloy with/without gelatin coating, Mater. Sci. Eng. C. 33 (2013) 5019–5027. doi:10.1016/j.msec.2013.08.025.

[90] X. Xu, P. Lu, M. Guo, M. Fang, Cross-linked gelatin/nanoparticles composite coating on micro-arc oxidation film for corrosion and drug release, Appl. Surf. Sci. 256 (2010) 2367–2371. doi:10.1016/j.apsusc.2009.10.069.

[91] B. V Vladimirov, B.L. Krit, V.B. Lyudin, N. V Morozova, A.D. Rossiiskaya, I. V Suminov, A. V Epel'feld, Microarc oxidation of magnesium alloys: A review, Surf. Eng. Appl. Electrochem. 50 (2014) 195–232. doi:10.3103/S1068375514030090.

[92] T.S.N.S. Narayanan, 9 – Strategies to improve the corrosion resistance of microarc oxidation coatings on magnesium and its alloys: Implications for biomedical applications, in: Surf. Modif. Magnes. Its Alloy. Biomed. Appl., 2015: pp. 235–267. doi:10.1016/B978-1-78242-078-1.00009-8.

[93] I. Buzzacchera, M. Vorobii, N.Y. Kostina, A. De Los Santos Pereira, T. Riedel, M. Bruns, W. Ogieglo, M. Möller, C.J. Wilson, C. Rodriguez-Emmenegger, Polymer Brush-Functionalized Chitosan Hydrogels as Antifouling Implant Coatings, Biomacromolecules. 18 (2017) 1983–1992. doi:10.1021/acs.biomac.7b00516.

[94] B. Wang, L. Zhao, W. Zhu, L. Fang, F. Ren, Mussel-inspired nano-multilayered coating on magnesium alloys for enhanced corrosion resistance and antibacterial property, Colloids Surfaces B Biointerfaces. 157 (2017) 432–439. doi:10.1016/j.colsurfb.2017.06.013.

[95] J. Song, X. Cui, G. Jin, Z. Cai, E. Liu, X. Li, Y. Chen, B. Lu, Self-healing conversion coating with gelatin–chitosan microcapsules containing inhibitor on AZ91D alloy, Surf. Eng. (2017) 1–6. doi:10.1080/02670844.2017.1327187.

[96] L.-Y. CUI, J. XU, N. LU, R.-C. ZENG, Y.-H. ZOU, S.-Q. LI, F. ZHANG, In vitro corrosion resistance and antibacterial properties of layer-by-layer assembled chitosan/poly-L-glutamic acid coating on AZ31 magnesium alloys, Trans. Nonferrous Met. Soc. China (English Ed. 27 (2017) 1081–1086. doi:10.1016/S1003-6326(17)60126-2.

[97] S. Heise, M. Höhlinger, Y.T. Hernández, J.J.P. Palacio, J.A. Rodriquez Ortiz, V. Wagener, S. Virtanen, A.R. Boccaccini, Electrophoretic deposition and characterization of chitosan/bioactive glass composite coatings on Mg alloy substrates, Electrochim. Acta. 232 (2017) 456–464. doi:10.1016/j.electacta.2017.02.081.

[98] H. Gao, M. Zhang, J. Zhao, L. Gao, M. Li, In vitro and in vivo degradation and mechanical properties of ZEK100 magnesium alloy coated with alginate, chitosan and mechano-growth factor, Mater. Sci. Eng. C. 63 (2016) 450–461. doi:10.1016/j.msec.2016.02.073.

[99] L. Jia, C. Liang, N. Huang, Z. Zhou, F. Duan, L. Wang, Morphology and composition of coatings based on hydroxyapatite-chitosan-RuCl3 system on AZ91D prepared by pulsed electrochemical deposition, J. Alloys Compd. 656 (2016) 961–971. doi:10.1016/j.jallcom.2015.09.223.

[100] M. Höhlinger, S. Heise, V. Wagener, A.R. Boccaccini, S. Virtanen, Developing surface pre-treatments for electrophoretic deposition of biofunctional chitosan-bioactive glass coatings on a WE43 magnesium alloy, Appl. Surf. Sci. 405 (2017) 441–448. doi:10.1016/j.apsusc.2017.02.049.

[101] J. Zhang, Z. Wen, M. Zhao, G. Li, C. Dai, Effect of the addition CNTs on performance of CaP/chitosan/coating deposited on magnesium alloy by electrophoretic deposition, Mater. Sci. Eng. C. 58 (2016) 992–1000. doi:10.1016/j.msec.2015.09.050.

[102] J. Zhang, F. Zhu, Y. Zhang, M. Hu, Y. Chi, X. Zhang, X. Guo, In vitro bioactivity, degradation property and cell viability of the CaP/chitosan/graphene coating on magnesium alloy in m-SBF, Int. J. Electrochem. Sci. 11 (2016) 9326–9339. doi:10.20964/2016.11.63.

[103] J. Song, X. Cui, Z. Liu, G. Jin, E. Liu, D. Zhang, Z. Gao, Advanced microcapsules for self-healing conversion coating on magnesium alloy in Ce(NO3)3 solution with microcapsules containing La(NO3)3, Surf. Coatings Technol. 307 (2016) 500–505. doi:10.1016/j.surfcoat.2016.09.024.

[104] L. de Y. Pozzo, T.F. da Conceição, A. Spinelli, N. Scharnagl, A.T.N. Pires, Chitosan coatings crosslinked with genipin for corrosion protection of AZ31 magnesium alloy sheets, Carbohydr. Polym. 181 (2018) 71–77. doi:https://doi.org/10.1016/j.carbpol.2017.10.055.

[105] L.C. Córdoba, A. Marques, M. Taryba, T. Coradin, F. Montemor, Hybrid coatings with collagen and chitosan for improved bioactivity of Mg alloys, Surf. Coatings Technol. (2017). doi:https://doi.org/10.1016/j.surfcoat.2017.08.062.

[106] N. Scharnagl, C. Blawert, 14 - Polymer-based degradable coatings for metallic biomaterials, in: C. Wen (Ed.), Surf. Coat. Modif. Met. Biomater., Woodhead Publishing, (2015): pp. 393–422. doi:https://doi.org/10.1016/B978-1-78242-303-4.00014-4.

[107] K. Yliniemi, B.P. Wilson, F. Singer, S. Höhn, E. Kontturi, S. Virtanen, Dissolution Control of Mg by Cellulose Acetate–Polyelectrolyte Membranes, ACS Appl. Mater. Interfaces. 6 (2014) 22393–22399. doi:10.1021/am5063597.

[108] B. Zhu, Y. Xu, J. Sun, L. Yang, C. Guo, J. Liang, B. Cao, Preparation and Characterization of Aminated Hydroxyethyl Cellulose-Induced Biomimetic Hydroxyapatite Coatings on the AZ31 Magnesium Alloy, Metals (Basel). 7 (2017).

[109] P. Neacsu, A.I. Staras, S.I. Voicu, I. Ionascu, T. Soare, S. Uzun, V.D. Cojocaru, A.M. Pandele, S.M. Croitoru, F. Miculescu, C.M. Cotrut, I. Dan, A. Cimpean, Characterization and In Vitro and In Vivo Assessment of a Novel Cellulose Acetate-Coated Mg-Based Alloy for Orthopedic Applications, Materials (Basel). 10 (2017).

[110] S. Kaabi Falahieh Asl, S. Nemeth, M.J. Tan, Novel biodegradable calcium

phosphate/polymer composite coating with adjustable mechanical properties formed by hydrothermal process for corrosion protection of magnesium substrate, J. Biomed. Mater. Res. Part B Appl. Biomater. 104 (2016) 1643–1657. doi:10.1002/jbm.b.33505.

[111] E. Aghion, T. Yered, Y. Perez, Y. Gueta, The Prospects of Carrying and Releasing Drugs Via Biodegradable Magnesium Foam, Adv. Eng. Mater. 12 (2010) B374--B379. doi:10.1002/adem.200980044.

[112] G. Ryan, a Pandit, D. Apatsidis, Fabrication methods of porous metals for use in orthopaedic applications, Biomaterials. 27 (2006) 2651–2670. doi:10.1016/j.biomaterials.2005.12.002.

[113] J. Kubásek, D. Vojtěch, E. Jablonská, I. Pospíšilová, J. Lipov, T. Ruml, Structure, mechanical characteristics and in vitro degradation, cytotoxicity, genotoxicity and mutagenicity of novel biodegradable Zn-Mg alloys., Mater. Sci. Eng. C. Mater. Biol. Appl. 58 (2016) 24–35. doi:10.1016/j.msec.2015.08.015.

[114] C. Zhao, F. Pan, S. Zhao, H. Pan, K. Song, A. Tang, Microstructure, corrosion behavior and cytotoxicity of biodegradable Mg-Sn implant alloys prepared by sub-rapid solidification., Mater. Sci. Eng. C. Mater. Biol. Appl. 54 (2015) 245–51. doi:10.1016/j.msec.2015.05.042.

[115] M. Schinhammer, A.C. Hänzi, J.F. Löffler, P.J. Uggowitzer, Design strategy for biodegradable Fe-based alloys for medical applications., Acta Biomater. 6 (2010) 1705–13. doi:10.1016/j.actbio.2009.07.039.

[116] S.K. Swain, I. Gotman, R. Unger, C.J. Kirkpatrick, E.Y. Gutmanas, Microstructure, mechanical characteristics and cell compatibility of β-tricalcium phosphate reinforced with biodegradable Fe-Mg metal phase., J. Mech. Behav. Biomed. Mater. 53 (2015) 434–444. doi:10.1016/j.jmbbm.2015.09.002.

[117] J.E. Gray, B. Luan, Protective coatings on magnesium and its alloys — a critical review, J. Alloys Compd. 336 (2002) 88–113. doi:10.1016/S0925-8388(01)01899-0.

[118] Y. Yang, C. Michalczyk, F. Singer, S. Virtanen, A.R. Boccaccini, In vitro study of polycaprolactone/bioactive glass composite coatings on corrosion and bioactivity of pure Mg, Appl. Surf. Sci. 355 (2015) 832–841. doi:10.1016/j.apsusc.2015.07.053.

[119] M. Yazdimamaghani, M. Razavi, D. Vashaee, V.R. Pothineni, J. Rajadas, L. Tayebi, Significant degradability enhancement in multilayer coating of polycaprolactone-bioactive glass/gelatin-bioactive glass on magnesium scaffold for tissue engineering applications, Appl. Surf. Sci. 338 (2015) 137–145. doi:10.1016/j.apsusc.2015.02.120.

[120] M.M. Farag, H. Yun, Effect of gelatin addition on fabrication of magnesium phosphate-based scaffolds prepared by additive manufacturing system, Mater. Lett. 132 (2014) 111–115. doi:10.1016/j.matlet.2014.06.055.

[121] Y. Chen, S. Zhao, M. Chen, W. Zhang, J. Mao, Y. Zhao, M.F. Maitz, N. Huang, G. Wan, Sandwiched polydopamine (PDA) layer for titanium dioxide (TiO2) coating on magnesium to enhance corrosion protection, Corros. Sci. 96 (2015) 67–73. doi:10.1016/j.corsci.2015.03.020.

[122] A.O. Elzoghby, Gelatin-based nanoparticles as drug and gene delivery systems: reviewing three decades of research., J. Control. Release. 172 (2013) 1075–91. doi:10.1016/j.jconrel.2013.09.019.

[123] M.C. Morán, N. Rosell, G. Ruano, M.A. Busquets, M.P. Vinardell, Gelatin-based nanoparticles as DNA delivery systems: Synthesis, physicochemical and biocompatible characterization, Colloids Surfaces B Biointerfaces. 134 (2015) 156–168. doi:10.1016/j.colsurfb.2015.07.009.

[124] A. Bigi, B. Bracci, S. Panzavolta, Effect of added gelatin on the properties of calcium phosphate cement., Biomaterials. 25 (2004) 2893–9. doi:10.1016/j.biomaterials.2003.09.059.

[125] C.-K. Chiu, D. Lee, H. Chen, L. Chow, C.-C. Ko, In-situ hybridization of calcium silicate and hydroxyapatite-gelatin nanocomposites enhances physical property and in vitro osteogenesis, J. Mater. Sci. Mater. Med. 26 (2015) 1–14. doi:10.1007/s10856-015-5456-9.

[126] M.E. Lynge, Recent developments in poly (dopamine) - based coatings for biomedical applications, 10 (2015) 2725–2742.

[127] C.-T. Kao, C.-C. Lin, Y.-W. Chen, C.-H. Yeh, H.-Y. Fang, M.-Y. Shie, Poly(dopamine) coating of 3D printed poly(lactic acid) scaffolds for bone tissue engineering, Mater. Sci. Eng. C. 56 (2015) 165–173. doi:10.1016/j.msec.2015.06.028.

[128] M.E. Lynge, R. van der Westen, A. Postma, B. Städler, PDA39-Polydopamine—a nature-inspired polymer coating for biomedical science, Nanoscale. 3 (2011) 4916. doi:10.1039/c1nr10969c.

[129] Y. Wu, X. Liu, Y. Li, M. Wang, Surface-adhesive layer-by-layer assembled hydroxyapatite for bioinspired functionalization of titanium surfaces, RSC Adv. 4 (2014) 44427–44433. doi:10.1039/C4RA07907H.

[130] Y. Ding, L.-T. Weng, M. Yang, Z. Yang, X. Lu, N. Huang, Y. Leng, Insights into the Aggregation/Deposition and Structure of a Polydopamine Film., Langmuir. 30 (2014) 12258−12269. doi:10.1021/la5026608.

[131] J. Jiang, L. Zhu, L. Zhu, B. Zhu, Y. Xu, Surface characteristics of a self-polymerized dopamine coating deposited on hydrophobic polymer films, Langmuir. 27 (2011) 14180– 14187. doi:10.1021/la202877k.

[132] W.-B. Tsai, W.-T. Chen, H.-W. Chien, W.-H. Kuo, M.-J. Wang, Poly(dopamine) coating to biodegradable polymers for bone tissue engineering., J. Biomater. Appl. 28 (2014) 837–848. doi:10.1177/0885328213483842.

[133] J. Ryu, S.H. Ku, H. Lee, C.B. Park, Mussel-inspired polydopamine coating as a universal route to hydroxyapatite crystallization, Adv. Funct. Mater. 20 (2010) 2132–2139. doi:10.1002/adfm.200902347.

[134] L. Huang, J. Yi, Q. Gao, X. Wang, Y. Chen, P. Liu, Carboxymethyl chitosan functionalization of CPED-treated magnesium alloy via polydopamine as intermediate layer, Surf. Coatings Technol. 258 (2014) 664–671. doi:10.1016/j.surfcoat.2014.08.020.

[135] F. Singer, M. Schlesak, C. Mebert, S. Höhn, S. Virtanen, Investigating the Influence of Polydopamine Coatings on the Corrosion Properties of Magnesium for possible Biodegradable Applications, (2015). doi:10.1021/acsami.5b08760.

[136] X. Liu, Z. Zhen, J. Liu, T. Xi, Y. Zheng, S. Guan, Y. Zheng, Y. Cheng, Multifunctional MgF2/Polydopamine Coating on Mg Alloy for Vascular Stent Application, J. Mater. Sci. Technol. 31 (2015) 733–743. doi:10.1016/j.jmst.2015.02.002.

[137] B. Lin, M. Zhong, C. Zheng, L. Cao, D. Wang, L. Wang, J. Liang, B. Cao, Preparation and characterization of dopamine-induced biomimetic hydroxyapatite coatings on the AZ31 magnesium alloy, Surf. Coatings Technol. 281 (2015) 82–88. doi:10.1016/j.surfcoat.2015.09.033.

[138] C. Liu, Y. Xin, G. Tang, P.K. Chu, Influence of heat treatment on degradation behavior of bio-degradable die-cast AZ63 magnesium alloy in simulated body fluid, Mater. Sci. Eng. A. 456 (2007) 350–357. doi:10.1016/j.msea.2006.12.020.

[139] F. Witte, J. Fischer, J. Nellesen, H.-A. Crostack, V. Kaese, A. Pisch, F. Beckmann, H. Windhagen, In vitro and in vivo corrosion measurements of magnesium alloys, Biomaterials. 27 (2006) 1013–1018. doi:10.1016/j.biomaterials.2005.07.037.

[140] J. Trinidad, I. Marco, G. Arruebarrena, J. Wendt, D. Letzig, E. Sáenz de Argandoña, R. Goodall, Processing of Magnesium Porous Structures by Infiltration Casting for Biomedical Applications, Adv. Eng. Mater. 16 (2014) 241–247. doi:10.1002/adem.201300236.

[141] S.T. Methods, Standard Test Methods of, (2013) 1–9. doi:10.1520/E0009-09.2.

[142] Y. Wang, M. Wei, J. Gao, J. Hu, Y. Zhang, Corrosion process of pure magnesium in simulated body fluid, Mater. Lett. 62 (2008) 2185–2188. doi:10.1016/j.matlet.2007.11.092.

[143] L.-X. Li, D. Xu, X.-Q. Li, W.-C. Liu, Y. Jia, Excellent fluoride removal properties of porous hollow MgO microspheres, New J. Chem. 38 (2014) 5445–5452. doi:10.1039/C4NJ01361A.

[144] M. Jevtić, M. Mitrić, S. Škapin, B. Jančar, N. Ignjatović, D. Uskoković, Crystal structure of hydroxyapatite nanorods synthesized by sonochemical homogeneous precipitation, Cryst. Growth Des. 8 (2008) 2217–2222. doi:10.1021/cg7007304.

[145] J. Weng, Formation and characteristics of the apatite layer on plasma-sprayed hydroxyapatite coatings in simulated body fluid, Biomaterials. 18 (1997) 1027–1035. doi:10.1016/S0142-9612(97)00022-7.

[146] T.-H. Tsai, C.-Y. Lin, H.-J. Tsai, S.-Y. Chen, S.-P. Tai, K.-H. Lin, C.-K. Sun, Biomolecular imaging based on far-red fluorescent protein with a high two-photon excitation action cross section, Opt. Lett. 31 (2006) 930–932. doi:10.1364/OL.31.000930.

[147] A. Paz, D. Guadarrama, M. López, J.E. González, N. Brizuela, J. Aragón, A Comparative Study of Hydroxyapatite Nanoparticles Synthesized By Different Routes, Quim. Nov. 35 (2012) 1724–1727. doi:10.1590/S0100-40422012000900004.

[148] Y. Xin, K. Huo, H. Tao, G. Tang, P.K. Chu, Influence of aggressive ions on the degradation behavior of biomedical magnesium alloy in physiological environment, Acta Biomater. 4 (2008) 2008–2015. doi:https://doi.org/10.1016/j.actbio.2008.05.014.

[149] M. Tomozawa, S. Hiromoto, Growth mechanism of hydroxyapatite-coatings formed on pure magnesium and corrosion behavior of the coated magnesium, Appl. Surf. Sci. 257 (2011) 8253–8257. doi:http://dx.doi.org/10.1016/j.apsusc.2011.04.087.

[150] X. Wang, J. Huang, K. Wang, M. Neufurth, H.C. Schroder, S. Wang, W.E.G. Muller, The morphogenetically active polymer, inorganic polyphosphate complexed with GdCl3, as an inducer of hydroxyapatite formation in vitro, Biochem. Pharmacol. 102 (2016) 97– 106. doi:10.1016/j.bcp.2015.12.011.

[151] N. Hort, Y. Huang, D. Fechner, M. Störmer, C. Blawert, F. Witte, C. Vogt, H. Drücker, R. Willumeit, K.U. Kainer, F. Feyerabend, Magnesium alloys as implant materials-Principles of property design for Mg-RE alloys, Acta Biomater. 6 (2010) 1714–1725. doi:10.1016/j.actbio.2009.09.010.

[152] Y. Xin, T. Hu, P.K. Chu, In vitro studies of biomedical magnesium alloys in a simulated physiological environment: A review, Acta Biomater. 7 (2011) 1452–1459. doi:10.1016/j.actbio.2010.12.004.

[153] P. Manfrinetti, K.A. Gschneidner, Phase equilibrium in the La- Mg (0–65 at.% Mg) and Gd-Mg systems, J. Less Common Met. 123 (1986) 267–275.

[154] S. Agarwal, J. Curtin, B. Duffy, S. Jaiswal, Biodegradable magnesium alloys for orthopaedic applications: A review on corrosion, biocompatibility and surface modifications, Mater. Sci. Eng. C. 68 (2016) 948–963. doi:10.1016/j.msec.2016.06.020.

[155] F. Cao, Z. Shi, J. Hofstetter, P.J. Uggowitzer, G. Song, M. Liu, A. Atrens, Corrosion of ultra-high-purity Mg in 3.5% NaCl solution saturated with Mg(OH)2, Corros. Sci. 75 (2013) 78–99. doi:http://dx.doi.org/10.1016/j.corsci.2013.05.018.

[156] F. Guadarrama-Muñoz, J. Mendoza-Flores, R. Duran-Romero, J. Genesca, Electrochemical study on magnesium anodes in NaCl and CaSO4–Mg(OH)2 aqueous solutions, Electrochim. Acta. 51 (2006) 1820–1830. doi:http://dx.doi.org/10.1016/j.electacta.2005.02.144.

[157] A. Srinivasan, P. Ranjani, N. Rajendran, Electrochemical polymerization of pyrrole over AZ31 Mg alloy for biomedical applications, Electrochim. Acta. 88 (2013) 310–321. doi:http://dx.doi.org/10.1016/j.electacta.2012.10.087.

[158] G. Baril, G. Galicia, C. Deslouis, N. Pébère, B. Tribollet, V. Vivier, An Impedance Investigation of the Mechanism of Pure Magnesium Corrosion in Sodium Sulfate Solutions, J. Electrochem. Soc. 154 (2007) C108. doi:10.1149/1.2401056.

[159] G. Song, A. Atrens, D. St John, X. Wu, J. Nairn, The anodic dissolution of magnesium in chloride and sulphate solutions, Corros. Sci. 39 (1997) 1981–2004. doi:10.1016/s0010-938x(97)00090-5.

[160] A.D. King, N. Birbilis, J.R. Scully, Accurate Electrochemical Measurement of Magnesium Corrosion Rates; a Combined Impedance, Mass-Loss and Hydrogen

Collection Study, Electrochim. Acta. 121 (2014) 394–406. doi:10.1016/j.electacta.2013.12.124.

[161] M. Finšgar, I. Milošev, Corrosion behaviour of stainless steels in aqueous solutions of methanesulfonic acid, Corros. Sci. 52 (2010) 2430–2438. doi:10.1016/j.corsci.2010.04.001.

[162] J.H. Muyonga, C.G.B. Cole, K.G. Duodu, Fourier transform infrared (FTIR) spectroscopic study of acid soluble collagen and gelatin from skins and bones of young and adult Nile perch (Lates niloticus), Food Chem. 86 (2004) 325–332. doi:10.1016/j.foodchem.2003.09.038.

[163] L. Berzina-Cimdina, N. Borodajenko, Research of Calcium Phosphates Using Fourier Transform Infrared Spectroscopy, Infrared Spectrosc. – Mater. Sci. Eng. Technol. (2012) 123–148. doi:10.5772/36942.

[164] R. Rettig, S. Virtanen, Composition of corrosion layers on a magnesium rare-earth alloy in simulated body fluids, J. Biomed. Mater. Res. - Part A. 88 (2009) 359–369. doi:10.1002/jbm.a.31887.

[165] H.M. Wong, Y. Zhao, V. Tam, S. Wu, P.K. Chu, Y. Zheng, M.K.T. To, F.K.L. Leung, K.D.K. Luk, K.M.C. Cheung, K.W.K. Yeung, Invivo stimulation of bone formation by aluminum and oxygen plasma surface-modified magnesium implants, Biomaterials. 34 (2013) 9863–9876. doi:10.1016/j.biomaterials.2013.08.052.

[166] D. Gopi, P.R. Bhalaji, S. Ramya, L. Kavitha, Evaluation of biodegradability of surface treated AZ91 magnesium alloy in SBF solution, J. Ind. Eng. Chem. 23 (2015) 218–227. doi:10.1016/j.jiec.2014.08.019.

[167] T.M. Mukhametkaliyev, M.A. Surmeneva, A. Vladescu, C.M. Cotrut, M. Braic, M. Dinu, M.D. Vranceanu, I. Pana, M. Mueller, R.A. Surmenev, A biodegradable AZ91 magnesium alloy coated with a thin nanostructured hydroxyapatite for improving the corrosion resistance, Mater. Sci. Eng. C. 75 (2017) 95–103. doi:10.1016/j.msec.2017.02.033.

[168] G. Baril, C. Blanc, N. Pébère, AC Impedance Spectroscopy in Characterizing Time-Dependent Corrosion of AZ91 and AM50 Magnesium Alloys Characterization with Respect to Their Microstructures, J. Electrochem. Soc. 148 (2001) B489. doi:10.1149/1.1415722.

[169] M. Chen, Y. Chen, W. Zhang, S. Zhao, J. Wang, J. Mao, W. Li, Y. Zhao, N. Huang, G. Wan, Controlling the corrosion rate and behavior of biodegradable magnesium by a surface-immobilized ultrathin 1-hydroxyethylidene-1,1-diphosphonic acid (HEDP) film, RSC Adv. 6 (2016) 15247–15259. doi:10.1039/C5RA23228G.

[170] D.-J. Lin, F.-Y. Hung, S. Jakfar, M.-L. Yeh, Tailored coating chemistry and interfacial properties for construction of bioactive ceramic coatings on magnesium biomaterial, Mater. Des. 89 (2016) 235–244. doi:10.1016/j.matdes.2015.09.144.

[171] L.C. Córdoba, M.F. Montemor, T. Coradin, Silane/TiO2 coating to control the corrosion rate of magnesium alloys in simulated body fluid, Corros. Sci. 104 (2016) 152–161. doi:10.1016/j.corsci.2015.12.006.

[172] Yufeng Zheng-Magnesium Alloys as Degradable Biomaterials-CRC Press (2015).pdf, (n.d.).

[173] H.O. Ammar, H.A. Salama, S.A. El-Nahhas, H. Elmotasem, Design and evaluation of chitosan films for transdermal delivery of glimepiride., Curr. Drug Deliv. 5 (2008) 290–298. doi:10.2174/156720108785915005.

[174] S. Gorgieva, V. Kokol, Preparation, characterization, and in vitro enzymatic degradation of chitosan-gelatine hydrogel scaffolds as potential biomaterials, J. Biomed. Mater. Res. - Part A. 100 A (2012) 1655–1667. doi:10.1002/jbm.a.34106.

[175] Z. Li, X. Gu, S. Lou, Y. Zheng, The development of binary Mg-Ca alloys for use as biodegradable materials within bone, Biomaterials. 29 (2008) 1329–1344. doi:10.1016/j.biomaterials.2007.12.021.

[176] T.T. Nge, J. Sugiyama, Surface functional group dependent apatite formation on bacterial cellulose microfibrils network in a simulated body fluid, J. Biomed. Mater. Res. - Part A. 81 (2007) 124–134. doi:10.1002/jbm.a.31020.

[177] S. Kumar, J. Koh, Physiochemical, optical and biological activity of chitosan-chromone derivative for biomedical applications, Int. J. Mol. Sci. 13 (2012) 6103–6116. doi:10.3390/ijms13056102.

[178] S. Feliu, I. Llorente, Corrosion product layers on magnesium alloys AZ31 and AZ61: Surface chemistry and protective ability, Appl. Surf. Sci. 347 (2015) 736–746. doi:10.1016/j.apsusc.2015.04.189.

[179] X. Cai, K. Ma, Y. Zhou, T. Jiang, Y. Wang, Surface functionalization of titanium with tetracycline loaded chitosan–gelatin nanosphere coatings via EPD: fabrication, characterization and mechanism, RSC Adv. 6 (2016) 7674–7682. doi:10.1039/C5RA17109A.

[180] B. Lin, M. Zhong, C. Zheng, L. Cao, D. Wang, L. Wang, J. Liang, B. Cao, Preparation and characterization of dopamine-induced biomimetic hydroxyapatite coatings on the AZ31 magnesium alloy, Surf. Coatings Technol. 281 (2015) 82–88. doi:10.1016/j.surfcoat.2015.09.033.

[181] F. Singer, M. Schlesak, C. Mebert, S. Höhn, S. Virtanen, Corrosion Properties of Polydopamine Coatings Formed in One-Step Immersion Process on Magnesium, ACS Appl. Mater. Interfaces. 7 (2015) 26758–26766. doi:10.1021/acsami.5b08760.

[182] H. Yu, Q. Dong, J. Dou, Y. Pan, C. Chen, Preparation of Si-containing oxide coating and biomimetic apatite induction on magnesium alloy, Appl. Surf. Sci. (2016). doi:10.1016/j.apsusc.2016.02.051.

[183] Y. Xin, K. Huo, H. Tao, G. Tang, P.K. Chu, Influence of aggressive ions on the degradation behavior of biomedical magnesium alloy in physiological environment., Acta Biomater. 4 (2008) 2008–15. doi:10.1016/j.actbio.2008.05.014.

[184] L.J. Gibson, The mechanical behaviour of cancellous bone, J. Biomech. 18 (1985) 317–328. doi:10.1016/0021-9290(85)90287-8.

[185] M.-H. Kang, H.-D. Jung, S.-W. Kim, S.-M. Lee, H.-E. Kim, Y. Estrin, Y.-H. Koh, Production and bio-corrosion resistance of porous magnesium with hydroxyapatite coating for biomedical applications, Mater. Lett. 108 (2013) 122–124. doi:10.1016/j.matlet.2013.06.096.

[186] M. Cheng, T. Wahafu, G. Jiang, W. Liu, Y. Qiao, X. Peng, T. Cheng, X. Zhang, G. He, X. Liu, A novel open-porous magnesium scaffold with controllable microstructures and properties for bone regeneration, Sci. Rep. 6 (2016) 24134. doi:10.1038/srep24134.

[187] Y. Bi, Y. Zheng, Y. Li, Microstructure and mechanical properties of sintered porous magnesium using polymethyl methacrylate as the space holder, Mater. Lett. 161 (2015) 583–586. doi:10.1016/j.matlet.2015.09.039.

[188] M. Yazdimamaghani, M. Razavi, D. Vashaee, L. Tayebi, Microstructural and mechanical study of PCL coated Mg scaffolds, 0 (2014) 1–7. doi:10.1179/1743294414Y.0000000307.

[189] M. Yazdimamaghani, M. Razavi, D. Vashaee, V.R. Pothineni, S. Assefa, G.A. Köhler, J. Rajadas, L. Tayebi, In vitro analysis of Mg scaffolds coated with polymer/hydrogel/ceramic composite layers, Surf. Coatings Technol. (2016) 1–7. doi:10.1016/j.surfcoat.2016.01.017.

[190] E. Van De Walle, I. Van Nieuwenhove, E. Vanderleyden, H. Declercq, K. Gellynck, D. Schaubroeck, H. Ottevaere, H. Thienpont, W.H. De Vos, M. Cornelissen, S. Van Vlierberghe, P. Dubruel, Polydopamine–Gelatin as Universal Cell-Interactive Coating for Methacrylate-Based Medical Device Packaging Materials: When Surface Chemistry Overrules Substrate Bulk Properties, Biomacromolecules. 17 (2016) 56–68. doi:10.1021/acs.biomac.5b01094.

Publications based on the present work

1. Hanuma Reddy Tiyyagura, Rebeka Rudolf, Selestina Gorgieva, Regina Fuchs-Godec, Venkatappa Rao Boyapati, Krishna Mohan Mantravadi,Vanja Kokol. "The chitosan coating and processing effect on the physiological corrosion behaviour of porous magnesium monoliths", Progress in Organic Coatings, 2016, vol. 99, pp. 147-156.
2. Hanuma Reddy Tiyyagura, Balakrishnan Munirathinam, B. Ratna Sunil, Lakshman Neelakantan,RegineWillumeit',MantravadiKrishnaMohan,VanjaKokol "Electrochemical corrosion behaviour of Mganesium binary alloys. Journal of Material Science and Surface engineering. vol.5(3), 2017, pp. 561-564.
3. Hanuma Reddy Tiyyagura, K. Chaitanya Kumar, Snehashis Pal, M. Krishna Mohan "Finite Element Analysis for Mechanical Response of Magnesium Foams with Regular Structure Obtained by Powder Metallurgy Method", Procedia Engineering, 2016, vol .149, pp. 425-430.
4. Hanuma Reddy Tiyyagura, Selestina Gorgieva, Regina Fuchs-Godec, Krishna Mohan Mantravadi,Vanja Kokol, "*In-situ* cross-linked gelatine coating on AZ91 Mg alloy for less-corrosive and surface bioactive orthopaedic application", (under review)
5. Hanuma Reddy Tiyyagura, Regina Fuchs-Godec, Tomaž Vuherer, Selestina Gorgeiva, Mantravadi Krishna Mohan,Vanja Kokol" Bioinspired Ploy dopamine/Gelatine(PDA/GEL) surface modification on the magnesium scaffold to control the degradation for bone tissue engineering applications", (under review)
6. Hanuma Reddy Tiyyagura ,Fuchs-Godec, Regin Kurečič, Manja, Mantravadi Krishna Mohan,VanjaKokol "Electrochemical studies of pure magnesium surface coated with electrospun cellulose acetate (CA) nanofibers", (under review)
7. Hanuma Reddy Tiyyagura, Regina Fuchs-Godec, Tomaž Vuherer, Selestina Gorgeiva, Mantravadi Krishna Mohan, Vanja Kokol "*In vitro* studies of Magnesium binary alloys in Simulated Body Fluids", (under review)

Conferences / Proceedings

1. Hanuma Reddy.T, Selestina Gorgieva, B.V Appa Rao, M.K Mohan, Vanja Kokol,"Controlling the degradation rate of gelatin-modified AZ91 magnesium alloy in

means of dip coating procedures", Eurocorr 2015 : Earth, Water, Fire, Corrosion happens everywhere / European corrosion congress, Graz, Austria, 6-12 September 2015

2. Hanuma Reddy Tiyyagura ,Fuchs-Godec, Regin Kurečič, Manja, Mantravadi Krishna Mohan,VanjaKokol, "Electrochemical studies of pure magnesium surface coated with electrospun cellulose acetate (CA) nanofibers" International Conference of Lithuanian Society of Chemistry, Lithuanian Academy of Science, Vilnius, Lithuania, April 28-29, 2016. ISBN 978-609-95511-3-5.

3. Hanuma Reddy, Tiyyagura,Gorgieva, Selestina Vuherer, Tomaž,Fuchs-Godec, Regina,Mantravadi, Krishna Mohan Kokol, Vanja, "Mechanical and corrosion properties of biopolymer-coated magnesium scaffold for biomedical applications" POZ-MAR 2016, University of Maribor, Slovenia.

Book chapter:

Hanuma Reddy Tiyyagura, Tamil Selvan Mohan, Snehashis Pal, M. Krishna Mohan "Magnesium and its alloys as orthopedic biomaterials", NEW - Fundamental biomaterials: Metals, Elsevier(under review)